IMPACT RESISTANCE OF CORNER SUPPORTED CONCRETE PANELS

By

Mohammed Abdullah M. Alaloula

Dissertation

Submitted to the Faculty of the

Graduate School of Vanderbilt University

in partial fulfillment of the requirements

for the degree of

DOCTOR OF PHILOSOPHY

in

Civil Engineering

May 10th, 2024

Nashville, Tennessee

Approved:

Prodyot K. Basu, D.Sc., Chair

Douglas Adams, Ph.D.

Sankaran Mahadevan, Ph.D.

Caglar Oskay, Ph.D.

Ozgur Yapar, Ph.D.

DEDICATION

I am profoundly grateful to my parents Abdullah and Jameelah, for their unwavering encouragement, sacrifices, and boundless love throughout my academic journey. My most profound appreciation goes to my supportive wife, Afnan, whose constant belief in me and patience sustained me through the challenges. Lastly, my heartfelt thanks to my daughter Reema, whose understanding and joyous presence brought balance to my life as I pursued this Ph.D. endeavor.

ACKNOWLEDGMENTS

I would like to express my sincere gratitude to everyone who has helped me during my Ph.D. journey.

First and foremost, I would like to thank my advisor, Prof. P. K. Basu. His guidance, support, and mentorship have been invaluable to me throughout my Ph.D. studies. His knowledge, expertise, and constructive feedback have helped me grow as a researcher and have shaped my thinking in countless ways.

I would also like to thank my committee members for their insightful feedback and constructive criticism. Their expertise and diverse perspectives have enriched my research and have helped me improve my work.

I would like to express my gratitude to the staff and faculty at Vanderbilt University for providing me with the necessary resources, tools, and opportunities to conduct my research. I am particularly grateful to the Civil and Environmental Engineering staff for their administrative support and assistance throughout my Ph.D. studies. I am especially thankful to David Koester, Director of LASIR and his support staff for their invaluable assistance in undertaking impact testing using the Instron Impact Tester.

I am deeply grateful to my family for their unwavering love, support, and encouragement. Their belief in me has been a source of strength and motivation, and I could not have completed this journey without them.

Lastly, I would like to thank all the participants who participated in my research. Their willingness to share their experiences and insights has been vital to the success of my research.

Thank you, everyone, for your support and encouragement. My Ph.D. journey has been challenging, but it has also been rewarding, and I am grateful to have had such a supportive community throughout this process.

TABLE OF CONTENTS

LIST OF TABLES

LIST OF FIGURES

CHAPTER 1

INTRODUCTION

1.1 Background

Exterior claddings are provided to protect buildings from the elements, acting as a barrier between interior and exterior environments. In doing so, the cladding serves three purposes – a) safely transfer external environmental load effects to support structure, b) control ingress of air, light, rain, snow, heat, fire, smoke, vapor, etc. from outside, and c) satisfy functional, aesthetic and durability requirements. Of all the materials, concrete and glass enclosures have been most widely used for public and commercial buildings as well as for potentially high-risk facilities. This research is limited to the consideration of structural integrity of precast concrete panel claddings, with and without glazed window openings, against impact and blast effects. Such claddings have been used since the 1920s and became increasingly popular since the 1950s [1]. During the last decade, the performance of such claddings has improved noticeably, as new finishing techniques and materials, new insulating and anchoring methods as well as improved methods for addressing rain, wind, vapor and heat movement were introduced.

Extreme events experienced by buildings may be caused by environmental conditions (like wind, earthquake, flooding, fire, etc.) or, due to man-made causes. The primary focus of this research is on the effects of man-made extreme events like explosions and ballistic projectile attack, excluding fire and heat resulting from such events. Over the last few decades, increased terrorist activities have necessitated evaluation of the integrity of claddings against terrorist attacks. In a successful mitigation plan it is necessary to address two distinct scenarios:

i) a new building in the planning and design stage; and

ii) an existing building built conventionally with no provision to resist terrorist attack.

In the first case, necessary provisions can be made following official recommendations during the design and construction phases before occupation. In the second case, however, supplementary measures are needed to harden the existing building, as far as possible, without unduly compromising its functionality and aesthetics. During recent decades, assurance of adequate blast and projectile impact load resistance of civil and military structures has assumed

great importance. In the present-day world, with the proliferation of terrorist outfits, domestic and foreign, armed with IEDs, small arms, mortars, etc. ready to be deployed to kill perceived enemies indiscriminatingly, which mostly include innocent civilians, is wreaking havoc around the world. Events like 1995 bombing Alfred P. Murrah Federal Building in downtown Oklahoma City and the 1996 terrorist attack on The Khobar Tower in Dhahran, Saudi Arabia are some of the early examples of such events. More recently, this and other western countries are experiencing unusual rise in hate-based mass killing of innocents using semi-automatic guns, sometimes, fueled by irresponsible political rhetoric magnified by mental health problems. The January 6 2021 events at the U.S. Capital are a recent major example of this trend.

Depending upon place and time, different solutions to the problem have been put forward. In one area, there seems to be common agreement is the urgent need to ensure safety to life and property from such attacks. In this context, one of the focus items is based on the scenario of protecting people inside a building from blast and projectile assault by attackers operating from without. As the first line of defense, the needed measures should first be applied to strategically critical buildings and places of assembly, both to existing structures and new construction. The nature of damage inflicted on a building or on a critical infrastructural component like bridge due to the detonation of explosives depends upon the stand-off distance of the source of explosion and the magnitude of the blast measured by the equivalent weight (W) of TNT (Trinitrotoluene – C6H2(NO2)3CH3). The activation of the explosive by the detonator initiates chemical reactions generating shock waves travelling at supersonic speed, intense heat, flying debris, and high velocity fragments (shrapnel), purposely embedded to cause maximum injury. In short, a blast wave is a small area of intense pressure expanding supersonically outward from an explosive core. If the stand-off distance is large enough, the dominant effect of explosion is elevated pressure in the blast wave causing full or partial failure of a structure. In shorter stand-off distances, apart from the explosive force (or blast load), heat, and the high velocity fragments also come into play. The gas and air pressure immediately behind a detonation front can be well in excess of 750 atmospheres and the resulting shock front impinging a structure is the main agent to cause structural damage. In the case of small arms fire and mortar attacks, the damaging effect of the projectile tend to be more localized near the point of impact, and a major source of worry is the penetration of the ballistic projectile into the interior of a building causing injury or death to the people inside.

In the context of a performance-based approach, to design a building against blast and projectile impact loads, four objectives need to be satisfied:

(i) Prevent progressive collapse, which is usually the cause of most fatalities.

(ii) Limit injuries, if any, to those inside the building caused by failing structural components, flying fragments and debris.

(iii) Minimize harm to people near the building perimeter.

(iv) Prevent casualties due to bullets or other projectiles by trapping it in the building envelop preventing inside penetration.

Blast wave propagation in air is a problem of fluid dynamics in which the pressure and flow resulting from the detonation releases a large amount of energy in a localized volume. This results in a leading shock wave, followed by a 'self-similar' subsonic flow field. In simple terms, a blast wave is a spherical pressure front expanding supersonically outward from an explosive core. It has a leading shock front of compressed gases. The initial blast wave is of large magnitude peaking over a very short duration. It is followed by a negative wind pressure of longer duration tending to suck the structure back towards the source. The degree of damage resulting from a certain blast wave is determined by the stand-off distance of the source. As this distance becomes smaller, the destructive effect becomes more severe and may be coupled with intense thermal effect and impact of flying shrapnel.

1.2 Motivation

Since the possibility of terrorist attack on target critical facilities by bomb blasts and/or ballistic projectile impact is reality of present-day life, not only in the Middle East but other parts of world, namely, United States as well, it is necessary to design such facilities to mitigate against destruction and loss of life wrought by such attacks. In the case of blast effect, it is necessary to account for the type, size and location of the explosive which determine, in addition to the blast pressure, the effects of heat, flying fragments and negative pressure. Another important aspect of the blast effect which is not normally accounted for is the additional damaging influence of a surface blast. In such a scenario, the energy of a surface blast not only creates shock wave front in the air, part of the energy is also used up in crater creation and the generation of ground shock waves which travel towards the structure as primary (P-), shear (S-), and Rayleigh waves, just as

in the case of an earthquake. These subterranean shock waves may cause additional damage to the structure, see Fig. 1.1.

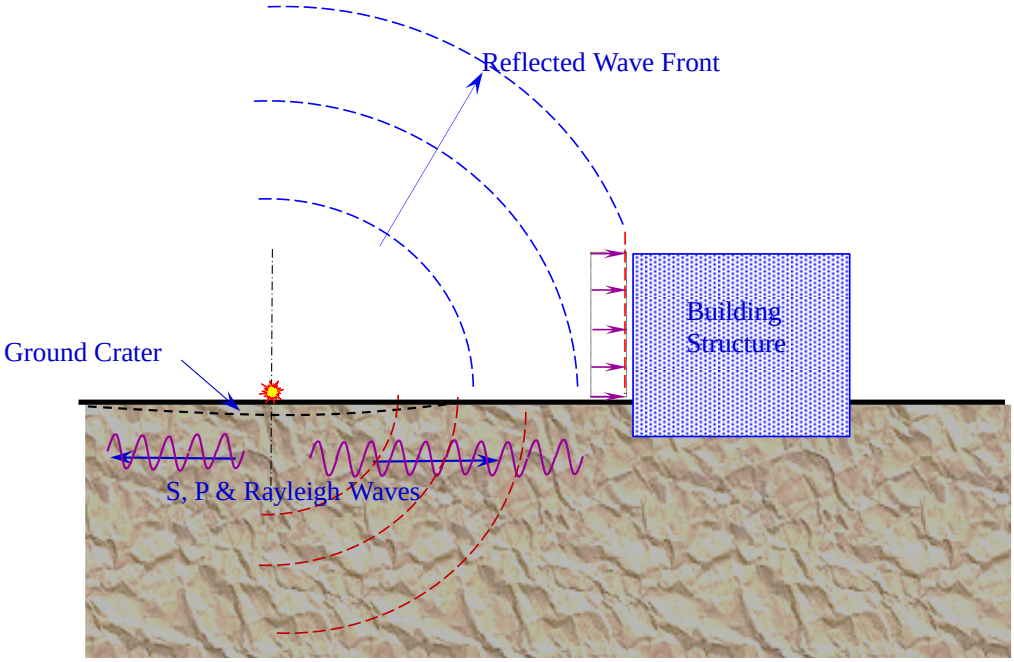

Figure 1.1. Energy transfer paths with surface blast.

Apart from commonly used passive measures to increase the stand-off distance for, say, an explosive laden vehicle, additional measures to reduce casualties and damage to properties are as follows:

- First Line of Defense: Strategically placed external barriers to increase the stand-off distance. Alternatively, one can erect protective barrier walls which are expensive, potentially inconvenient, and of questionable effectiveness, except in war-like situations.
- Second Line of Defense: Blast and impact resistant building envelop which will normally comprise of full and/or partial (window) glazing. The increased vulnerability of glazing to blast and impact may require especial treatment.
- Next Line of Defense: Adequacy of structural skeleton in resisting the loads transferred to prevent progressive failure.

In the case of projectile impact, the response of a building envelop depends upon the type, size and support conditions of cladding envelop; its geometry, material, dimensions, orientation with respect to projectile path, and most importantly the projectile velocity. Depending upon the values of these parameters, the response of the target may be global with damage appearing globally in the form of excessive deflection and cracking. This kind of behavior typically occurs at lower projectile velocities. If the velocity is large enough, the target response will tend to cause local damage indifferent degrees. In the extreme case, the projectile will perforate the target with residual velocity. In the case of blast effect, for sufficiently large lead-off distance, the target response tends to be global. In a nutshell, to make a building terrorist attack proof, the following actions are necessary:

1. Ensuring integrity of main structural framework designed to resist gravity and horizontal loads; and
2. Ensuring adequate protective cladding (including roofing) for the building to effectively withstand the blast effect and prevent the penetration of projectiles (ballistic or bomb shrapnel). It is advantageous to use cladding panels which is hardened against blast and impact. Various possibilities exist for manufacturing such panels of concrete. In the case of window openings, the best solution is to use laminated E-glass panels. Examples of traditional precast panels are shown in Fig. 1.2.

(a) As built (b) During construction

Figure 1.2. (a) Existing wall panels, (b) wall panels under construction.

In the case of existing buildings, guaranteeing all the requirements is difficult. For instance, to prevent progressive failure, strengthening of selected members and joints can prove to be

daunting. On the other hand, different possibilities for hardening the existing cladding are as follows:

a) Bonding Fiber Reinforced Concrete (FRP) composite laminates (wet or dry) or pultruded sheets comprising
    - Fibers (woven or chopped) – carbon (graphite), E-glass, S-glass, steel, aramid, polypropylene, etc.
    - Matrix – epoxy, polyesters, phenol formaldehyde, etc.
b) Coatings—Poly-urea
c) Bonded foam panels—stiffened glass foam (Tycor), resin infused balsa, PVC foam sheets, metal wool panels, etc.
d) Anti-blast films – polyurethane sheets.

The hardening materials selection based on the predicted scenarios are guided by:

- Cost
- Availability
- Safety
- Existing base material, concrete or glass
- Ease of application.

For windows and glass walls, the strengthening materials can be blast resistant transparent films or regular glazing can be replaced by E-glass glazing. Some of aforementioned hardening measures if applied to the claddings involve the use of materials which may emit hazardous fumes detrimental to the health of people inside.

In the case of projectile impact, the response of a building envelop depends upon the type, size and support conditions of cladding envelop; its geometry, material, dimensions, orientation with respect to target, and most importantly the projectile velocity. Depending upon these factors, the response of the target may be global with damage appearing globally in the form of excessive deflection and cracking. This kind of behavior typically occurs at lower projectile velocities. If the velocity is large enough, the target response will tend to cause local damage of different degrees. In the extreme case, the projectile will perforate the target with a residual velocity.

1.3 Current Design Practice

In the U.S., concrete claddings design is required to follow the guidelines in the PCI Design Handbook [2]. Simplistic guidelines for blast-resistance design of precast, prestressed concrete components appear in the appendix section of this handbook but lack information on projectile impact effects. For instance, the deflection limit requirement is specified as blast response criteria. However, a number of prescriptive guidelines and specifications [2-8] are available for ensuring structural integrity against weapons effect by various agencies, such as DoD, but none explicitly addresses the issue of methodology to be used for reliable checking of the performance of a facility against blast and projectile impact effects. In some instances, however, the need for using an acceptable dynamic analysis methodology is emphasized and measures to ensure performance requirements are specified. Such requirements define the acceptable structural damage in terms of response limits for individual element types based on the defined levels of protection. The response limits are specified as either maximum support rotation or maximum ductility, which is defined as the ratio of the maximum deflection to the elastic deflection. For typical precast concrete components, blast-resistant design is primarily focused on the design of the exterior building components and their connections such as precast wall panels. Blast-resistant building components are designed to provide acceptable performance in the event of an explosion.

In almost all cases, a design methodology where the structural components are analyzed as equivalent single-degree-of-freedom (SDOF) systems is deemed acceptable. The SDOF method idealizes the structural component into a mass-spring system with stiffness and mass related to those in the blast-loaded structural component see Fig. 1.3.

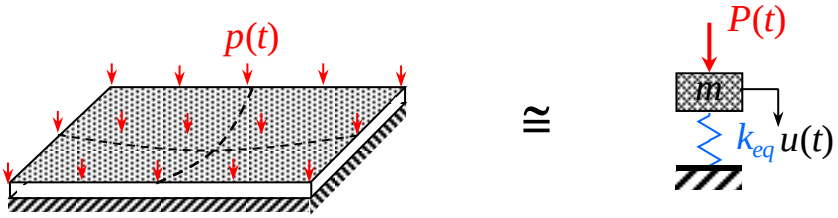

(a) Actual structure (b) SDOF model

Figure 1.3. Equivalent spring-mass model for a plate supporting dynamic load.

The equivalent SDOF system is so defined that its deflection at each time step is equal to the maximum deflection of the structural component, assuming its response can be described in terms of single degree of freedom (that is, the point of maximum deflection) and an assumed shape

function that defines motion at all other points on the component relative to the maximum deflection. In some more recent studies, the single spring model was replaced by several springs covering the panel area. But such approaches pitifully fail to reflect the actual local as well as global damage characteristics due to highly complex response involving plasticity, damage, perforation, fragmentation, wave propagation and strain-rate effects.

According to Zukas [9], the best way to study and check different scenarios of materials shock and impact loading conditions is to use well validated numerical simulation tools based on, say, finite element simulation and/or smooth particle hydrodynamics based 'hydrocode.' Generically, a hydrocode is a software designed to simulate the response of materials under rapidly applied load. In this study, the hydrocode capabilities of Abaqus Explicit will be used and only impact loading will be considered.

1.4 Research Objectives and Scope

The primary goal of this research is to develop and apply accurate modeling techniques to predict the performance of building claddings with and without hardening measures against ballistic impact and blast loads and arrive at simple but reasonably accurate methods for practical application. To realize the primary goal, the following objectives are identified:

1. Arrive at the physical details of the panels and loading to be used in the study
   a) based on practice and Precast/Prestressed Concrete Institute recommendations [2].
   b) identification of the nature of typical blast and impact loads for buildings based on professional recommendations [3-8].
   c) identification of a candidate hardening scheme.
2. Determine suitable models for component materials, like concrete, steel, glass, polyethylene, etc., of the panel to be used in the simulation.
3. Design and fabricate the test specimen keeping in view the testing facilities available at Vanderbilt University.
4. Define the mathematical model(s) to be used in the study and identify the relevant material parameters.
5. Determine the material properties consistent with the needs identified in Objective 4.
6. Undertake impact load tests to determine the actual response of test specimen.

7. Undertake three-D numerical simulations to predict the response of the test panels using nonlinear finite element method.
8. Validate simulations results with test data.

Objectives 1 and 2 are presented in Chapter 2. Chapter 3 deals with Objective 4. Objectives 3, 5, and 6 are covered in Chapter 4 and partly in Appendices A and B. Chapter 5 deals with Objectives 7, 8 and 9. Finally, conclusions and recommendations are given in Chapter 6.

CHAPTER 2

NATURE OF IMPACT AND BLAST EFFECTS ON PLATES

2.1 Selection of Cladding Panel and Hardening Measure

In Chapter 1, the use of standardized precast reinforced concrete claddings in building construction was discussed. The details of such panels in terms of geometry, concrete, steel reinforcement, attachment and window opening were carefully examined. Based on such information the typical candidate panels were identified. In making the choice, only single-story panels were considered. Thereafter, based on the resources available, the required test panels, both in terms of type and number were arrived at. Two basic types of standard precast concrete panels were identified one solid and other with concentric glazed opening. These rectangular panels were assumed to be anchored at the corners at the floor levels of the supporting structure. The overall dimensions of typical prototype panels were found to be close be 12ft×6ft×0.5ft. A suitable concrete grade for the panel was identified as M40. Moreover, provision of standard steel reinforcement comprising of wire mesh near and top and bottom faces was necessary. Prestressed concrete cladding panels are also used in practice. The modeling and simulation of such panels will be like the reinforced ones, except require allowance for the prestressing force. In the present study, only steel reinforced cladding will only be considered. Actual details of the test models used in this study is given in Chapter 4.

Different choices for hardening of existing cladding panels are as follows:

a) Bonding Fiber Reinforced Concrete (FRP) composite laminates (wet or dry) or pultruded sheets comprising of
    i) Fibers (woven or chopped) – carbon (graphite), E-glass, S-glass, steel, aramid, polypropylene, etc.
    ii) Matrix – epoxy, polyesters, phenol formaldehyde, etc.
b) Coatings – Polyurea.
c) Bonded foam panels – stiffened glass foam (Tycor), resin infused balsa, PVC foam sheets, metal wool panels, etc.
d) Anti-blast films – polyurethane sheets.

The selection of hardening materials based on the predicted scenarios are guided by:

- Cost
- Availability
- Safety
- Existing base material, concrete or glass
- Ease of application.

For windows and glass walls, the strengthening materials can be blast resistant transparent films or regular glazing can be replaced by E-glass glazing. Some of the hardening measures if applied to the claddings involve the use of materials which may emit hazardous fumes detrimental to the health of the residents.

The most used window glazing in existing buildings is float glass. Keeping in view the needs of safety, economy, ease of application and utility, as the first line of defense against breakage from projectile impact and blast effects, the application of bonded safety films is an attractive option. High density polyethylene sheet of appropriate thickness and adequate bonding layer can be used for this purpose. This type of sheet is supposed to be extremely strong against impact and abrasion. According to manufacturers [112], such a film can provide protection from:

- flying broken glass caused by accident.
- violent weather (glass breakage from high wind pressures and flying debris).
- attempted break ins by vandals and thieves.
- explosions caused by terrorists.
- projectile impacts.

Accordingly, as a cost-effective safety measure, self-adhesive polyethylene film is not only tried on window glazing but also on solid concrete surface in one face or both the faces. Further details of the film used in this study are given in Chapter 4.

Based on above considerations, subsequent discussions will be restricted to corner supported rectangular precast cladding panels of two types, solid and glazed, with and without protective polyethylene film applied to one face or both the faces.

2.2 Nature of Impact and Blast Loading Effects

First, the nature of impact loading will be discussed in detail to be followed by a brief discussion of similarities and dissimilarities between impact and blast load effects. Impact phenomenon occurs when a solid body moving with a speed, say, V_p collides with another solid body, stationary or moving with a velocity, say, $V_t < V_p$. Therefore, the relative velocity of the striker, or projectile, with respect to the target is $V_o = V_p - V_t$. In real life, this phenomenon occurs deliberately or accidentally all the time. The outcome of an impact depends upon shapes, sizes, and material types of target and projectile, and relative velocity and motion path of the projectile. If the event is deliberate, most likely, the outcome is damage, preconceived or not. If, on the other hand, the event is accidental, the outcome is uncertain depending upon associated controlling factors. Some typical examples of impact situation are as follows:

- Controlled demolition of a structure using wrecker ball.
- Enemy projectile attack on a nuclear reactor containment structure.
- Military hardware and soldier body armors resisting enemy projectile attack.
- Buildings and other civil infrastructure components exposed to severe projectile impact during extreme weather conditions like landfall of tornados.
- Deliberate detonation of explosives to cause harm to people and infrastructure components.
- Moving vehicle impacting against a barrier or another car.
- Impact of meteorites of planets and space vehicles.
- Reforming of hot wrought iron with a sledgehammer by a metalsmith, etc.

In most of the above situations, the target is stationary. In the case of detonation of explosives, apart from the impact fragments and heat, there will be extreme air shock wave pressure engulfing the target. In an impact situation, the projectile may be propelled by externally applied forces, namely fired ammunition like a flying bullet or an air borne projectile propelled by the power of storm. Alternatively, the projectile may be self-propelled like a rocket or missile, guided or not. A meteorite is propelled by gravitational pull.

2.2.1 Target Response to Impact

At the moment of impact, kinetic energy of a projectile of mass Mp with velocity Vo, termed as impact velocity is

$$K_p = \frac{1}{2} M V_o^2 \tag{2.1}$$

If the target is stationary, it represents the total initial kinetic energy of impact. From the moment the projectile strikes the target, this kinetic energy is dissipated in various ways. In the case of a stationary concrete target, a rapid attenuation of the velocity (or kinetic energy) of the projectile occurs as strain energy due to elastic and plastic deformations of the target, as damage energy due to local fracture or destruction of part of the target, and as damping energy due to viscous and material damping effects. This causes a sharp attenuation of projectile velocity. In the approach phase, a stage is reached when work done by the contact forces reaches its peak value. At this point the projectile speed drops to zero and rebound phase begins when the reversible part of the stored impact energy tends to put the target and projectile apart till separation occurs at some relative velocity (ricochet effect). The ratio of rebound velocity and incidence velocity is an indication of degree of damage caused by the first cycle of impact. If the projectile is flexible, part of the impact energy will also be consumed to cause elastic-plastic deformations in the projectile. The motion of the target after impact may also account for the part of the impact energy. If no ricochet effect is involved, the projectile and target are in continued contact with residual kinetic energy. Typical range of ballistic projectile speeds compiled from various sources is given in Table 2.1.

Table 2.1. Ballistic projectile speeds.

Type of Weapon	Velocity Range (ft/sec)	Velocity Classification	Response Type
Meteorite impact	>40,000	Super high	Vaporization
Special purpose guns	4250 to 9840	High	Local
Conventional guns	1640 to 4250	Medium (<8200)	Mostly local
Pneumatic guns	80 to 1640	Mostly low	Mostly overall
Free falling mass	0 to 80	Low (<820)	Overall

If the impact velocity, V_o, is low (say, less than a few hundred ft/sec), the penetration resistance of a target is determined by dynamic deformation mechanisms and fracture processes within the target and the projectile. Apart from the velocity of impact, target thickness, strength, ductility, toughness, acoustic impedance and density of both target and projectile materials play important role in determining the nature and extent of damage.

In view of above observations, the impact energy consumption can be specifically identified as follows:

1. Deformation and damage depending upon the relative strength properties of projectile and target, shape of projectile and target as well support conditions of the target, and impact velocity, V_o.
2. Residual motion of projectile and target locked together or separately. In the event the projectile gets lodged into a target of mass m and the target starts moving with a velocity V_t, the kinetic energy after impact will be

$$K_t = 1/2(M+m)V_t^2 \tag{2.2}$$

By applying the law of conservation of momentum,

$$MV_o = (M+m)V_t$$

so that

$$K_t = \frac{M}{M+m}K_p \qquad \frac{V_t}{V_o} = \frac{M}{M+m} \tag{2.3}$$

Based on Eqs. (2.1) to (2.3), it follows

$$K_t = \frac{M}{M+m}K_p \tag{2.4}$$

3. Heat generation due to friction between the penetrating projectile and target as well as

internal particular heat generation due to elastic-plastic deformation, stress wave propagation and local damage processes.

4. Acoustic wave generation in the ambient environment.

If a hard projectile impacts a ductile metallic plate target, depending upon V_o, the damage may appear as a crater with the projectile penetrating into and getting lodged into the target. At very low velocities, no damage will occur, and the hard projectile will bounce off the target with little energy loss. If the target is thin enough, with increasing velocities cratering (spalling), penetration and scabbing will occur successively. With velocities exceeding the ballistic limit, the projectile will perforate the target with an exit velocity, V_p. Ballistic limit is the minimum speed of projectile to cause perforation of the target. In the case of ductile materials like steel the damage, due its shape, is termed as petaling effect, see Fig. 2.1.

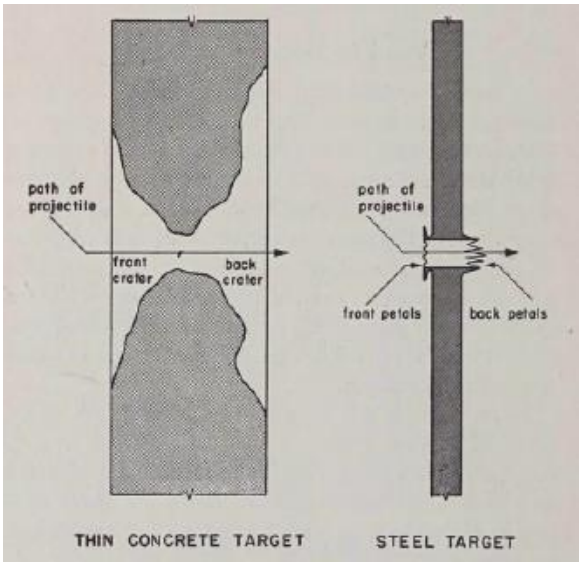

Figure 2.1. Petaling effect [10].

In general, harder materials, like ceramics, provide superior resistance to impact force and construction material like concrete does so to a lesser degree, depending upon its strength.

If a thin rectangular panel of relatively brittle material supported at its corners (or, edges) is impacted by a hard projectile at its center, the resulting bending of the panel will create hoop tension causing radial cracks (sometimes, accompanied by circumferential crack), as shown in Fig. 2.2.

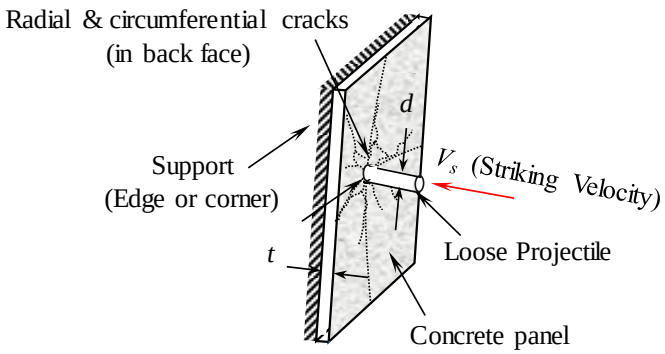

Figure 2.2. Cracking due to projectile impact on concrete panel.

In the case of overall damage, the impact energy dissipation is global. In the case of thicker target, the impact energy dissipation is mostly local, around the impact point. As the small impact area on the target plate is in a state of confinement from the material surrounding the projectile contact area, the concrete under the contact area is in a state of severe hydrostatic compression. In addition to causing local damage, the compression waves released from the impact zone tend to attenuate with distance from the impact point. The compression wave travels along the thickness direction as well as along length and width of the plate. The wave travelling in the thickness direction gets reflected from the unconstrained back face of the target creating tensile reflection waves, which in turn interact with the incident compression wave causing cratering in the impact face, as shown in Fig. 2.3a and Fig. 2.5. The cratering phenomenon can be further explained in terms of Prandtl's slip line field theory giving cratering depth to be 0.707***d***, shown in Fig. 2.4. In addition, depending upon the speed, the projectile tends to push out a conical plug from the rear face of the target, which eventually crumbles (Fig. 2.3b). In the process, large shear stresses are mobilized and shear bands are formed. Such back face cratering failure is also known as scabbing. If, however, the projectile speed exceeds the ballistic limit of the target, the target undergoes perforation (Fig. 2.3c).

In Fig. 2.3(a), the depth of projectile penetration is denoted by ***x***. The required minimum thickness of target to prevent scabbing is denoted by ***s***. Required minimum thickness of a target for a projectile velocity, $\boldsymbol{V_o}$, to prevent perforation is denoted by ***e***, and is termed as perforation limit.

Instead of orthogonal impact, if the projectile strikes at an angle, the effect is to create a normal and a tangential component of the impact force. In majority of situations, orthogonal impact is more critical.

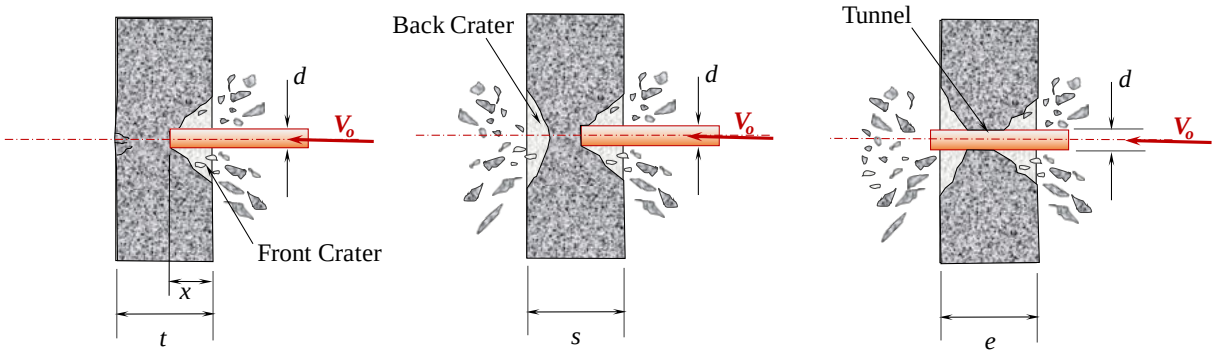

(a) Spalling (b) Scabbing (c) Perforation

Figure 2.3. Orthogonal impact.

In the case of concrete plates lightly reinforced with top and bottom mesh of steel rods, as shown in Fig. 2.5, the response does not change appreciably as far as scabbing and perforation behaviors are concerned. The reinforcements become effective only after scabbing has occurred, because as the shear cone is formed, the steel rods restrain the shear cone from separation and thereby preventing the projectile from exiting out of the back face of the target. If the volume of reinforcement is increased, the plate assumes more rigidity and the response changes accordingly.

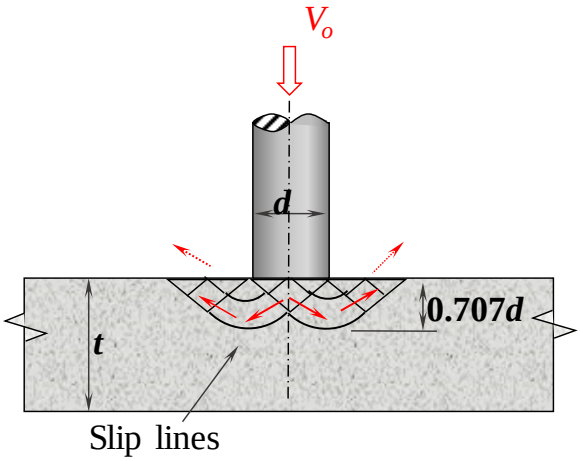

Figure 2.4. Slip field causing cratering by flat headed rigid projectile in a thick target.

Front face reinforcement and aggregate interlock also contribute to increased plate stiffness. However, the back-face reinforcement expends more energy acting as a tension

membrane. Apart from energy dissipation due to target penetration and global target deformations, part of the kinetic energy of impact may be deliberately dissipated through support deformations.

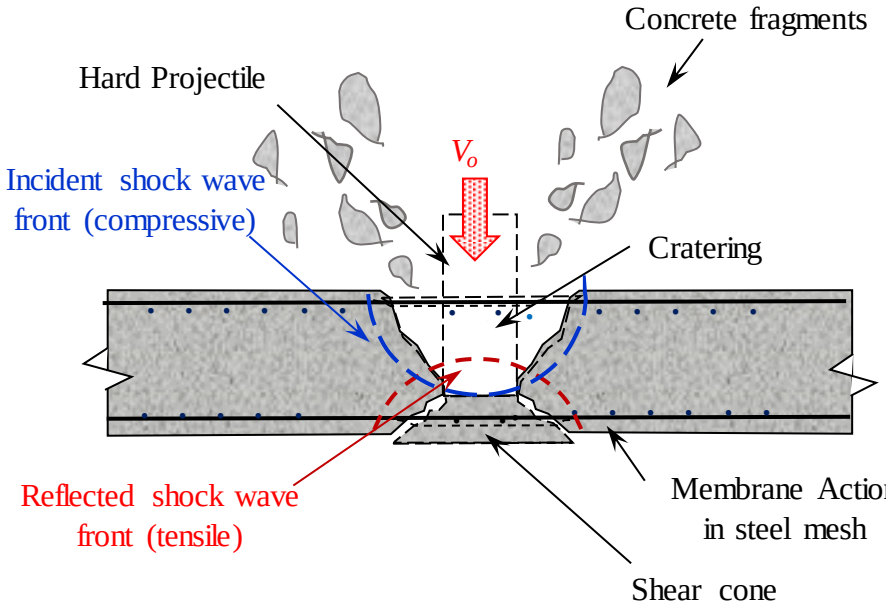

Figure 2.5. Projectile impact response of reinforced concrete plate.

2.2.2 Semi-Empirical Prediction Methods

Over the years, a large number of empirical formulas have been put forward to predict the local response of concrete targets (like ballistic limit, penetration depth, and scabbing limit) of concrete targets due to hard projectile impact without any regard to support conditions or global response. Formula predictions were widely different, often dimensionally inconsistent, did not explicitly allow for the presence of reinforcement and were of marginal practical value. So, no further consideration of these empirical formulas is warranted as part of the present study.

2.2.3 Basic Equations of Target Response

The three required conservation equations are those of mass, momentum, and energy.

i) Conservation of mass:

$$\rho \Omega = \rho_o \tag{2.5}$$

ii) Conservation of momentum:

$$\sigma_{ij,j} + \rho f_i = \rho \ddot{u}_i,\ i = 1,2,3 \tag{2.6}$$

where:

σ_{ij} = Cauchys stress tensor

ρ = Current material density

f_i = Body force density

$\ddot{u}_i$ = Current Acceleration

iii) Conservation of energy:

$$\dot{e} = s_{ij}\dot{s}_{ij} - (p+v)\frac{\dot{\Omega}}{\Omega} \tag{2.7}$$

where:

$\dot{e}$ = rate of change of energy per relative volume.

$\frac{\dot{\Omega}}{\Omega}$ = ratio of rate of change of relative volume and relative volume.

s_{ij} = deviatoric stress tensor = $\sigma_{ij} + (p+v)\delta_{ij}$

p = hydrostatic stress = $-\frac{\sigma_{kk}}{3} - v$

v = material bulk viscosity, which is viscous damping coefficient for slow volumetric straining (like creep) of material under constant stress

These small deformation Lagrangian equations can be implemented numerically satisfying appropriate elliptic boundary and initial conditions.

2.3 Wave Effects from Projectile Impact

Under a rapidly varying load, the easily noticeable response of the target structure is physical (or bulk) oscillatory motion. In wave propagation, only the wave form moves, not the material. In other words, wave is a disturbance moving through a medium from one location to another transmitting energy but not matter. Consequently, when an excitation is applied very rapidly to a structure, its effect is not felt instantly throughout its volume. The effect is transferred from the point of application to successive points over a period through atomic vibrations, depending upon the velocity of propagation for the material the structure is made of. In the case of solid continuum, this velocity is a function of material density and elastic properties. If the rate of load application is not very rapid, the effect of excitation can be assumed to be experienced by all points in the body instantly because the comparative velocity of wave propagation is very high.

Typical velocities of one-dimensional wave propagation in materials of interest in this study are shown in Table 2.2.

Table 2.2. Acoustic velocity of materials of interest.

Material	Weight density	Velocity of compression wave
Steel	490 pcf	16,500 ft/sec
Concrete	Variable	10,500 to 12,100 ft/sec
Glass	Variable	13,000 to 16,400 ft/sec
Polyethylene	56 pcf	6,400 ft/sec

In a solid, there is non-zero stiffness both for volumetric deformations and shear deformations. Hence, it is possible to generate stress (or, strain) waves with different velocities depending upon the deformation mode. Stress waves causing volumetric deformations (compressive or extensional) are known as pressure waves or P-waves. In this case the particles oscillate in the direction of wave propagation. Stress waves causing shear deformations are termed as shear waves or S-waves. In addition to these body waves, additional waves can exist near the surface of a solid body suddenly impinged by a fast-moving projectile or exposed to earthquake shock. These are known as Rayleigh (R-waves) and Love waves. Rayleigh waves are particularly important when it is created by surface impact. Such waves undergo both longitudinal and transverse motions that decrease in amplitude with distance from the surface.

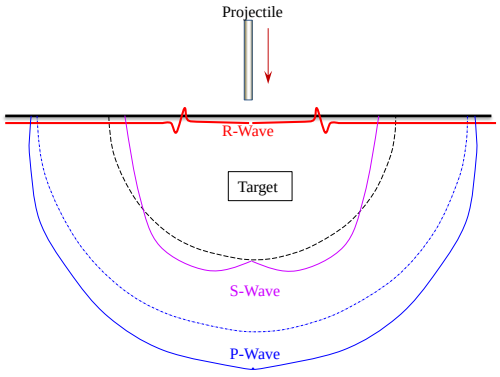

Figure 2.6. P-, S- and R-waves in the half-space.

The schematics of P-, S- and R-waves caused by the impact of a projectile on a semi-infinite solid continuum are shown in Fig. 2.6. Love waves are, however, of seismic origin.

The particle movement in Rayleigh wave is shown in Fig. 2.7. The longitudinal and transverse motions associated with R-waves decrease exponentially with distance from the impacted surface. This behavior is similar to water particle motion of surface waves propagating in deep bodies of water. The velocities of S- and R-waves are approximately 61% and 56% of P-wave. If the impact loaded media is a thin plate, the stress wave is termed as Lamb wave, which actually is Rayleigh wave confined in the thin plate. Actually, a Rayleigh wave appears as a Lamb wave if the thickness of the plate is less than the wavelength of a Rayleigh wave. Lamb waves propagate in a solid bounded by two parallel surfaces resulting from the superposition of multiple reflections of P-waves and S-waves from the confining surfaces, with symmetrical and unsymmetrical components. In order to be able to simulate such motion at the particulate level, microscale simulations are necessary, which is beyond the scope of the present effort.

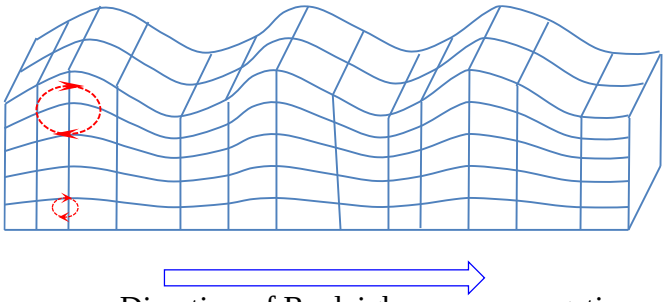

Figure 2.7. Direction of Rayleigh wave propagation.

2.3.1 Basic Equations of Wave Propagation

Using divergence notation the general equilibrium equations for a three-D isotropic solid continuum ignoring the body force density can be expressed as

$$\rho_o \frac{(\partial^2 \bar{u})}{(\partial t^2)} = (\lambda + 2\mu)\nabla(\nabla.\bar{u}) - \mu\nabla \times (\nabla \times \bar{u}) \tag{2.8}$$

where ρ = density of target material;

λ & μ = Lame' parameters for target material

$\bar{u} = iu_1 + ju_2 + ku_3$

$$\nabla = i\frac{\partial}{\partial x_1} + j\frac{\partial}{\partial x_2} + k\frac{\partial}{\partial x_3}$$

$$\nabla \bullet \bar{u} = \frac{\partial}{\partial x_1} + \frac{\partial}{\partial x_2} + \frac{\partial}{\partial x_3}$$

$$\nabla \times \bar{u} = i\left(\frac{\partial u_3}{\partial x_2} - \frac{\partial u_2}{\partial x_3}\right) + j\left(\frac{\partial u_1}{\partial x_3} - \frac{\partial u_3}{\partial x_1}\right) + k\left(\frac{\partial u_2}{\partial x_1} - \frac{\partial u_1}{\partial x_2}\right)$$

For one-D wave propagation in a 3-D continuum, it is necessary to define the displacement components as $u_1 = u_1(x_1, t);\ u_2 = u_3 = 0$. Eq. (2.8) will then take the following form.

$$\frac{\partial^2 u_1}{\partial t^2} = \frac{1}{c^2}\frac{\partial^2 u_1}{\partial t^2} \tag{2.9}$$

Here, $c^2 = \dfrac{\lambda + 2\mu}{\rho}$ with $\lambda = \dfrac{\nu E}{(1+\nu)(1-2\nu)}$ and $\mu = \dfrac{E}{2(1+\nu)}$.

P-wave speed is given by

$$c_p = \sqrt{\frac{\lambda + 2\mu}{\rho}} = \sqrt{\frac{E(1-\nu)}{(1+\nu)(1-2\nu)\rho}}$$

S-wave speed is given by

$c_s = \sqrt{\dfrac{\mu}{\rho}} = \sqrt{\dfrac{E}{2(1+\nu)\rho}}$, and

R-wave speed is approximately expressed in terms S-wave by applying a correction factor [11] as shown below.

$$c_r = \frac{0.87 + 1.12\nu}{1+\nu} c_s$$

Compression wave speed in a plate,

$$c_{pp} = \sqrt{\frac{E}{(1-\nu^2)\rho}}$$

Compression wave speed in a bar,

$$c_{pb} = \sqrt{\frac{E}{\rho}}$$

Note that the speed of pressure waves depends both on the axial and shear resistance properties of the material, while the speed of shear waves depends on the shear properties only. Typical velocities of one-dimensional wave propagation in materials of interest in this study are shown in Table 2.3.

Table 2.3. Acoustic wave velocities for different materials.

Material	Weight density	Velocity of P-wave	Velocity of S-wave	Velocity of R-wave
Steel	490 pcf	16,500 ft/sec	10,273 ft/sec	9,530 ft/sec
Concrete	140 pcf (av)	10,000 to 12,000 ft/sec	5850 to 7100 ft/sec	5750 to 6500 ft/sec
Glass	Variable	13,000 to 16,400 ft/sec	13,000 to 16,400 ft/sec	11,300 to 14,240 ft/sec
Polyethylene	56 pcf	6,400 ft/sec	1,750ft/sec	1,650 ft/sec

The P- and S-waves are reflected at stress-free boundaries. In a plate, multiple reflections can occur if a wave travels back and forth between top and bottom free surfaces. This is known as specular reflection. When a P-wave strikes a boundary at an oblique angle, an S-wave can also be produced by the process of mode-conversion. Likewise, an incident S-wave can produce a P-wave.

2.3.2 Hugoniot Jump Conditions at Shock Front

A shock wave is actually a wave front in motion across which a discontinuous adiabatic jump in state variables like pressure, velocity, and density may exist [12, 13]. In one-D impact situation, the progression of a plane shock wave in a solid is depicted in Fig. 2.7. In time Δt, the shock front travels a distance $\boldsymbol{v_s \Delta t}$. During the same time the deformation is $\boldsymbol{v_p \Delta t}$. Based on definitions in Fig. 2.8, Hugoniot equations for conservation of mass, momentum and energy across a steady shock front can be expressed as below.

$$\rho_o v_s = \rho\left(v_s - v_p\right) \tag{2.10}$$

$$p - p_o = \rho_o v_s v_p \tag{2.11}$$

$$e - e_o = \frac{1}{2}\left(p - p_o\right)\left(\Omega_1 - \Omega_o\right) \tag{2.12}$$

where the subscript ***o*** refers to the material just ahead of the shock front and the subscript ***s*** to the shock front; ***p*** represents pressure, v_p is the particle velocity and u_s shock velocity ahead of the shock front. ***P***, ***e***, and ρ describe the pressure, energy, and density. $\Omega = 1/\rho$ is the specific volume.

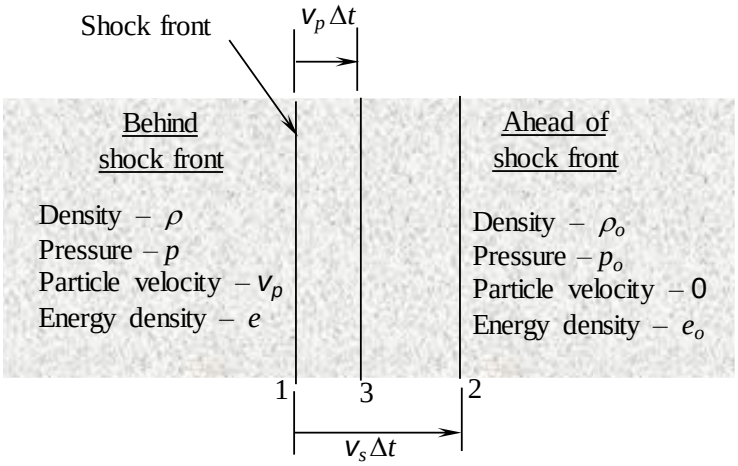

Figure 2.8. Shock wave propagation.

In Eq. (2.11), if p_o is at atmospheric pressure, it can be ignored as compared to *p*, so that

$$p \cong \rho_o v_s v_p \tag{2.13}$$

As there are five unknowns in Eqs. (2.10) to (2.13), the following equation of state relating shock velocity with particle velocity is added.

$$v_s = C_o + s v_p \tag{2.14}$$

The constants C_o and ***s*** can be determined experimentally.

2.4 Blast Effect on Buildings

In Chapter 1, the action of shock wave caused by detonation of explosives on structures was introduced. The nature of damage inflicted on a building or bridge due to the detonation of explosives depends upon the normalized stand-off distance, Z [14], given by Eq. (2.15), is obtained.

$$Z = \frac{R}{W^{\frac{1}{3}}} \tag{2.15}$$

Blast wave propagation in air is a problem of fluid dynamics in which the pressure and flow resulting from the detonation of a large amount of energy in a localized volume. The flow field can be approximated as a lead shock wave, followed by a 'self-similar' subsonic flow field. In simple terms, a blast wave is an area of pressure expanding supersonically outward from an explosive core. It has a leading shock front of compressed gases. The blast wave is followed by a wind blast of negative pressure, which sucks items back in towards the source. The degree of damage resulting from blast wave is determined by the stand-off distance. As this distance becomes smaller, the destructive effect becomes more severe. In other words, as the wave front expands from the source, the intensity of blast energy drops with its distance from the source point. The pressure created by the wave front is most likely to be much greater than other loads considered in a design. However, the duration of the explosion is usually extremely short, measured in milliseconds.

Blast wave reflections also occur within structures, greatly increasing the potential for injury to the occupants and damage to building systems and contents as well as the surroundings. A recent example of this is August 4, 2020, explosion in Beirut, Lebanon, causing more than 200 deaths, 7500 injuries, and property damage worth $15 billion. This was all due to extreme callousness on the part of Beirut Port Authority's storage of large quantities of confiscated ammonium nitrate over a period with proper safety measures. Even in the case of outside blast, when a shock wave encounters a structure, it subjects all surfaces to the force of the blast. If the shock wave enters through windows or door openings, the interior elements, both structural (e.g., floor slabs and columns) and nonstructural (partitions, lighting fixtures, etc.) the contents, and the occupants will also be exposed to the effects of the air blast [15].

As blast waves tend to wrap around objects and buildings, persons or objects behind a large building are not necessarily protected from a blast that starts on the opposite side of the building. To predict how objects will respond to a blast, sophisticated mathematical models like fluid-structure interaction models have been used. The simplest form of a blast wave has been determined and termed as Friedlander waveform. It occurs when a high explosive detonates in a free field, that is, with no surfaces nearby with which it can interact. Blast waves have properties predicted by the laws of wave propagation which may involve diffraction for propagation through narrow openings, and refraction during passage through materials. Consequently, just as in the case of light or sound waves, when a blast wave reaches a boundary between two materials, part of its energy is transmitted, part of it is absorbed, and the remaining part is reflected. The impedances of the two materials determine the relative proportions of the three components.

The idealized representation of temporal variation of pressure with time at a given distance from the source of explosion due to Friedlander [16-18] is shown in Fig. 2.9. After the shock front reaches the target at time t_o it suddenly jumps to the peak incident pressure p_s at time t_s. As the rise time ($= t_s - t_o$) is very short, an instantaneous rise in peak pressure can be assumed [19]. Subsequently, the peak pressure decays to the ambient value in time t_p, and this is the positive phase of the pressure pulse. This is followed by the negative phase characterized by pressures lower than the ambient pressure causing a reversal of the pressure front. As the negative phase does not contribute to the maximum response, it is usually ignored. Therefore, the impulse delivered to the target is taken as the area under the positive phase of the incident pressure-time curve.

The incident peak over pressure p_s gets amplified by a reflection factor as the shock wave encounters a building in its path. The reflection factor is greatest for normal incidence and diminish with increasing deviation from the normal. If the exterior walls of the building are capable to resist the blast, the shock can penetrate through the window and door openings creating mayhem inside the building. The case of internal blast, which is another possibility, was discussed earlier. All blast parameters are primarily dependent on the amount of energy released by a detonation in the form of a blast wave and the distance from the explosion. In Fig. 2.10, the expression for p_s is due to Mills [20].

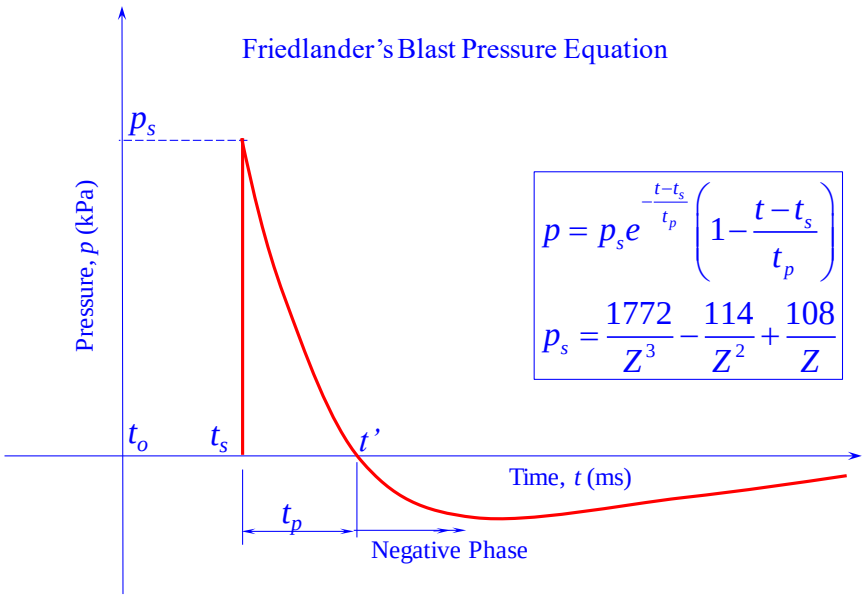

Figure 2.9. Free-field blast pressure vs. time variation.

The air behind the propagating shock-front of a blast wave moves outward with a lower velocity. The corresponding wind pressure (or, velocity) at a point varies with time depending on the peak overpressure ($\boldsymbol{p_s}$) of the blast wave. According to Ngo et al. [17], the maximum air pressure ($\boldsymbol{q_s}$) at a point can be expressed as

$$q_s = \frac{5p_s^2}{2(p_s + 7p_a)} \tag{2.16}$$

As the blast wave front impinges on to a rigid surface, the incident air particle velocity reduces to zero, and the pressure, density and temperature of air are increased to values greater than those of incident blast wave. The resulting reflected overpressure is amplified to twice the incident pressure for weak shocks and higher in the case of stronger shocks. The maximum reflected overpressure p_r [17]can be expressed as in Eq. (2.17).

$$p_r = 2p_s\left(\frac{7p_a + 4p_s}{7p_a + p_s}\right) \tag{2.17}$$

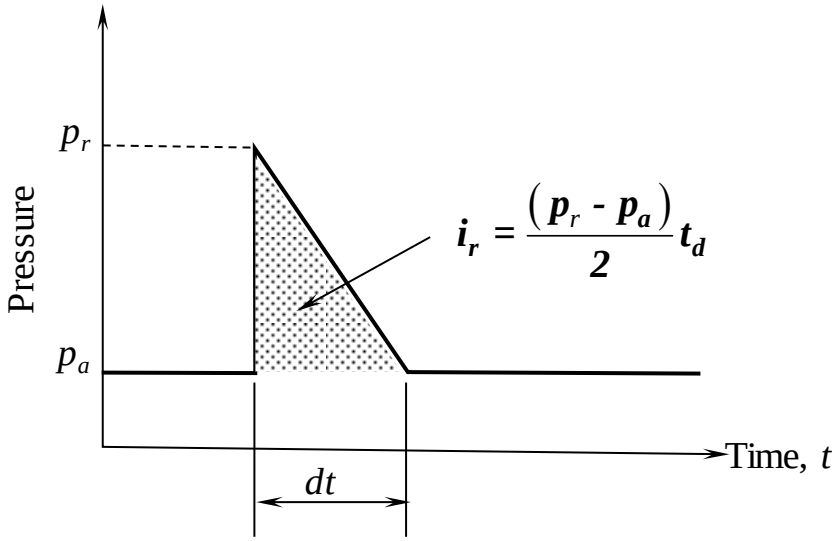

Figure 2.10. Approximation of shock wave pressure.

As shown in Fig. 2.10, the reflected overpressure is, sometimes, idealized by an equivalent triangular pulse of maximum peak pressure p_r and time duration t_d for the overpressure to be dissipated giving the reflected impulse given by [21].

$$i_r = \frac{1}{2}(p_r - p_a)t_d \tag{2.18}$$

Over the years, the DoD has developed methods to calculate blast load on structures [22-24] They have put forward very useful tools for defining the blast loads first by introducing charts for calculating the blast load parameters, in terms of normalized stand-off distance (Z) in the case of spherical and hemispherical wave fronts [22]. These charts covered a limited number of idealized cases only and were replaced by restricted access software like CONWEP (Conventional Weapons Effects) [25,26], a software developed by USACE (United States Army Corps of Engineers). It is a collection of conventional weapons effects calculations covering many practical situations for air blast, projectile penetration, cratering, ground shock, etc. Air blast capabilities include free air and surface burst calculation and loads on exposed surfaces accounting for angle of incidences. Another useful software from USACE is BLASTX to perform calculations of the shock wave and confined detonation products, pressure and venting for explosions either internal

or external to a structure. A more recent tool is BEC (Blast Effect Computer) [27] which is optimized air blast effect prediction is claimed to give values closer to measured values.

To define Z, apart from what is stated above, a number of possibilities exist like those standardized or recommended by various organizations such as DoD's Unified Facilities Criteria [28], ASCE's Blast Protection of Building Standard [29], DHS's Risk Management Series FEMA 426, and GSA's Progressive Collapse and Design Guidelines. For instance, UFC 4-010-02 [28] establish standards that provide minimum levels of protection against terrorist attacks for the occupants of all DoD inhabited buildings. Therefore, using the available tools, the characteristics of incident and reflected pressures on structures caused by an explosion can be determined reliably without difficulty, unless the center of source of blast is very close to the structure (which happens when $Z < 1.5$).

CHAPTER 3

MATERIAL PROPERTIES AND CONSTITUTIVE RELATIONSHIPS

3.1 Material Properties

The materials of interest in this study are concrete, reinforcing steel, glass, and laminated polyethylene. In Section 3.2, the relevant mechanical characteristics of these materials are expounded. In addition, the applicable mathematical models for these materials are examined. In the case of concrete: the uniaxial, biaxial and triaxial stress vs. strain characteristics in tension and compression are considered. The confining effect of concrete on its compressive strength is critically scrutinized. In the context of triaxial strength, the relationship between hydrostatic pressure and volumetric strain used to define the equation of state for concrete is evaluated. In the case of steel rods, plate glass and polyethylene film, uniaxial strength characteristics are looked into. In all cases, the strain-rate effect on strength characteristics is elucidated.

3.1.1 Concrete

Structural concrete, the most widely used construction material in the world, has also found extensive use in structures requiring protection from destructive effects of blast and projectile impact. Although concrete with compressive strengths as high as 250 MPa has been produced, it is treated as a quasi-brittle material because of its low tensile strength, which may vary between 6 to 11% of its compressive strength. The lower percentage is typical of ultra-high strength concrete. To impart the tensile stress resistance capability, discretely placed supplemental higher strength material like steel is embedded in the concrete. Accordingly, to increase structural resistance against blast and impact loading effects, apart from supplemental steel reinforcement, various strengthening measures like prestressing and bonded fiber reinforced polymers have been considered.

To be able to accurately model the behavior of both normal and strengthened concrete structural elements, it is, first, necessary to understand the nature of failure modes of structural elements of interest under projectile impact and blast effect, both before and after the strengthening measures are undertaken. In Chapter 2, the nature of response of concrete slab panels to such extreme effects was explained. For instance, depending upon the speed of hurled projectile

impinging the slab orthogonally, various failure patterns like penetration, spalling, cratering, and perforation were identified. Also, the possibilities of purely local, global or a combined failure mode were recognized. In the case of blast loading, however, the response mainly tends to be global in nature. The simulation model needs to be equipped with the capability to reproduce such behaviors, before being identified as an appropriate tool for evaluating the performance of a particular strengthening measure. In doing so, first, the strength characteristics of concrete used in the structure needs to be identified. In addition to quasi-static tensile and compressive stress-strain characteristics of concrete in a three-dimensional stress field, the loading rate effects need due attention. To determine its strength properties, as per ASTM standards, requires testing in uniaxial compression and tension [30, 31]. For tensile strength of concrete, the uniaxial test is often replaced by the more convenient indirect test known as Brazilian split-cylinder test [32]. These tests are undertaken in quasi-static loading conditions. Under dynamic loading conditions, namely, impact loading, the strength properties like tensile strength, compressive strength and elastic modulus apparently exhibit elevated values as compared to those obtained under quasi-static loading conditions. Such enhancement is often accounted for by multiplying the quasi-static values with a strain-rate dependent Dynamic Increase Factor (*DIF*). Assuming different values in tension and compression. These factors are normally obtained by using Klosky (Split-Hopkinson) bar test on cylindrical concrete specimen [33].

3.1.2 Concrete in Uniaxial Compression (UXC)

The two well-recognized simple failure mechanisms of concrete are cracking under tension and crushing under compression [34]. The cracking stress level is an order of magnitude smaller than the crushing stress level. In a complex three-dimensional stress field, the failure pattern is also complex, requiring the identification of inelastic behavior by defining the yield surface and flow rule. To be able to define these properties, a series of strain-controlled compression tests are performed on representative cylindrical concrete specimens. A typical compression stress-strain curve resulting from such tests is shown in Fig. 3.1. It exhibits nearly elastic behavior up to a stress level around 40% of compressive strength. Beyond this point, the behavior is essentially inelastic with initial strain-hardening till the peak stress ($f_c^{'}$) is reached. Beyond the peak point the material is progressively weakened due to micro-cracking, leading to strain-softening and eventual failure by crushing.

Being highly inhomogeneous, standard concrete test specimen are bulky (typically 4in dia.×8in long) and generation of such curves requires high-capacity testing machines, which are not available in most situations. As a result, the only available experimental data is often the average compressive strength ($f_c^{'}$) of concrete using an ultra-high-capacity compressive testing machine meant for the purpose and the initial or elastic part of the stress-strain curve using a conventional UT machine to get the value of elastic modulus, E_c . Given the early part of the stress-strain curve, the value of elastic modulus is obtained using the ASTM Standard [31] formula given below.

$$E_c = \frac{(S_2 - S_1)}{(\varepsilon_2 - \varepsilon_1)} \tag{3.1}$$

Here, E_c = chord modulus of elasticity, MPa.

S_2 = stress in MPa corresponding to 40% of ultimate load.

S_1 = stress in MPa corresponding to a longitudinal strain, ε_1 (=5E-5).

ε_2 = longitudinal strain with stress S_2 .

In Fig. 3.1, under monotonic loading conditions, the change in strain from the elastic limit strain ε_2 to the ultimate strain ε_{cu} is the measure of total inelastic strain till failure occurs in compression. If the values of the test parameters appearing in Eq. 3.1 are not available, the formula shown in Eq. 3.2 based on unit weight of concrete (w_c) and its 28-day compressive strength ($f_c^{'}$) can be used to approximately predict the value of E_c [32].

$$E_c = 0.043 w_c^{1.5} \sqrt{f_c^{`}} \tag{3.2}$$

Given the values of $f_c^{'}$ and E_c , it is necessary to predict the full f_c vs ε_c curve so that nonlinear behavior and damage behavior can be specified in the material model with a reasonable degree of accuracy. In Fig. 3.1, three regions can be identified, such as elastic ($f_c < 0.4 f_c^{'}$), strain-hardening ($\varepsilon_c \le \varepsilon_{co}$), and strain-softening ($\varepsilon_c > \varepsilon_{co}$). In the strain-hardening region, the total strain

in concrete, ε_c, will comprise of a plastic component, ε^p, and an elastic component, ε_e, which is the strain recovered upon unloading from stress level f_c. Note that the elastic strain recovery, ε_e, shown in Fig. 3.1 is based on the original elastic modulus, E_c.

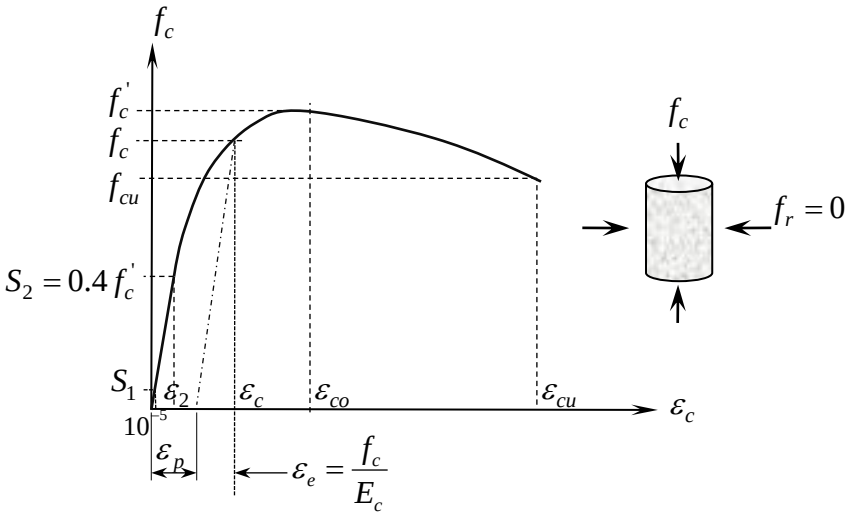

Figure 3.1. Typical stress-strain diagram for concrete in axial compression (UXC Test).

Due to micro-cracking, which grows as the strain is increased beyond the peak stress point, progressive softening of the material occurs leading to a reduction in the value of elastic modulus to, say, $E_d < E_c$, the value of which continues to drop with the progression of damage. In a strain-controlled experiment, the drop in stress from the peak value is an indication of the degree of damage. For strains beyond the elastic limit, the inelastic component of strain, ε^p $(= \varepsilon_c - \varepsilon_e)$ appears prominently in Concrete Damage Plasticity (CDP) models for concrete [35, 36]. In continuum damage mechanics, material degradation in most damage models is characterized as a macroscopic state variable d_c, ignoring the details of growth and distribution in a material element. The damage variable is often treated as an indicator of the degradation of the value of elastic modulus E_d. In the case of concrete, this damage parameter can be used to define the reduced elastic modulus after the onset of the softening process. If d_c = 0, it signifies no damage condition and the effective elastic modulus is E_c. On the other hand, d_c = 1 signifies full damage appearing as crumbled concrete, when 0< d_c <1, the state of damage as reflected by the reduced value of the effective elastic modulus as

$$E_d = (1 - d_c) E_c \tag{3.3}$$

The corresponding stress at a point in the damaged is defined as

$$f_c = E_d(\varepsilon_c - \varepsilon_p) = E_d(1 - d_c)(\varepsilon_c - \varepsilon_p) \tag{3.4}$$

As shown in Fig. 3.1, in the strain-hardening region where $d_c = 0$, the plastic component of strain is based on E_c. Allowing for progressive degradation of concrete properties, the unloading path in the stress vs strain plot appears as in Fig. 3.2. In the post-peak region, the damage parameter can be defined as $d_c = 1 - f_c / f_c^{'}$. The plastic strain can then be obtained from: $\varepsilon^p = \varepsilon_c - \frac{1}{1-d_c} \cdot \frac{f_c}{E_c}$.

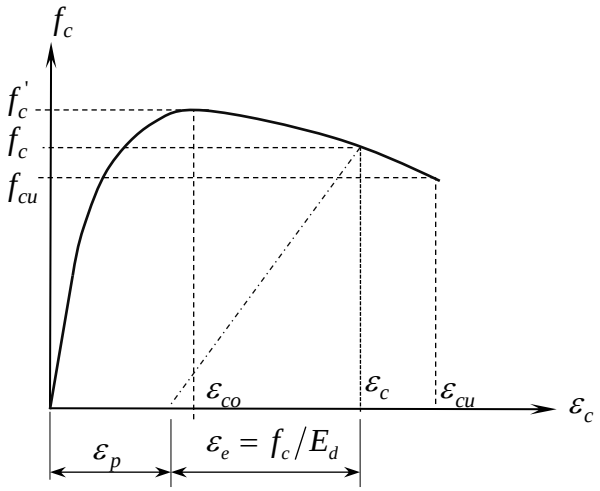

Figure 3.2. Stress-strain curve in compression strain components after damage.

Prediction Formulas for Stress-Strain Curves for Concrete in Compression

Due to practical experimental limitations faced by the researcher, the complete experimental stress vs. strain curve of concrete could not be experimentally generated in-house. The way out of it is to identify the most appropriate formula among the myriads of empirical prediction formulas available in the published literature [37-41]. Based on the commonly used

assumption that the rising or strain-hardening part of the curve is parabolic and that crushing strength (f_c) as well as elastic modulus (E_c) of a given concrete are known, the stress vs. strain equation, at least, for the rising part, will be

$$f_c = E_c \varepsilon_c \left[1 - \frac{\varepsilon_c E_c}{4 f_c'} \right] \tag{3.5}$$

The secant modulus, E_{co}, is defined as f_c'/ε_{co}, where strain ε_{co} corresponds to $f_c = f_c'$. However, for a parabolic stress-strain curve $E_c = 2E_{co}$ which in turn means $E_c = 2 f_c'/\varepsilon_{co}$. Substituting for E_c in Eq. (3.5) and setting $r_\varepsilon = \varepsilon_c/\varepsilon_{co}$, the following alternative form of Eq. (3.5) is obtained.

$$f_c = r_\varepsilon \left[2 - r_\varepsilon \right] f_c' \tag{3.6}$$

Eq. (3.6) is similar to the formula put forward by Hognestad [37]. He, however, defined the descending or softening branch of the curve by a straight line originating from the peak stress point. His expression is shown in Eq. (3.7).

$$f_c = \left[1 - 0.15 \frac{r_\varepsilon - 1}{\varepsilon_{cu}/\varepsilon_{co} - 1} \right] f_c' \tag{3.7}$$

Here, ε_{cu} is the crushing strength of concrete. Using the measured strength properties of the concrete used in this study, such as $f_c' = 41.94$MPa and $\varepsilon_{co} = 0.002$, the stress-strain plot based on Eqs. (3.6) and (3.7) is shown in Fig. 3.3. Using these strength values, according to Hognestad formula,

$$E_c = 2 \times 41.94 / 0.002 = 41{,}940 \text{ MPa}$$

This value is significantly different from the measured typical value of $E_c \cong 30,000\text{MPa}$, based on the UXC compression test undertaken by the author.

Due to this anomaly, other published formulas were examined; the general form of most of these formulas is

$$f_c = f_c' r_\varepsilon e^{[1-r_\varepsilon]}$$

After series expansion of the exponential term and retention of the first four terms only leads to

$$f_c = \frac{2.7182\, f_c' r_\varepsilon}{1 + r_\varepsilon + 0.5 r_\varepsilon^2 + r_\varepsilon^3 / 6} \tag{3.8}$$

Most of the other published formulas [38-41] are generic forms of this formula. For instance, based on the numerical analysis of available test data, Popovics [41] proposed the following formula for obtaining f_c corresponding to a given value of r_ε.

$$f_c = \frac{\kappa f_c' r_\varepsilon}{(\kappa - 1) + r_\varepsilon^\kappa} \tag{3.9}$$

when f_c' is in MPa, $\kappa = 1 + 0.058 f_c'$.

The estimation of the strain values (ε_{co} and ε_{cu}) at peak and failure stresses, respectively, follows. The magnitude of f_c' is influenced by compressive strength and rate of loading during the quasi-static test. For a given strain rate and load duration, say, as per ASTM standards, the peak point strain has been predicted by empirical formulas [39]. For instance, according to Popovics [41] ε_{co} can be estimated from

$$\varepsilon_{co} = 0.000875\, f_c'^{0.25} \tag{3.10}$$

Based on his experimental results, Majewski [84] proposed the following more accurate formula for the same purpose.

$$\varepsilon_{co} = 0.00014\left[2 - e^{-0.024 f_c^{'}} - e^{-0.014 f_c^{'}}\right] \simeq 0.002 \tag{3.11}$$

He also put forward the following widely used empirical formula for estimating the failure strain of concrete, ε_{cu}.

$$\varepsilon_{cu} = 0.004 - 0.0011\left[1 - e^{-0.0215 f_c^{'}}\right] \simeq 0.0035 \tag{3.12}$$

Hereinafter, the values: ε_{co} =0.002 and ε_{cu} =0.0035 will be used.

The plot of the formulas for stress-strain curve mentioned above appears in Fig. 3.4. The curve shown (as proposed by the author) is based on cubic spline fitted formula in the strain-hardening segment and quadratic spline fitted in the strain-softening segment, as described below.

For strain-hardening segment:

$$f_c = a r_\varepsilon + b r_\varepsilon^2 + c r_\varepsilon^3 \tag{3.13}$$

Here, $a = \varepsilon_{co} E_c$; $b = 3 f_c^{'} - 2 E_c \varepsilon_{co}$; and $c = -2 f_c^{'} + E_c \varepsilon_{co}$

For strain-softening segment:

$$f_c = a' + b' \varepsilon_c + c' \varepsilon_c^2 \tag{3.14}$$

In this equation, $a' = \dfrac{[(r_\varepsilon^{'} - 2) + r_f] f_c^{'}}{(r_\varepsilon^{'} - 1)^2}$; $b' = \dfrac{2 r_\varepsilon^{'} (1 - r_f) f_c^{'}}{(r_\varepsilon^{'} - 1)^2 \varepsilon_{co}}$; and $c' = -\dfrac{(1 - r_f) f_c^{'}}{(r_\varepsilon^{'} - 1)^2 \varepsilon_{co}^2}$ with

$r_\varepsilon^{'} = \dfrac{\varepsilon_{cu}}{\varepsilon_{co}}$ and $r_f = \dfrac{f_{cu}}{f_c^{'}}$.

In this figure, the proposed plot corresponds to the case $f_{cu} = 0.85 f_c'$. This stress vs. strain curve, which agrees closely with the Popovics curve, is used in this study.

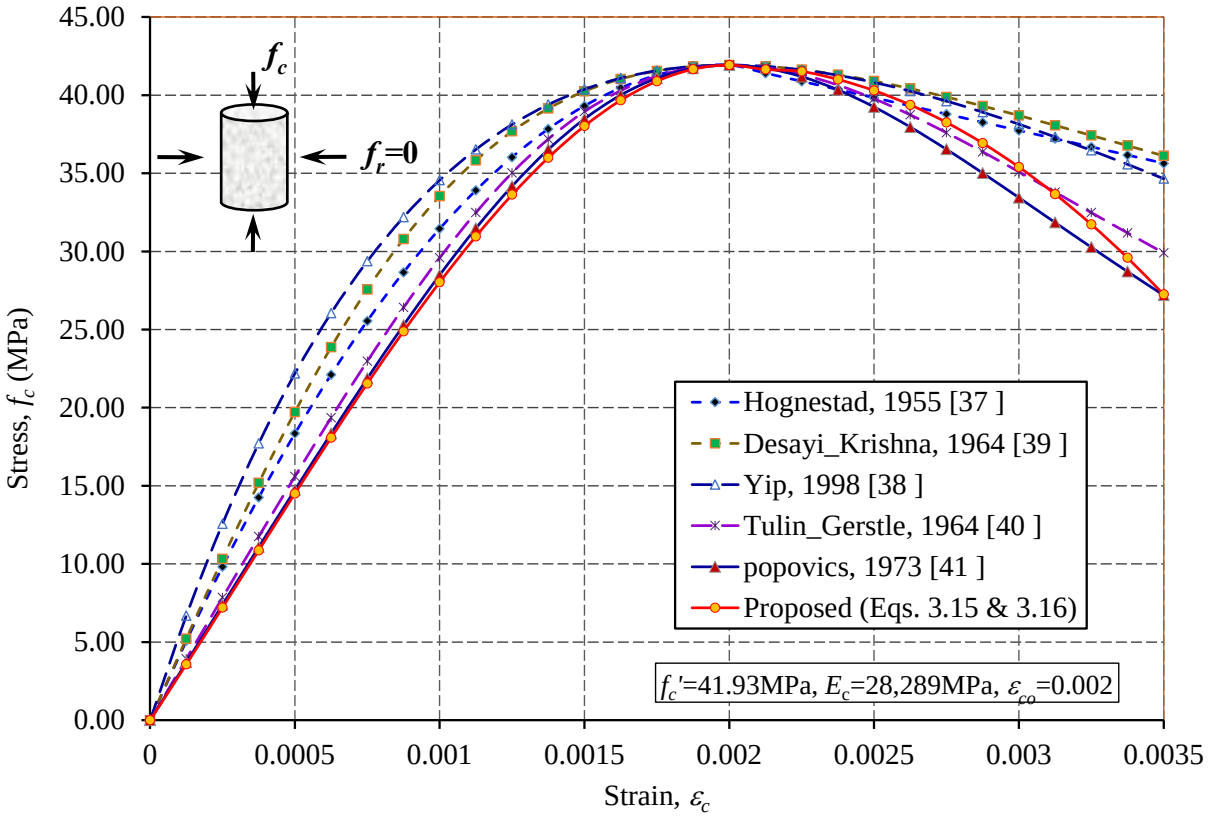

Figure 3.3. Stress vs. strain curves for concrete in axial compression.

3.1.3 Concrete in Triaxial Compression (TXC)

In Section 3.1.1, the quasi-static uniaxial compression behavior of concrete used in the present study was presented. In the case of projectile impact problems involving penetration and piercing of concrete target, a complex multiaxial state of localized stress is created in the vicinity of the impact area. During impact, the concrete ahead of the projectile path may experience radial confining effect of the surrounding concrete mobilizing its shear and tensile strengths. Hence, the damage process in concrete at and in the immediate vicinity of the projectile impact area is prone to triaxial behavior, requiring consideration of the influence of radial confining pressure on compressive strength as well as shear strength of concrete. Such behavior can be determined experimentally using a highly complex and very expensive special purpose triaxial compression test equipment, which is normally available in large specialized laboratories only and is naturally

beyond the reach of researchers at Vanderbilt University. The issue of confined compressive strength of concrete was first addressed by Richart et al. [42] followed by Gardner [43], Li et al. [44] and others. A view of the triaxial compression test equipment of 1340 kN-capacity located in US Army Engineering Research Laboratory at Vicksburg, MS, used for generating the type of experimental data considered herein is shown in Fig. 3.5 [45]. In Refs. [45-47], details of the test procedure and experimental results for triaxial testing of high-strength concrete are outlined. Experimental data presented in these references are based on tests undertaken at ERDC laboratories under the Hardened Structures Research Program of the U.S. Army Corps of Engineers. The triaxial strength of concrete has been found to be significantly higher than uniaxial and biaxial strengths. However, the biaxial strength of concrete was found to be slightly higher than the uniaxial strength [79].

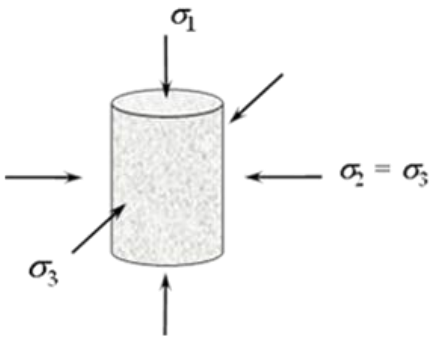

Figure 3.4. Stresses in triaxial (TXC) test.

The TXC test of concrete is undertaken under two loading conditions in terms of the way the axial stress (namely, σ_1) and radial (or, confining) stress (namely, $\sigma_2 = \sigma_3$) are applied to the test specimen. Referring to Fig. 3.4, (a) Hydrostatic Test is used to determine the relationship between the mean normal stress, $p = (\sigma_1 + \sigma_2 + \sigma_3)/3 = \sigma$, and volumetric strain, $\varepsilon_v = \varepsilon_1 + 2\varepsilon_3$. So, in this case, the specimen is subjected to different hydrostatic pressure levels in the pressure vessel and corresponding strain components are measured using LVDTs and strain gages; (b) Deviatoric test mobilizes the shear strength of concrete by performing a series of tests to determine axial failure corresponding to different values of confining pressure, which is kept constant during the duration of each test, to get the relationship between the principal stress difference, ($\sigma_1 - \sigma_3$) and axial strain (ε_1).

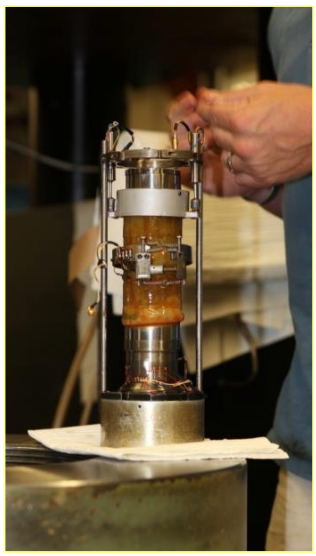

(a) Specimen instrumentation

(b) Triaxial test apparatus

Figure 3.5. Triaxial compression test machine.

Study of triaxial behavior of concrete was undertaken by Ahmad et al. [48], Sfer et al. [49], Nordendale [45], Heard [47], Mills et al. [50], Attard et al. [51] and others. For this purpose, the test results of cylindrical concrete specimen under different confining pressures were considered. Fig. 3.6, shows typical curves of $(\sigma_1 - \sigma_3)$ vs. ε_1 for ultra-high strength concrete with f_c' = 216 MPa [45]. Despite these successes, the problem of generating actual test data for a given concrete remained. So, the author focused on identifying generic empirical formulas reflecting the behavior in reliable test data available in the published database. Such formulas enabled the prediction of the behavior of a given concrete with different levels of confinement, utilizing minimal test data based on UXC test results. Such efforts were undertaken by Sammani et al. [52], Binici [53], Lim et al. [54] and others. In Fig. 3.7, the rising branch of the stress vs strain curve appears to be parabolic, as in the case of UXC test. Beyond the peak point, the descending branch has a gentle downward slope culminating in a stable plateau. Such post-peak behavior is due to the resistance offered by the cohesive strength concrete followed by the mobilization of frictional resistance in the presence of confining pressure. Moreover, the peak strength of confined concrete is a function of the confining pressure. The downward tail of the plots is a result of discontinuation of test after a certain level of strain is reached.

In this study, the well vetted prediction formulas by Lim and Ozbakkaloglu [54] were used. As shown in Fig. 3.7, the critical parameters appearing in the formulas for confined concrete are

peak strength ($f_{cc}^{'}$), corresponding strain (ε_{co}^{c}) and the residual strength (f_{res}^{c}) defined in terms of $f_c^{'}$, f_r and ε_{co} shown in Eqs. 3.15a, 3.15b and 3.15c. Here, f_r denotes the radial confining pressure. The stresses are expressed in MPa.

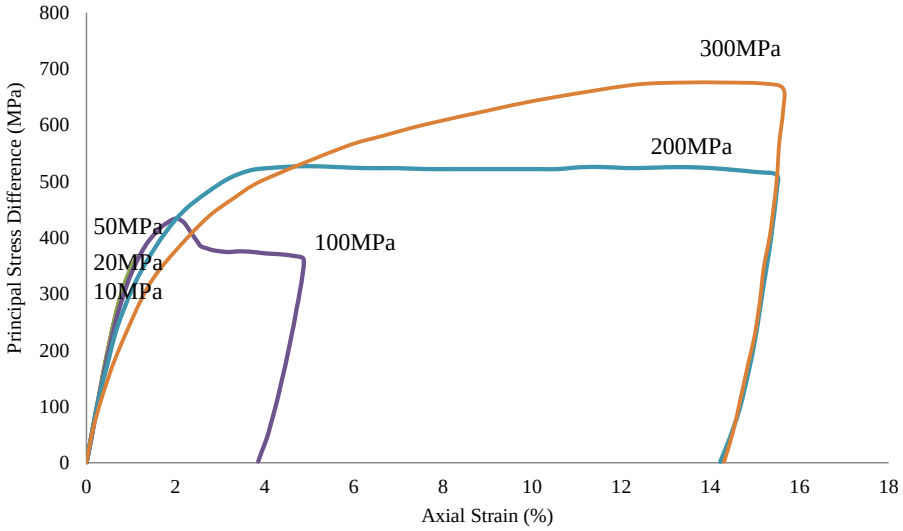

Figure 3.6. TXC test results for UHSC with f_c'=216 MPa [45].

$$f_{cc}^{'} = f_c^{'} + 5.2(f_c^{'})^{0.91}\left(\frac{f_r}{f_c^{'}}\right)^{(f_c^{'})^{-06}} \tag{3.15a}$$

$$\varepsilon_{co}^{c} = \varepsilon_{co} + 0.045(f_c^{'})^{0.91}\left(\frac{f_r}{f_c^{'}}\right)^{1.15} \tag{3.15b}$$

$$f_c^{res} = 1.6 f_{cc}^{'}\left(\frac{f_r^{\,0.24}}{f_c^{'0.32}}\right),\ f_c^{res} \le f_{cc}^{'} - 0.15 f_c^{'} \tag{3.15c}$$

The strain hardening part of the stress-strain curve is defined by

$$f_c = \frac{f_{cc}^{'}(\varepsilon_c / \varepsilon_{co}^{c})r}{r - 1 + (\varepsilon_c / \varepsilon_{co}^{c})^r},\ 0 \le \varepsilon_c \le \varepsilon_{co}^{c} \tag{3.16}$$

where $r = \dfrac{E_c}{\left(E_c - f_{cc}^{'}/\varepsilon_{co}^{c}\right)}$. The post peak part of the curve is defined by

$$f_c = f_{cc}^{'} - \frac{f_{cc}^{'} - f_c^{res}}{1+\left(\dfrac{\varepsilon_c - \varepsilon_{co}^{c}}{\varepsilon_{ci}^{c} - \varepsilon_{co}^{c}}\right)},\ \varepsilon_c > \varepsilon_{co}^{c} \tag{3.17}$$

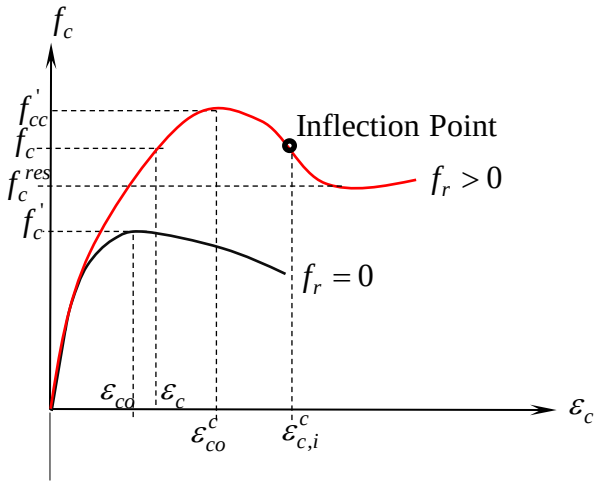

Figure 3.7. Critical parameters of confined compression.

In Eq. (3.17), the prediction expression for axial strain corresponding to the inflection point, $\varepsilon_{c,i}^{c}$, in the post-peak branch of the curve is given by

$$\varepsilon_{c,i}^{c} = \left(\frac{\rho_{c,f}}{2400}\right) 0.4\left[2.8\varepsilon_{co}^{c}\left(\frac{f_c^{res}}{f_{cc}^{'}}\right) f_c^{'-0.12} + 10\varepsilon_{co}^{c}\left(1 - \frac{f_c^{res}}{f_{cc}^{'}}\right) f_c^{'-0.47}\right] \tag{3.18}$$

Here, $\rho_{c,f}$ is density of concrete in kg/m^3.. These prediction formulas are based on data from cylindrical test specimens with aspect ratio of 2. After successful evaluation of these formulas with respect to available test data [45], the stress vs strain curves for the concrete used in the study for different level of confining stress were obtained. For $f_c^{'} = 41.93$ MPa the plots for different levels of confining pressure are shown in Fig. 3.8. The plots are based on the values of critical

parameters shown in Table 3.1 obtained by using Eqs. (3.15a to 3.15c). These plots allow for confining effect on the failure surface of concrete in the 3-D stress space.

Table 3.1. Data used for plots in Fig. 3.8.

f_r (MPa)	10	20	50	100	200	300	Remarks
ρ_{cf} (kg/m^3)			2,400				UXC Test
f'_c (MPa)			41.93				
E_c (MPa)			28,288				
ε_{co}			0.002				
ε_{co}^c	0.01066	0.0212	0.0571	0.124	0.273	0.454	Eq. 3.17b
$f_{cc}^{'}$ (MPa)	91.5	128.1	221.2	353.9	584.9	792.7	Eq. 3.17a
f_c^{res} (MPa)	76.95	121.8	214.9	347.6	578.6	786.4	Eq. 3.17c
$\varepsilon_{c,i}^c$	0.019	0.0378	0.102	0.222	0.487	0.779	Eq. 3.21

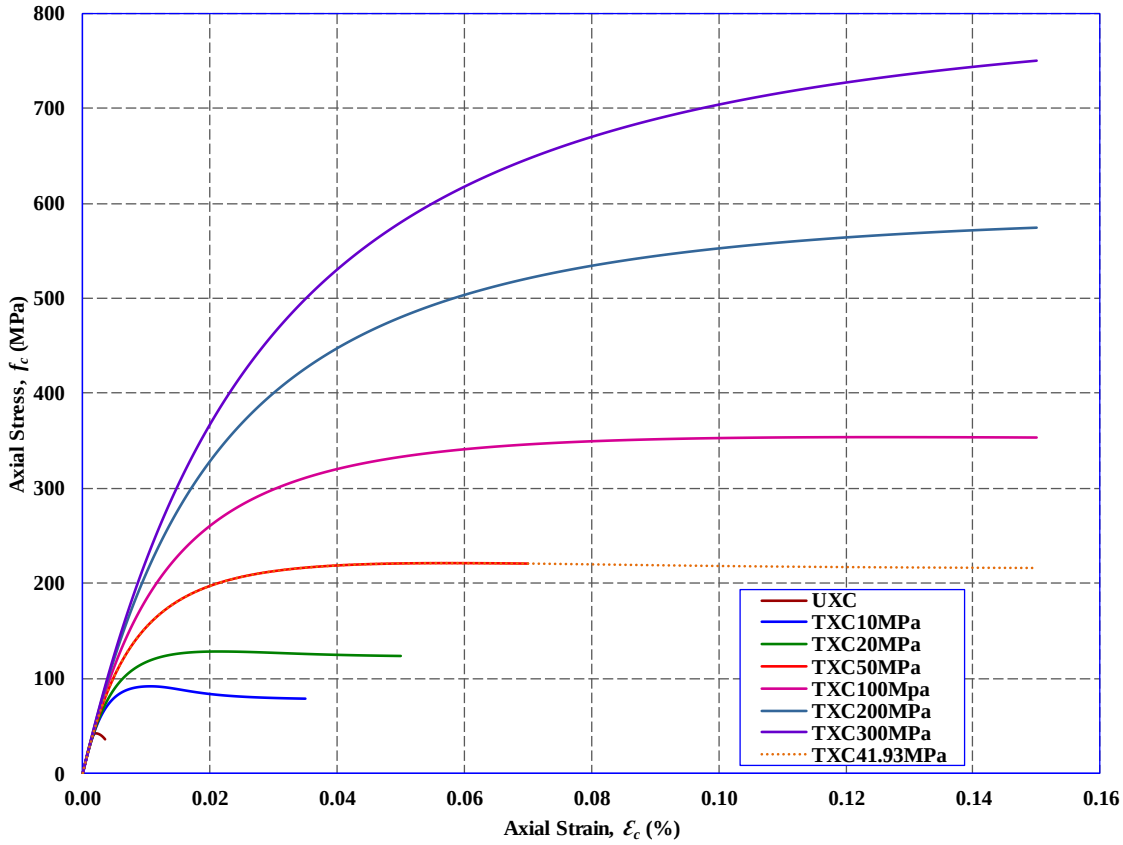

Figure 3.8. Predicted TXC curves for concrete used in this study ($f_c^{'}$ =41.93 MPa).

Such data can also be used to generate the parameters for the equation of state which is the relationship between hydrostatic pressure (p) vs. volumetric strain (ε_v), a typical plot [55] of which is shown in Fig. 3.9. In this plot, up to Point 1 the behavior is elastic, beyond Point 1 water and air-filled voids in the concrete collapse creating eventually a compacted solid mass at Point 2. Beyond this point, the compacted mass exhibits high linear stiffness.

In the p vs ε_v plot of Fig. 3.9, ε_v is commonly denoted by the density parameter μ which is defined as relative change in density; so that, $\varepsilon_v = \mu = (\rho - \rho_o)/\rho_o$, where ρ_o and ρ are original and current densities. Using the modified notation, in the elastic stage, $\mu_{crush} = p_{crush}/K$, where the elastic bulk modulus $K = E_c/3(1-2\nu_c)$ and $p_{crush} = f_c^{'}/3$. For $f_c^{'} = 41.93$ concrete, $E_c = 28,289$ MPa and $\nu_c = 0.15$ giving $K = 13471$ MPa and $\mu_{crush} = 0.0010375$.

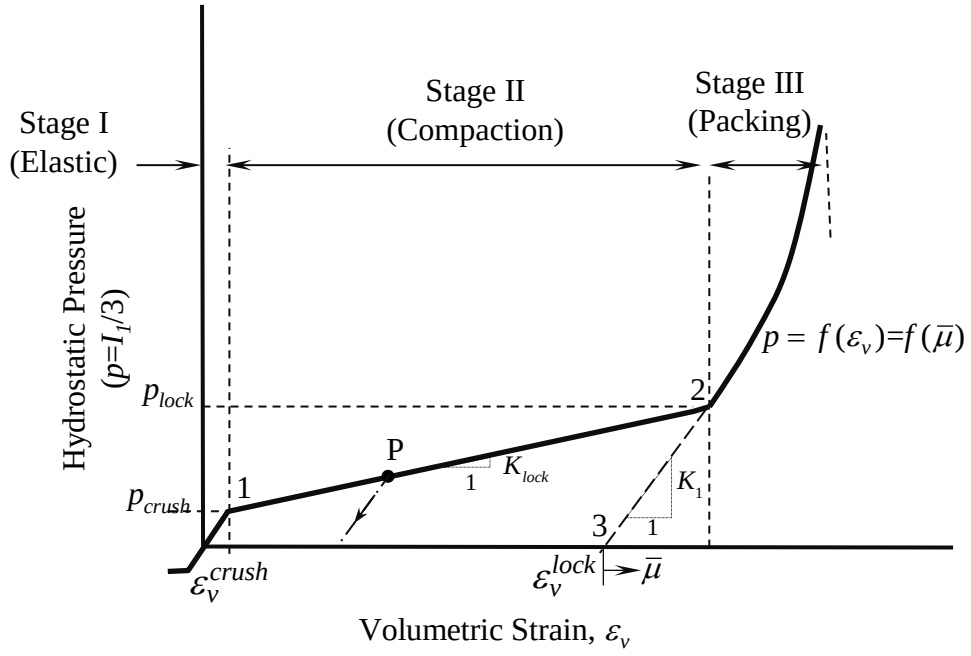

Figure 3.9. Hydrostatic pressure vs. volumetric strain.

Stage II is the transition stage caused by plastic deformation coupled with closure of pores. During loading, the pressure is given by:

$$p = p_{crush} + K_{lock}(\mu - \mu_{crush}) \text{ with } K_{lock} = (p - p_{crush})/(\mu_{lock} - \mu_{crush})$$

On the other hand, during unloading from (say, Point P) the slope of the unloading path is K_1 (which appears in Eq. 3.19):

$$p = p_{crush} + K_{lock}(\mu_P - \mu_{crush}) - K_1(\mu_P - \mu)$$

Here, μ_{lock} is defined as $(\rho_{grain} - \rho_o)/\rho_o$, where ρ_{grain} is the average density of concrete without voids given by $\rho_o/(1-n)$ where n is the porosity of the original concrete. According to Roy et al. [56], at 28 days, the porosity of normal strength concrete with and without admixtures varies from 8 to 14%. Using the median value of 11%, $\rho_{grain} = 1.1236\rho_o$ giving the value of μ_{lock} as 0.11236.

The variation of p in Stage III is expressed in terms of the following cubic equation:

$$p = f(\bar{\mu}) = K_1\bar{\mu} + K_2\bar{\mu}^2 + K_3\bar{\mu}^3, \ \bar{\mu} = \frac{\mu - \mu_{lock}}{1 + \mu_{lock}} \tag{3.19}$$

μ_{lock} being the value ε_v at Point 3. Note that for Eq. (3.19) Point 3 is used as the local origin. The coefficients K_1, K_2 and K_3 are material constants based on triaxial and SHPB test data.

3.1.4 Concrete in Tension

Determination of tensile strength of concrete using direct axial test is difficult to undertake and is prone to significant scatter. Therefore, indirect methods, such as Brazilian split-cylinder test (ASTM C96) and modulus of rupture test (ASTM C78) are preferred. Being a quasi-brittle material, the tensile stress-strain curve is mostly linear, except near the cracking point, as shown in Fig. 3.10. According to ACI-318, split-cylinder tensile strength and modulus of rupture can be approximated by $f_{spt} \approx 0.56\sqrt{f_c'}$ N/mm^2 and $f_{rt} = 0.62\sqrt{f_c'}$ N/mm^2. The direct tensile strength of concrete has been found to be close to 90% of f_{spt}. In Fig. 3.10, f_{spt} is the tensile strength of concrete and ε_{to} is the corresponding strain. The fracture strain is ε_{tu}. The elastic modulus in

tension, $E_t = E_c$. Cracking is initiated when $\varepsilon_t = \varepsilon_{to}$. If $\varepsilon_t \geq \varepsilon_{to}$, plastic strain in tension, $\varepsilon_t^p = \varepsilon_t - \dfrac{f_t}{E_{dt}}$ and the damage parameter in tension is denoted by d_t,

$$f_t = E_{dt}(\varepsilon_t - \varepsilon_t^p) = E_c(1-d_t)(\varepsilon_t - \varepsilon_t^p) \tag{3.20}$$

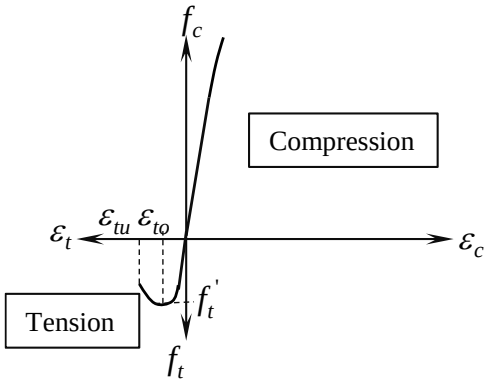

Figure 3.10. Stress vs. strain plot of concrete in tension.

Stress-Strain Curves of Concrete in Tension

According to Wang et al. [57], the stress vs. strain relationship can be defined as below.

Before cracking:

$$f_t = E_c\varepsilon_t,\ \varepsilon_t \leq \varepsilon_{cr} \tag{3.21}$$

After cracking:

$$f_t = f_t'\left(\frac{\varepsilon_{cr}}{\varepsilon_t}\right)^n,\ \varepsilon_t > \varepsilon_{cr} \tag{3.22}$$

In Eq. (3.22) the exponent *n* controls the rate of degradation. Carreira et al. [58] put forward the following general formula.

$$\frac{f_t}{f_t^{'}} = \frac{\beta\left(\frac{\varepsilon_t}{\varepsilon_{to}}\right)}{\beta - 1 + \left(\frac{\varepsilon_t}{\varepsilon_{to}}\right)^{\beta}} \tag{3.23}$$

Here, the exponent β determines the shape of tensile stress-strain curve. As this expression is of the same form as Popovics' formula (Eq. 3.11) for concrete in compression, it is desirable that the value of β is set equal to κ in Eq. 3.9, so that E_t and E_c have the same magnitude. Based on several experimental studies, ε_{to} is often assigned the value of 0.0002. Not surprisingly, this value is 10% of the previously defined value for ε_{co}.

The Equation of State for negative pressure (tension) is given by $p = K\mu \leq T$ (Fig. 3.9). Here, T is the limiting hydrostatic tensile pressure for the material. On modification for damage, the limiting value is $T(1-d_t)$.

3.1.5 Strain-Rate Effects in Concrete

Mechanical properties of engineering materials are affected by the rate of load application. Typical example of such a state is impact and blast loading of concrete panels. Strain rates associated with a range of loadings in real life situations are given in Fig. 3.11. It is well documented that material stress-strain behavior is greatly influenced by the rate of loading. The conventional understanding is that, when the strain-rate increases, the yield and ultimate strengths of steel get amplified. In the case of concrete, the compressive strength, tensile strength, and the slope of the descending portion of the stress-strain curve of concrete change. The strain-rate effect is also understood to be inversely proportional to strength of steel or concrete. This effect is, sometimes, attributed to

- Rate sensitivity to the presence of viscous pore fluid (Stefan effect)
- Alteration of path of micro-crack propagation causing preferential cracking through regions of high strength
- Inertial effects in the lateral direction

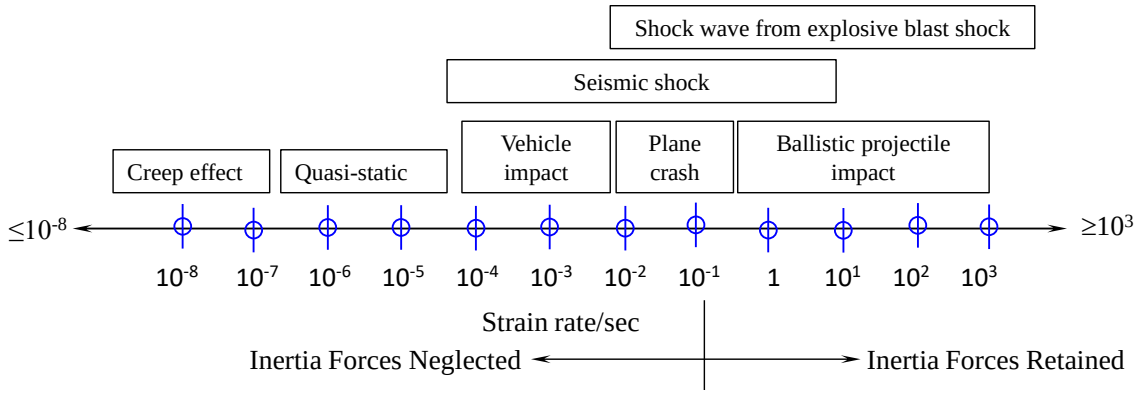

Figure 3.11. Strain rates associated with the loading spectrum.

To remove the inconsistencies and resulting confusion related to the nature of loading rate effects on concrete strength [59, 60, 61], Tedesco et al. [61] and others undertook Split-Hopkinson (or, Kolsky) Pressure Bar (SHPB) test. A strain rate of 5 to 6/sec was found to have minimal impact on the tensile strength. However, at higher strain-rates the effect was found to be more pronounced. This increase is represented as the ratio of dynamic strength to static strength and is called as Dynamic Increase Factor (DIF). But questions about markedly higher values in compression (DIF_c) as compared to those in tension (DIF_t) even after the removal of the effects of background noise during SHPB test caused by the scattering effect of the incident shock wave were addressed by Heard et al. [62]. They modified the SHPB test by inserting a appropriately designed copper ring pulse shaper at the impact end of the incident bar. This also helped to reduce the inertial effect of the striker. The hypothesis of some researchers was that the abnormally higher value of DIF_c as compared to DIF_t is most likely caused by the radial inertia effect in the SHPB test specimen.

Dynamic Increase Factor in Tension (DIF_t)

Several empirical formulas of $DIF_t = f_t^d / f_t$, mainly, based on experimental data have been proposed [63, 64, 65, 66, 67, 68, 69]. In 1983, Gebbeken et al. [63] suggested the following empirical formula for DIF_t to represent the shape of the curve conveniently allowing curve fitting with experimental and/or numerical data.

$$DIF_t = \left\{ \left[\tanh\left(\log\left(\frac{\dot{\varepsilon}}{\dot{\varepsilon}_o} \right) - C_1 \right) C_2 \right] \left[\frac{C_3}{C_4} - 1 \right] + 1 \right\} C_4 \tag{3.24}$$

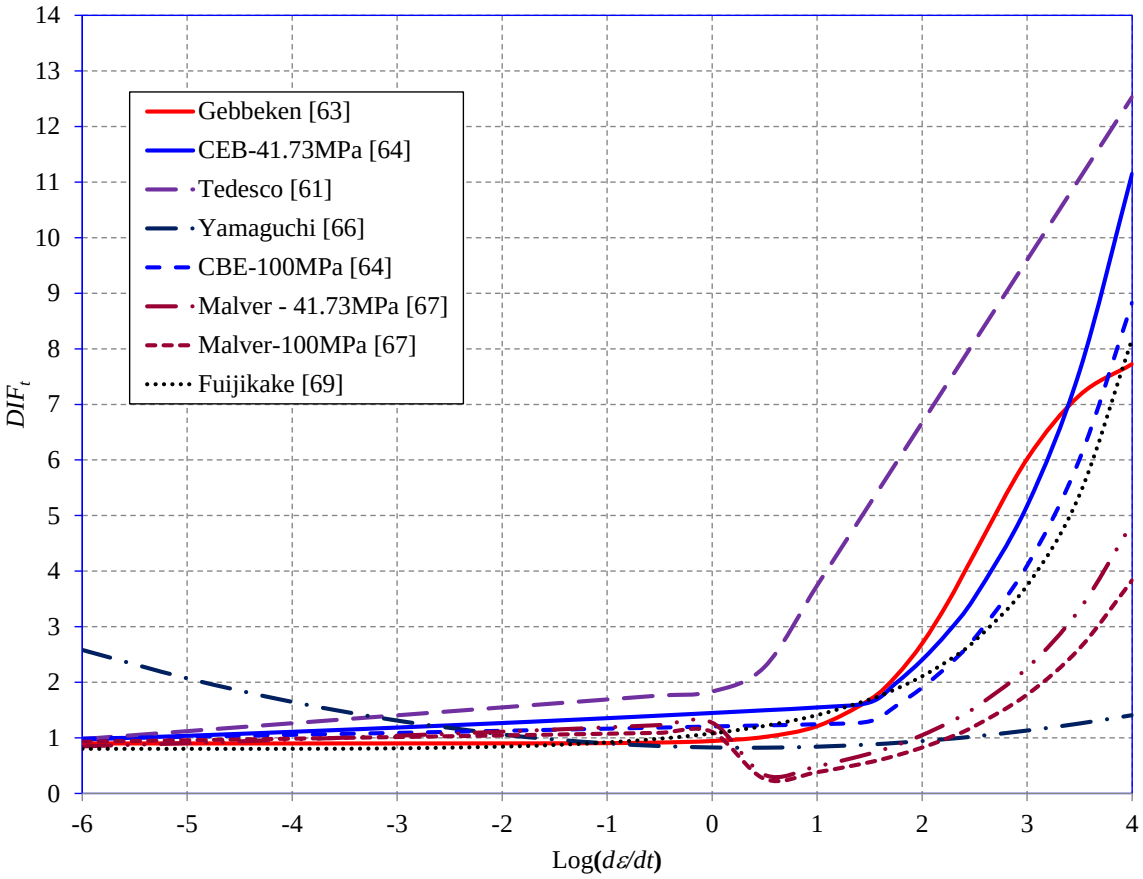

Figure 3.12. Comparison of different empirical formulas.

In Eq. (3.24), C_1, C_2, C_3 and C_4 are constants to best fit the curve with available data, $\dot{\varepsilon}$ is the applied strain rate, $\dot{\varepsilon}_o$ is the reference strain rate, usually assigned the value of 10.0/sec. As a best fit to the empirical formulas mentioned above the constants in Eq. (3.24) were found to assume the following values: C_1 =1.55, C_2 =0.8, C_3 =9, and C_4 =4.5. Based on these values, the plot of Eq. (3.24) is shown Fig. 3.12, along with the plots with other empirical formulas. All the formulas are independent of compressive strength of concrete except those of CEB [64] and Malver et al. [67]. For these two cases, the plots for both $f_c^{'}$ = 41.73 MPa and 100 MPa are shown but the magnitude of $f_c^{'}$ seems to have only a small effect on DIF_t, with higher strength concrete showing somewhat lower value. It is also evident from the figure that the curve for Eq. (3.24) based on the aforementioned values of the constants represents a good average fit to the empirical formulas and has three identifiable segments: i) a lead plateau when strain rates (≤0.1/sec) are low and has negligible dynamic effect on the tensile strength; ii) a gently rising strain rate effect over

the range 0.1/ to 1/sec strain rate; and iii) finally when $\dot{\varepsilon} > 1/\sec$, the strain-rate effect picks up at a faster rate but slows down slightly as it approaches the very high strain rate of 104/sec.

According to Lu et al. [70], the results of numerical simulation of tensile tests based on rate-independent constitutive model led him to believe that the dynamic tensile strength measured in, say, dynamic splitting test and direct tensile test models can solely be attributed to material effect. This assertion agrees with the findings of previous investigators. Hence, one may safely conclude that the dynamic tensile strength increase factors of Fig. 3.12 can solely be attributed to material response.

Dynamic Increase Factor in Compression (DIF_c)

In the case of compressive SHPB test as well, the high frequency noise effect gets minimized by using again the approach developed by Heard, et al. [62]. Using rate-independent concrete constitutive model based numerical simulation of SHPB tests, first, by Li et al. [71] followed by Hao et al. [72], it was concluded that inertial confinement plays an important role in the experimentally observed dynamic strength enhancement in SHPB compression tests and the empirical formula based on such test results overestimate the material strain-rate effects. Li et al. [71] proposed the following formula for compressive strength increase factor including the inertia effect.

$$DIF_c = \begin{cases} 1 + 0.03438(\log\dot{\varepsilon} + 3), & \dot{\varepsilon} \le 10^2 s^{-1} \\ 8.5303 - 7.1372\log\dot{\varepsilon} + 1.729(\log\dot{\varepsilon})^2, & \dot{\varepsilon} > 10^2 s^{-1} \end{cases} \tag{3.25}$$

In Fig. 3.13, the predictions by Eq. (3.25) are compared with the predictions based on the formulas in [64, 65, 68, 69]. It appears that the curve based on Eq. (3.25) lacks the characteristic wiggle present in other curves.

The curves for DIF_c shown in Fig. 3.13 have not been explicitly corrected for inertia effects. Before proceeding further, it is helpful to evaluate the plots shown in Fig. 3.13. At low strain-rates ($\dot{\varepsilon} < 0.1/\sec$), for all curves except those based on [65] and [68] $DIF_c \cong 1$. It signifies that at low strain-rates concrete strength is not affected and in the same token one may assume that

inertia effects are also negligible. To remove the inertia component from DIF_c observations with other materials can be used.

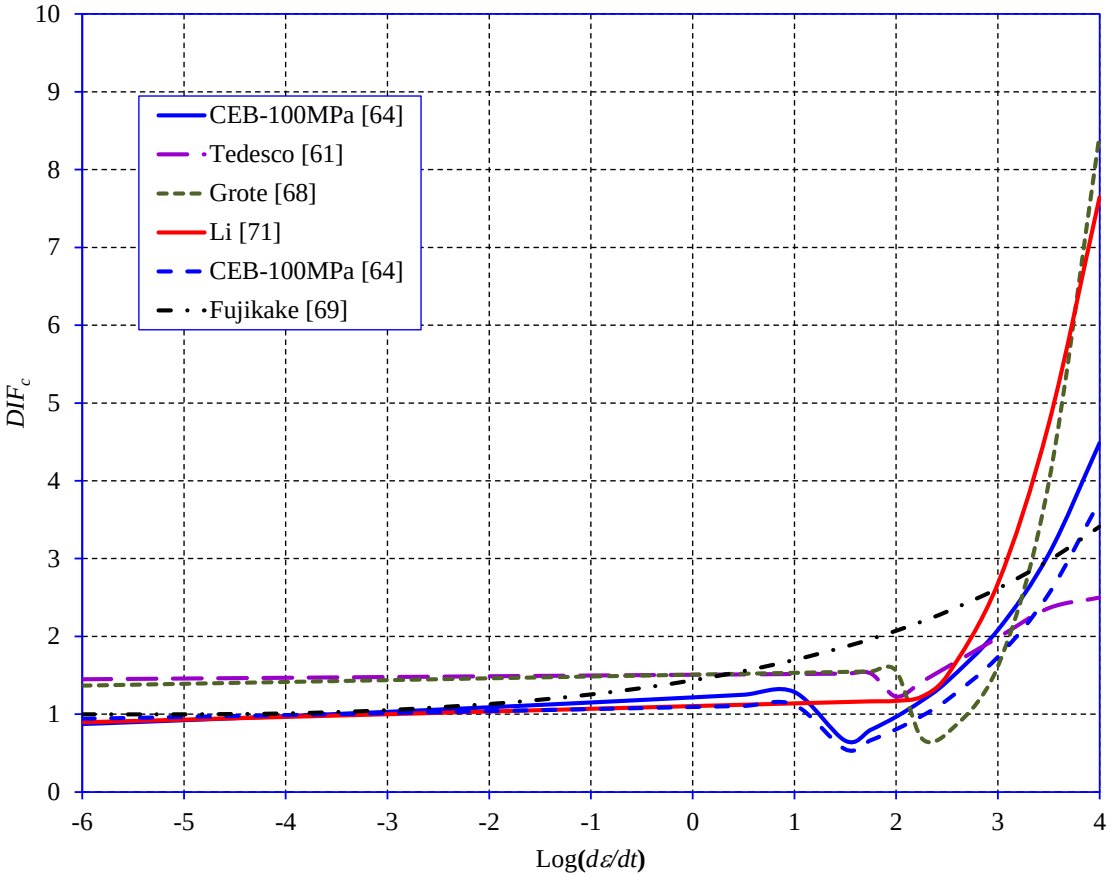

Figure 3.13. Verification of Eq. 3.25 with other empirical formulas.

The only prediction empirical formula for DIF_c free of inertia effects, based on experimental investigation, is reported by Li et al. [71] which will help validate the effort to isolate/remove the inertia effect. In the case of other materials (especially, polycrystalline ones) the relative increase in tensile and compressive strengths due to material strain-rate effects have been found to be the same [72], so that $DIF_{c-i} = DIF_t$. Based on this premise, it can be shown that the contribution of inertia effect on compressive strength (f_c^i) is

$$f_c^i = f_c^d - f_t^d \left(\frac{f_c'}{f_t} \right) \tag{3.26}$$

Dividing both sides of Eq. (3.26) with $f_c^{'}$ means, for concrete,

$$DIF_c^i = DIF_c - DIF_t \tag{3.27}$$

Unfortunately, of all the formulas for DIF_c and DIF_t, only those of CEB [65] are dependent upon both $f_c^{'}$ and $f_t^{'}$. Hence, Eq. (3.27) is amenable for direct application to CEB formulas only. Two values of $f_c^{'}$, specifically 41.73 MPa and 100 MPa, and corresponding $f_t^{'}(=0.494\sqrt{f_c^{'}}$ MPa) are used to compute DIF_i using Eq. (3.27). The resulting plots along with the corresponding segmental trend lines are shown in Fig. 3.14.

Table 3.2. Coefficients of quintic trend line for DIF_i shown in Fig. 3.14.

Power m in $\left(\frac{d\varepsilon}{dt}\right)^m$	5	4	3	2	1	0	R^2
$f_c^{'}=41.7$MPa	0.0002	0.0051	0.0379	0.1152	0.1397	0.2231	0.9976
$f_c^{'}=100$MPa	0.0004	0.0065	0.041	0.109	0.155	0.3392	0.9986

In subsequent discussions the coefficients corresponding to the second equation will be used, because of its closer proximity to zero for small strain rates. It will be interesting to determine DIF_c based on one of the trend lines for DIF_i, coefficients for which are shown in Table 3.2.

To arrive at a representative formula for DIF_t, all the acceptable prediction formulas were considered, and the following representative formula was arrived at by regression analysis.

$$DIF_t = \begin{cases} 0.0415\log\dot{\varepsilon} + 1.1577, & \log\dot{\varepsilon} < 1 \\ -0.0924(\log\dot{\varepsilon})^3 + 1.308(\log\dot{\varepsilon})^2 - 2.4828\log\dot{\varepsilon} + 2.4658, & \log\dot{\varepsilon} \geq 1 \end{cases} \tag{3.28}$$

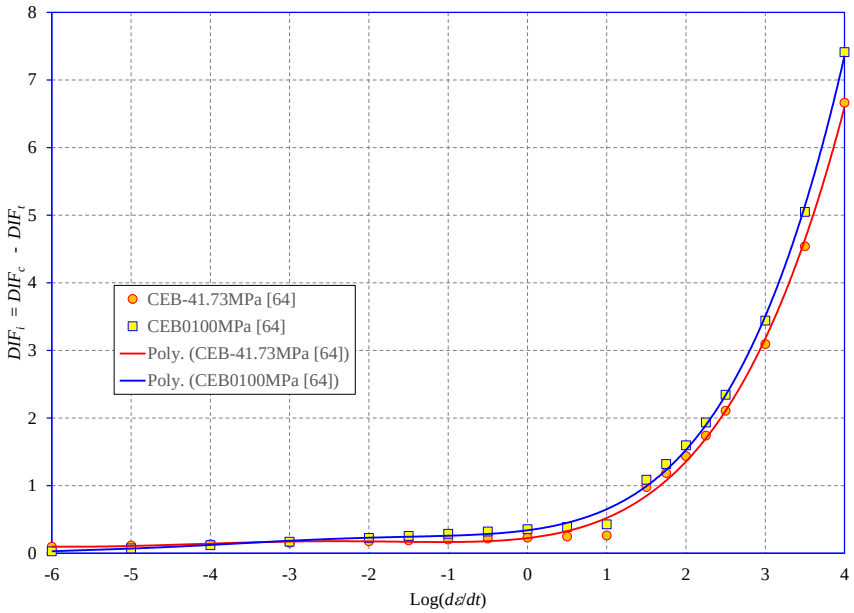

Figure 3.14. Variation of inertial component DIF_i with Log ($d\varepsilon/dt$).

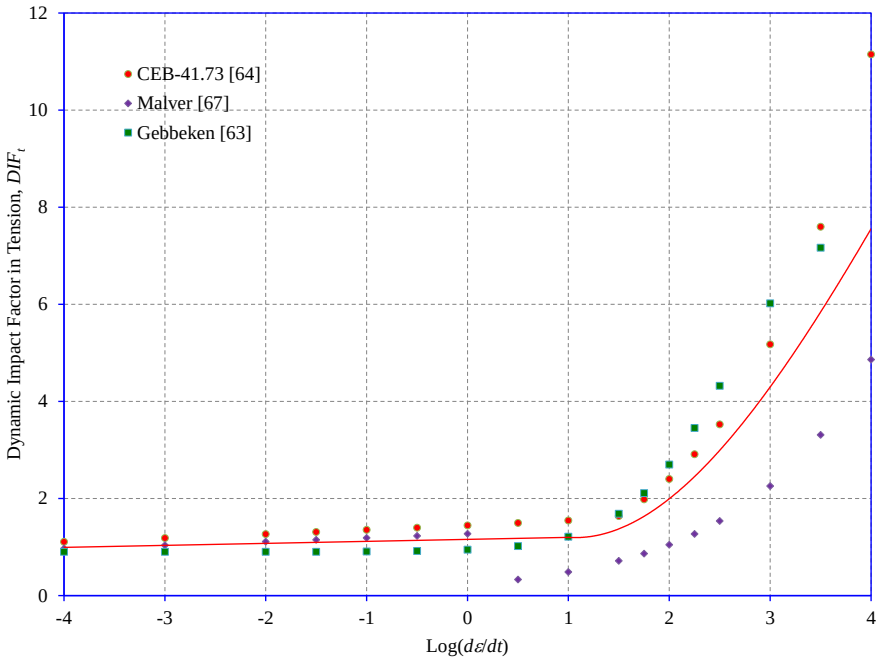

Figure 3.15. Trendline for dynamic impact factor in tension.

Plot of this new prediction is shown as solid red line in Fig. 3.15 along with two of the well-known ones. Eq. 3.28 is used in this research. Plot of predicted DIF_c based on DIF_t and DIF_i

is shown in Fig 3.16 and 3.17 along with those from [63], [64] and [67]. Reasonable correlation is noted.

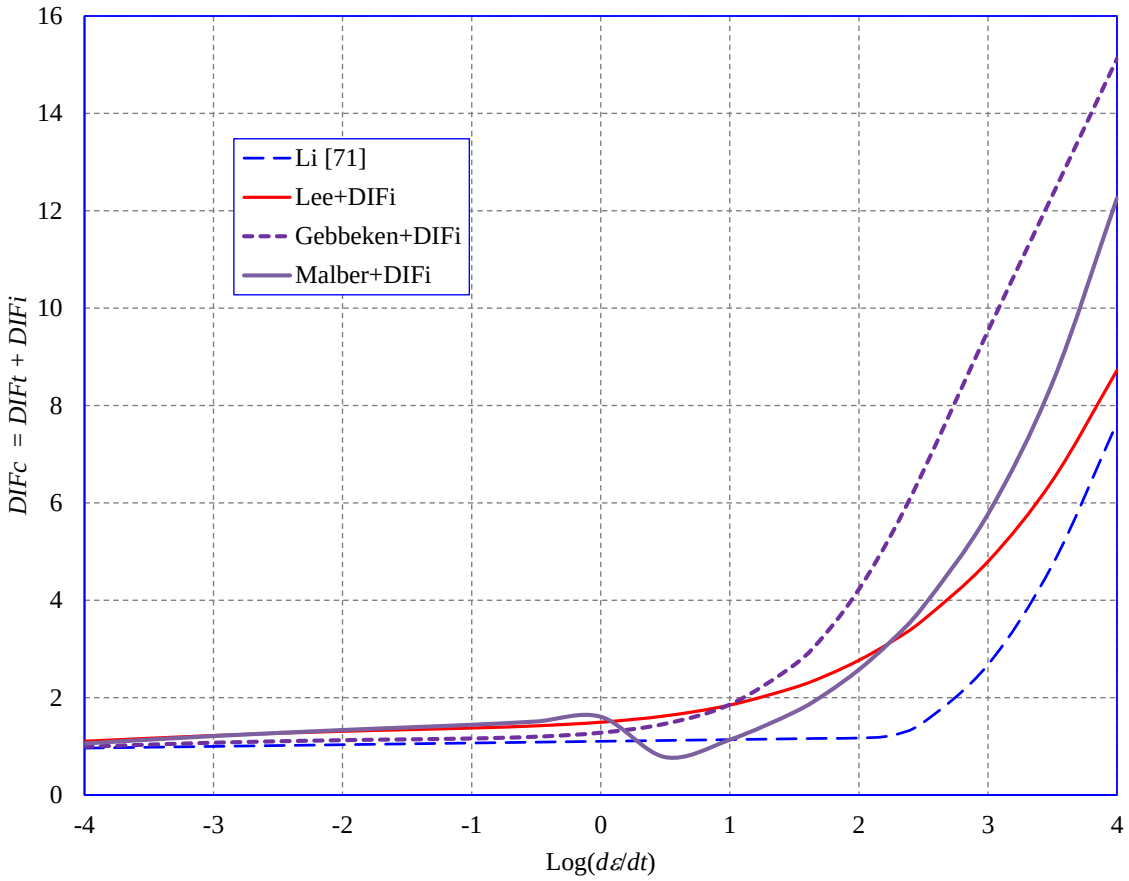

Figure 3.16. DIF_c prediction based on DIF_i.

Plots based on proposed prediction equation for *DIF* in comparison with those from [61], [64] and [65]. Excellent correlation of the proposed equation with those of Gebbeken [63] and CEB [64] is noteworthy. Also, plot based on HJC equation with the original value of constant C modified from 0.007 to 0.033, shows good agreement up to strain rate of 34 in/sec.

3.2 Steel Reinforcement

The cladding panels are reinforced with mats of steel rods in top and bottom to increase resistance against tensile forces which in turn increases ductility. Both quasi-static tensile behavior and strain-rate effects are considered.

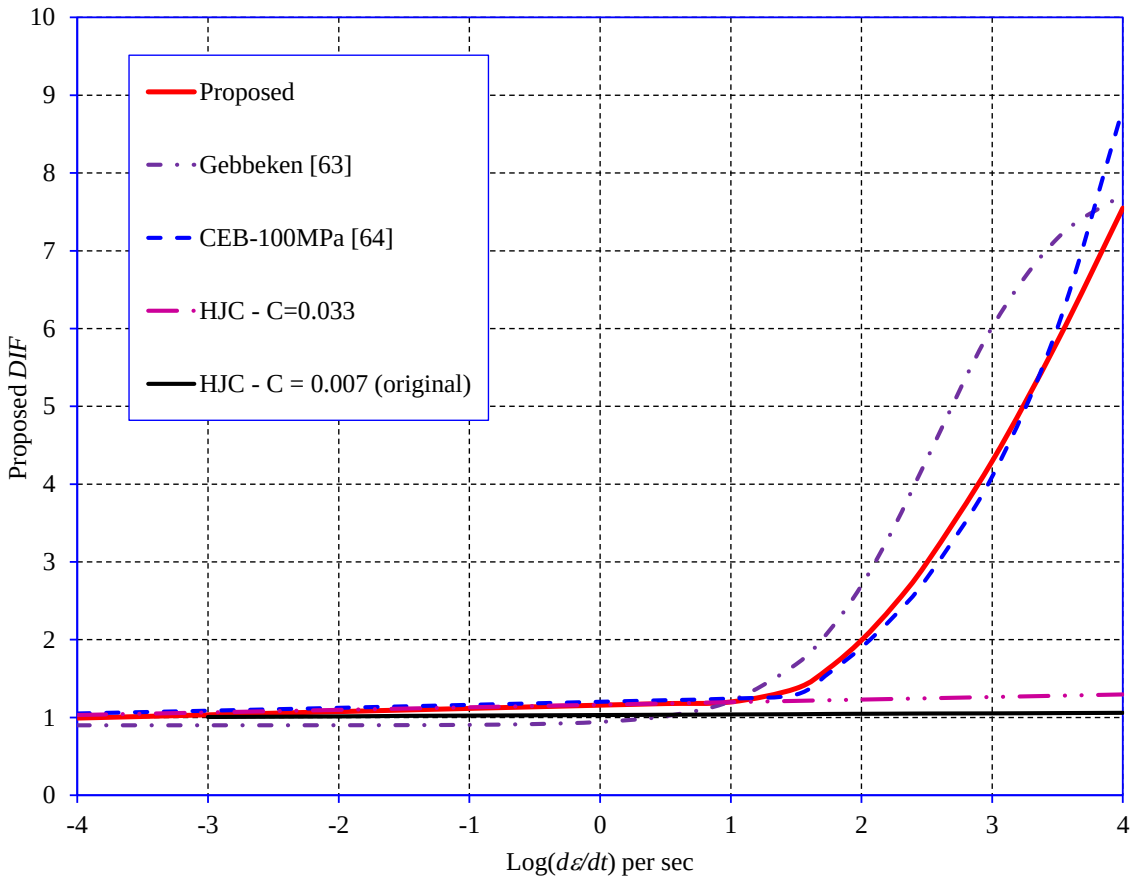

Figure 3.17. Comparison of proposed *DIF* .

3.2.1 Stress-Strain Curve

Typical stress–strain curves of steel rods used in reinforced concrete structures are obtained from tension tests, in which the loads are monotonically applied (without any unloading) until the failure of standard test specimen [73]. The typical tensile stress vs strain curve for ASTM Grade 60 reinforcing steel rod is shown in Fig. 3.18 is typical of low-carbon steel. The well-defined yield point stress, f_y = 414 MPa or 60 ksi.

Stress as well as strain values at critical points like proportional limit (or yield), ultimate and fracture are shown. A plastic plateau, which is absent in strain-hardened and high strength steels, corresponding to the yield point is also evident. In reinforced concrete structures, certain amount of reinforcement ductility is important. The common approximation for stress-strain curve for steel is elastic-perfectly plastic, with perfectly plastic behavior ranging from $\varepsilon_s = \varepsilon_y$ to ε_{su} .

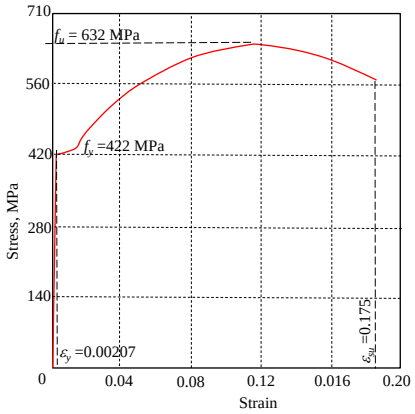

Figure 3.18. Typical stress vs. strain curve for Grade 60 reinforcing steel used in the study.

3.2.2 Strain-Rate Effect in Steel

Typical stress vs strain curves for low-carbon steel with strain-rate is shown in Fig. 3.19 and 3.20, under quasi-static and dynamic loading conditions. It is clear from the figure that both strength parameters of interest, that is, yield and ultimate strength, are enhanced under dynamic loading conditions, to an equal degree for tension and compression. According to Rao et al. [74], the dynamic increase factor for steel yield stress in ksi units is defined below.

$$DIF_s = \frac{f_y^d}{f_y} = 1 + \kappa \dot{\varepsilon}^n \tag{3.29}$$

where, $k = 0.021$ and $n = 0.26$ for ASTM A36 or equivalent steel. $k = 0.20$ and $n = 0.18$ for ASTM A441 or equivalent steel. For all other grades of steel,

$$DIF_s = 1 + \frac{3.2 + 0.001\dot{\varepsilon}}{f_y} \tag{3.30}$$

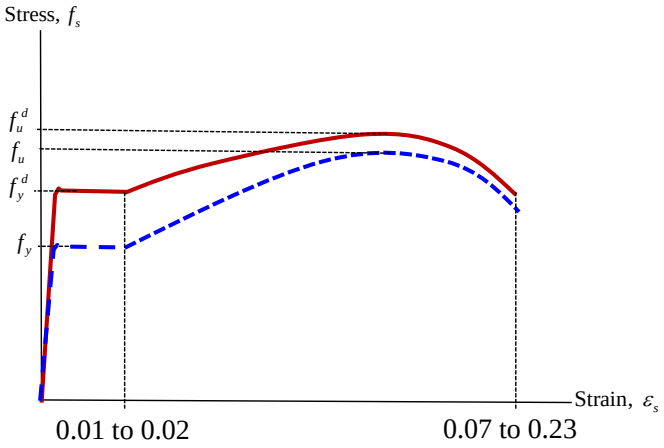

Figure 3.19. Typical quasi-static and dynamic stress-strain curve for low carbon steel.

More recently, according to Fujikake et al. [69], Takahashi put forward the following logarithmic DIF_s formula for steel.

$$DIF_s = \frac{f_y^d}{f_y} = 1.202 + 0.04\log(\dot{\varepsilon}) \tag{3.31}$$

Generally speaking, $DIF_s \approx 1.0$ for low strain rates between, say, 10^{-5}–10^{-3}. For higher strain, the effect of strain rate can be considered in terms of one of the formulas, given above.

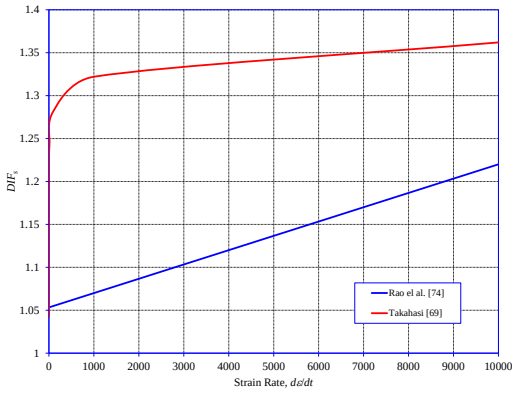

Figure 3.20. DIF vs. strain-rate for steel.

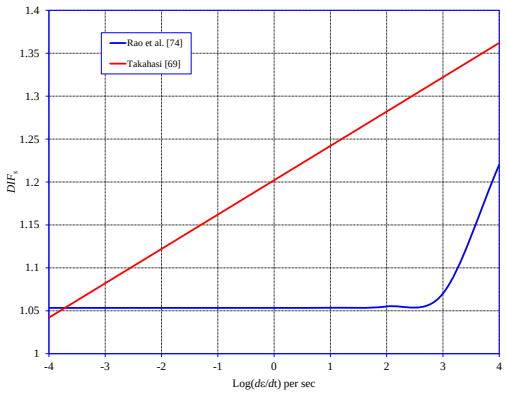

Figure 3.21. DIF vs. log(strain-rate) for steel.

Plots of Eqs. (3.29) and (3.31) are shown in Fig. 3.20 in terms of strain and in Fig. 3.21 in terms of logarithm of strain-rate. In this equation, the rate effect rises rapidly in lower strain range and does so at a much slower rate for higher strain rates. In contrast, with Eq. (3.29) the rate of increase of *DIF* is constant irrespective of the strain rate value. Although Eq. (3.29) is more convenient to use, in this study the more recent Eq. (3.31) is used.

3.2.3 Glass

Glass is used in this study as glazing for window openings. It is an amorphous material characterized by brittle behavior and is associated weakness in tension, which can be attributed to its non-crystalline molecular structure. So, if glass is stressed in tension beyond its strength limit, breakage occurs immediately without warning. Despite this shortcoming glass finds extensive use in many applications because it is transparent and resistant to scratching. Most widely used glass in construction is 'float glass' formed by pulling glass ribbons through a tin bath and exited on rollers in a temperature-controlled annealing kiln where it is cooled avoiding residual stresses. Depending upon the nature of heat treatment three groups of glass can be identified – annealed/heat-strengthened, tempered, and laminated glass. When impacted the heat-strengthened glass tends to break into large pieces with sharp corners and tend to fly off, see Fig. 3.22 (a).

Tempered glass is a type of safety glass processed by controlled chemical and thermal treatment inducing surface compressive stresses of about 70 MPa. It is about four times stronger than annealed glass of equal thickness. On impact it breaks into numerous small pieces which remain in the frame, reducing the potential for serious injury by flying glass pieces, as shown Fig. 3.22 (b).

Laminated glass is a type of safety glass in which two or more plies of glass are sandwiched with one or more interlayers of 0.02" to 0.06" (0.508 mm to 1.524 mm) thick polymeric material resulting in better shatter protection without creating flying glass fragments which remain adhered to the PVB interlayer, as shown in Fig. 3.22(c). Such laminated glass is widely used as wind shield of vehicles. In the present study, only monolithic annealed or only float glass is considered.

(a) Annealed glass (b) Tempered glass (c) Laminated glass

Figure 3.22. Crack patterns of different glass types under impact.

Apart from damage from projectile impact, glazing used in the exterior cladding of a building may fail from storm borne missile; severe wind pressure in a cyclone; blast shock pressure; and deliberate projectile attack (ballistic or otherwise). Being a highly complex material, its material characterization presents significant challenges. In numerical simulations, the main properties of interest for glass are density, thickness, elastic and shear moduli, Poisson's ratio, strength data (namely, tensile strength), fracture toughness, strain-rate sensitivity, and thermal sensitivity. According to Limbach et al. [75], strain-rate effects do not affect mechanical properties of glass under normal ambient temperature conditions. However, based on his extensive experimental work, Nie et al. [76] emphasized that glass appears to be strain-rate sensitive at high rates and higher tensile strengths. Holmquist et al. [77] proposed the following strain-rate formula for glass in the form commonly used for other materials.

$$DIF_g = \frac{\sigma}{\sigma_o} = 1.0 + C_g \ln \dot{\varepsilon} \tag{3.32}$$

Here, σ_o is the strength of glass at $\dot{\varepsilon}_o = 1$. Neither did the authors specify the unknown constant C_g nor allow for strain-rate effect in their follow up simulations of glass under impact load. In view of lack of data and prevailing uncertainty, strain-rate effect in glass is not considered

in this study. The mechanical properties of glass used in this study are based on laboratory tests undertaken by the author on representative test specimen of the glass used in the test models. Details are given in Appendix A. The properties of glass used in numerical simulation are shown in Appendix A (Table A1).

3.2.4 High Density Polyethylene Sheet

High density polyethylene is a highly ductile material. If the window glazing of an existing building is float glass, the first line of defense against breakage from projectile impact and blast effects, is to apply bonded safety films. High-density polyethylene sheet of appropriate thickness and adequate bonding capacity can serve as such a film. This type of sheet is supposed to be extremely strong against impact and abrasion. According to manufacturers, such a film can provide protection against, flying broken glass caused by accident, violent weather (glass breakage from high wind pressures and flying debris), attempted break-ins by vandals and thieves, explosion blasts, and projectile impacts.

For use in numerical simulation, the mechanical properties of interest of the HDP sheet material are shown Appendix A (Table A2). These properties are based on laboratory tests undertaken by the author on representative test specimen of the Polyethylene used in the research. The details of the test are given in Appendix A.

Strain-Rate Effect in HDP

Apart from using SHPB test to find normally measured strain-rate ($\leq 10^{-4}$ per sec) effects, Al-Maliky and Parry (1994) measured the more difficult very high strain-rate effects of high-density polyethylene using a novel technique known as exploding wire technique (EWT). Based on these experiment data from [78] (shown as blue markers) and the associated pair of trend lines obtained by the author are shown in Fig. 3.23. DIF_t equations for the two segments of the trend line were

$$DIF_t = \begin{cases} 2.353\log(\dot{\varepsilon}) - 6.996, & \dot{\varepsilon} \leq 13.75 \\ 0.1094\dot{\varepsilon} + 1.2394, & \dot{\varepsilon} > 13.75 \end{cases} \tag{3.33}$$

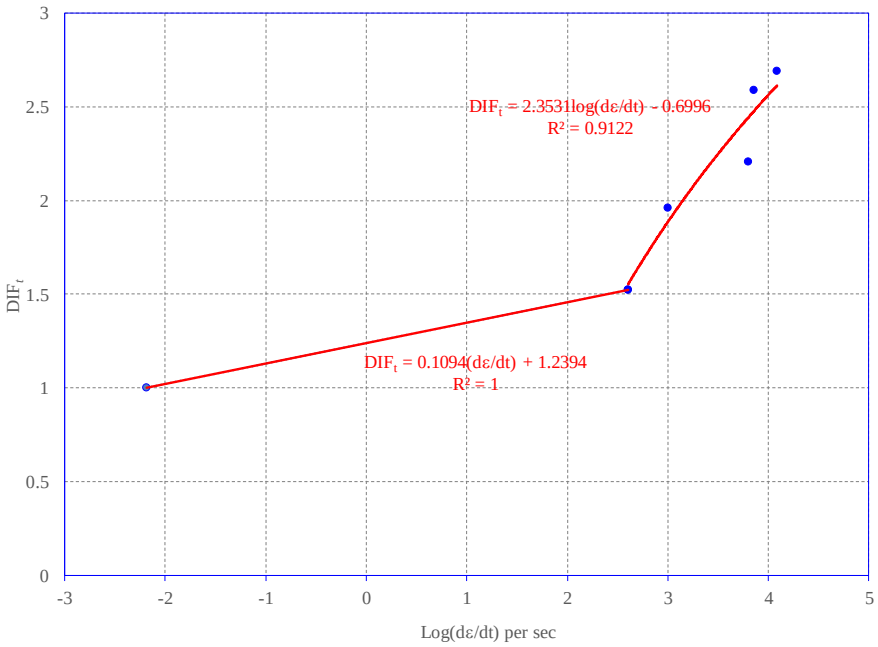

Figure 3.23. Strain rate effect for HDPE.

3.3 Constitutive Relationships

Constitutive relationships of materials used in the structure at different levels of loading are important elements of the response prediction process. Constitutive relationships for the four materials of interest are considered. In Section 3.3.1, the nonlinear constitutive relationships for concrete and selected phenomenological mathematical models reflecting continuum scale behavior are detailed. In Sections 3.3.2 to 3.3.4, the applicable constitutive relationships and the mathematical models used in this study are described.

3.3.1 Concrete

As a quasi-brittle material, concrete is prone to cracking initiated by the appearance of micro-cracks which coalesce into larger cracks that may lead to structural collapse. Any effort to analytically predict the dynamic response of a concrete plate due to impact requires identification of the appropriate failure model for concrete. This can be addressed either at microscopic level or, at macroscopic (i.e., continuum) scale. In the present study, the continuum approach based on smeared crack concept is adopted. To be able to solve the governing equations of motion, it is necessary to define appropriate phenomenological model by accurately incorporating uniaxial, biaxial, and triaxial behaviors of concrete in tension, compression, and combinations thereof. In Section 3.1, material models of concrete based on laboratory test data was presented.

The earliest models for characterizing the nonlinear mechanical behavior of materials, like Tresca, von Mises, Mohr-Coulomb, Drucker-Prager, etc., are based on plasticity theory accounting for linear isotropic strain hardening behavior combined with brittle failure criterion in tension, Chen [34]. These models were improved upon over the years by allowing for nonlinear plasticity and damage. The essential elements of such models are yield function, flow rule, damage measure, dilatancy (to account for the influence of confinement pressure on plastic strain components), and strain-rate effect.

The simplest definition of yield surface is based on the relationship between hydrostatic pressure, $p = I_1/3$, and square root of second variant of deviatoric stress tensor, $\sqrt{J_2}$, in terms of experimentally determined material constants. For instance, in the case of Drucker-Prager model the equation is

$$\alpha I_1 + \sqrt{J_2} - \beta = 0 \tag{3.34}$$

where $I_1 = \sigma_1 + \sigma_2 + \sigma_3$, the first invariant of stress tensor in terms of principal stresses and

$$J_2 = \frac{1}{6}\left[(\sigma_1 - \sigma_2)^2 + (\sigma_2 - \sigma_3)^2 + (\sigma_3 - \sigma_1)^2\right]$$

The material constants α, β can be defined in terms of uniaxial yield strength in tension, f_{yt}, and in compression, f_{yc}. The resulting form of Eq. (3.34) will then be as shown in Eq. (3.35).

$$\frac{\left(f_{yc} - f_{yt}\right)}{2} I_1 + \frac{\left(f_{yc} + f_{yt}\right)}{2} \sqrt{3J_2} - f_{yc} \bullet f_{yt} = 0 \tag{3.35}$$

This equation can also be expressed in terms of the new set of invariants (ξ,ρ,θ) known as Haigh-Westergaard (Lode) coordinates, with $\xi = I_1/\sqrt{3}$, $\rho = \sqrt{2J_2}$ and $3\theta = \cos^{-1}(3\sqrt{3}J_3/2J_2^{3/2})$. Here, ξ represents the axis of the conical yield surface, ρ the radius of the circle, and θ the angular position of ρ in the π-plane measured counter-clockwise with respect to the direction of deviatoric stress s_1 $(= \sigma_1 - I_1/3)$. The third invariant of deviatoric stress tensor: $J_3 = s_1 s_2 s_3$, $s_i = \sigma_i - I_1/3,\ i = 1,2,3.$ In terms of the new invariants, Eq. (3.35) takes the following form,

$$\left(f_{yc}-f_{yt}\right)\xi+\frac{\left(f_{yc}+f_{yt}\right)}{\sqrt{2}}\rho-\frac{2}{\sqrt{3}}f_{yc}\bullet f_{yt}=0 \tag{3.36}$$

This is essentially a two-parameter equation for the yield surface. During plastic flow, the stress point stays on this yield surface. The Drucker-Prager yield surface in the $(\sigma_1,\sigma_2,\sigma_3)$-space is shown in Fig. 3.24.

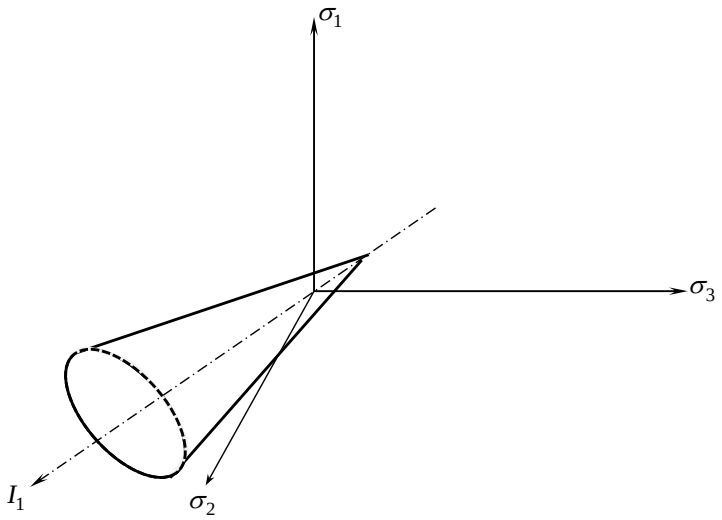

Figure 3.24. Drucker–Prager yield surface.

This model was further improved upon to differentiate between the tension and compression segments of the meridian of the yield surface. In the process, apart from compressive and tensile strengths, biaxial compressive strength, $f_{bc}^{'}$, also came into play. Due to continued inconsistencies of the model with respect to test data, further modifications were made resulting in changes in its shape in the π - plane (exhibiting three-way symmetry) with the variation of the magnitude of the hydrostatic confining pressure, p. The value of ρ for tension meridian (ρ_t) was smaller than that for the compression meridian (ρ_c), as evident from Fig. 3.25.

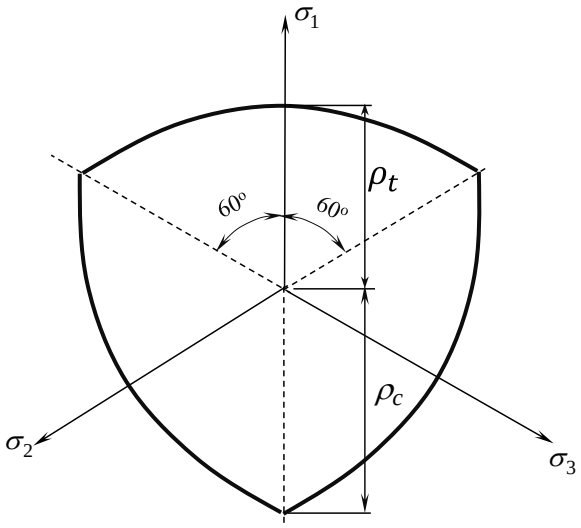

Figure 3.25. Typical π-plane profile of Drucker–Prager yield surface allowing for unequal tensile and compressive strengths of concrete ($I_1/f_c' = -4$, $f_c' = 41.93$ MPa).

The basic elements of plasticity theory are yield criterion and flow rule. For brittle material like concrete, the effects of rules for hardening and softening allowing for progressive damage need also to be addressed. The earlier models were inadequate in this respect. In Section 3.1.1, the usefulness of the concept of damage parameter was discussed in the context of uniaxial loading. The next generation of models with three to five parameters attempted further refinement of the model by including pressure sensitivity, path sensitivity, non-associated flow rule and strain-hardening leading to Modified Drucker-Prager failure criterion (or, Bresler-Pister criterion) [91], Hsieh-Ting-Chen failure criterion [92], William-Warnke failure criterion [93], Menetrey-William criterion [94], Imran, et al. [95], Grassl et al. [96], etc.

To ensure convexity of the yield surface at all points, William et al. [93] fitted the existing data on ρ_t and ρ_c in the deviatoric plane with a curve of elliptic shape in each 120° sector and put forward the following highly complex ρ vs θ formula.

$$\frac{\rho(I_1,\theta)}{\rho_c} = \frac{2(1-e^2)\cos\theta + (2e-1)\sqrt{4(1-e^2)\cos^2\theta + 5e^2 - 4e}}{4(1-e^2)\cos^2\theta + (2e-1)^2} \quad \text{with } e = \frac{\rho_t}{\rho_c} \tag{3.37}$$

Based on this formula, the shapes of the yield surface in the π-plane for different values for different values of $I_1 / f_c^{'}$ are shown in Fig. 3.26.

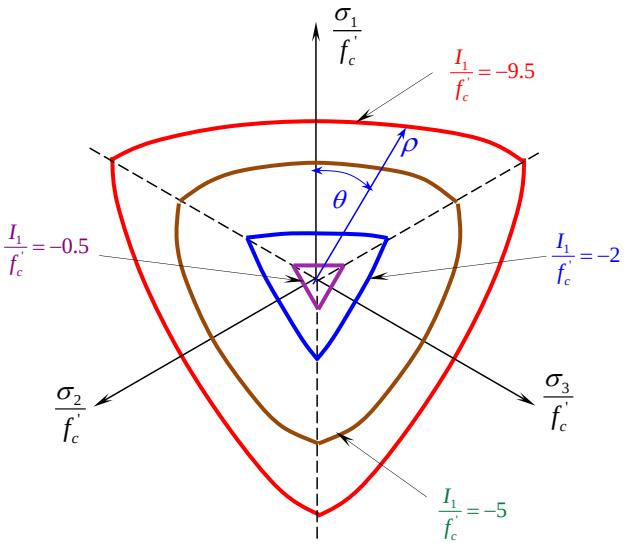

Figure 3.26. π-plane view of yield surface based on Eq. 3.37.

In addition to the yield surface, flow rules are necessary to monitor the plastic strain during hardening and softening processes and, also, the associated damage events through appropriate plastic strain vs stress relations in the incremental form. For instance, Eq. (3.37) can be rewritten as a yield function (or the plastic potential function in associate flow rule) after allowing for hardening and softening behavior. According to Kang [97], it can be expressed as below.

$$F(\xi,\rho,\theta) = F_p(\xi,\rho,\theta,DIF(\dot{\varepsilon}^*)) + F_h(\xi,\rho,k(q_h)) + F_s(\xi,\rho,c(q_s)) = \kappa \tag{3.38}$$

Here, the parameter κ is akin to a cohesive term, which becomes zero when the state of stress at a point $(\sigma_1,\sigma_2,\sigma_3)$ satisfies Eq. (3.37), meaning vanishing of this term. In this equation, the first term considers plasticity in the presence of strain-rate effects due to dynamic loading. The second term allows for the effect of strain-hardening on the yield surface and the third term allows for the effect of strain-softening due to the development of microscopic cracks. During plastic flow, $dF = d\boldsymbol{\sigma} : \partial F/\partial \boldsymbol{\sigma} = 0$ and during elastic unloading, $d\boldsymbol{\sigma} : \partial F/\partial \boldsymbol{\sigma} < 0$. In the case work-hardening if the applied load is greater than the yield load, a new expanded yield surface will develop for which $F = F_p + F_h$. According to associated flow rule, the expansion at a point on the yield surface occurs concentrically in the normal direction, so that $d\boldsymbol{\sigma} : \partial F/\partial \boldsymbol{\sigma} \geq 0$. As per Drucker's stability criterion [98], the infinitesimal plastic strain is $d\boldsymbol{\varepsilon}^p = d\lambda \cdot \partial F/\partial \boldsymbol{\sigma}$, where $d\lambda$

is a positive scalar proportionality factor. Hence, the expanded yield surface will have the same shape as the original and is dependent upon the loading history. In view of the eccentricity in deviatoric shape of the yield surface for concrete, the use of non-associated flow theory by replacing *F* in the flow equation with the equation of plastic flow potential, say, g, makes more sense. In this case, apart from the change in size, the deviatoric planar view of the failure surface can shift laterally. Thus, for non-associated flow rule: $d\boldsymbol{\varepsilon}^p = d\lambda \cdot \partial g / \partial \boldsymbol{\sigma}$. The gradient $\partial g / \partial \boldsymbol{\sigma}$ controls inelastic dilatancy. In the case of inelastic deformations, the total deformation will have elastic and plastic components, so that $d\boldsymbol{\varepsilon} = d\boldsymbol{\varepsilon}^e + d\boldsymbol{\varepsilon}^p$. The elastic component can be expressed as

$$d\boldsymbol{\varepsilon}^e = \left[\frac{dI_1}{9K} + \frac{1}{2G}\left(d\boldsymbol{\sigma} - \frac{dI_1}{3} \right) \right] \tag{3.39}$$

where, $K(I_1)$ and $G(J_2)$ are path-independent bulk and shear elastic moduli. To determine the hardening parameter $d\lambda > 0$, the consistency condition [34] can be used.

During degradation due to plastic damage, the cohesive terms will get modified. To allow for this, as was discussed in Section 3.1, the scalar stiffness degradation parameter, $0 \le d \le 1$, to represent associated stiffness reduction is introduced. Moreover, significantly lower tensile strength of concrete than its compressive strength requires consideration of different damage parameters for softening signifying damage growth and coalescence of micro cracks in tension, d_t, and in compression, d_c. Both these effects may be treated as isotropic. The composite damage parameter caused by both events will be $d = 1-(1-d_c)(1-d_t)$ and the constitutive relationship after damage will take the following double dot product form.

$$\sigma_{ij} = (1-d) C^e_{ijkl} : \left(\varepsilon_{kl} - \varepsilon^p_{kl} \right) \tag{3.40}$$

Here, σ_{ij} is the Cauchy stress tensor and C^e_{ijkl} is the original elasticity tensor, and $\varepsilon^e_{kl}, \varepsilon^p_{kl}$ represent elastic and plastic components of Green-strain tensor. C^e_{ijkl} can be expressed in terms of bulk and shear moduli as shown below:

$$C^e_{ijkl} = \left(K - \frac{2}{3}G \right)\delta_{ij}\delta_{kl} + G(\delta_{ik}\delta_{jl} + \delta_{il}\delta_{jk}) \tag{3.41}$$

so that, $\sigma_{ij} = (1-d)\left[K\varepsilon^e_{kk}\delta_{ij} + 2G\left(\varepsilon^e_{ij} - \frac{1}{3}\varepsilon^e_{kk}\delta_{ij} \right) \right]$, $\varepsilon^e_{ij} = \varepsilon_{ij} - \varepsilon^p_{ij}$.

According to the damage criterion of Mazars [24], the equivalent strain of quasi-brittle material

$$\tilde{\varepsilon}^e = \sqrt{\Sigma_i \left(\left\langle \varepsilon^e_i \right\rangle_+ \right)^2}$$

where ε_i =principal strain with $\left\langle \varepsilon_i \right\rangle_+ = \varepsilon_i$ if $\varepsilon_i \geq 0$ and $\left\langle \varepsilon_i \right\rangle_+ = 0$ if $\varepsilon_i < 0$. The damage threshold is then defined by

$$f(d) = \tilde{\varepsilon}^e - \kappa(d)$$

where $\kappa(0) = \varepsilon_{do}$, the initial damage threshold.

Based on the basic considerations discussed so far, attention is focused on two widely used specific models of concrete, CDP and HJC, used in this research.

Concrete Damage Plasticity (CDP) Model

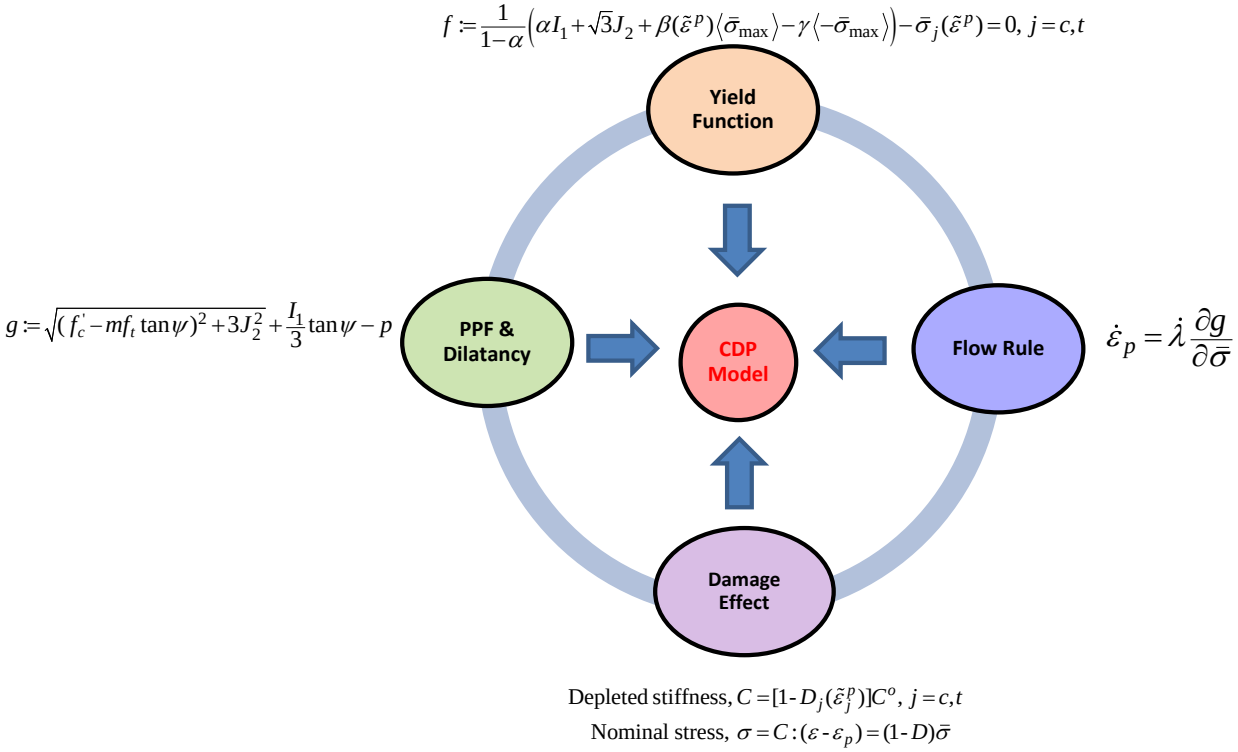

Figure 3.27. Concrete damage plasticity model.

As implemented in Abaqus, CDP model is the culmination of the models proposed by Lubliner et al. [80] followed by modifications of Lee et al. [81]. This model captures the irreversible damage process in quasi-brittle material like concrete under relatively low confining pressures. In compression, it allows for hardening followed by softening. In tension, the hardening part is ignored. It distinguishes between degradation of elastic stiffnesses in compression and tension. Contrary to reported claims, during this study, the Abaqus implementation of the model failed to properly account for strain-rate effects. So, this model is suited for problems involving low strain-rates. The essential elements of the model are summarized in Fig. 3.27. As shown in the figure, the main components of the model can be identified as: (i) yield function; (ii) flow rule; (iii) plastic potential function including dilatancy; and (iv) damage effect.

(i) Yield function (YF)

If the point in the three-dimensional stress space lies inside the yield surface, the material is elastic. If, however, the stress at a point lies on the yield surface, at that point, concrete is said to have reached the plastic state.

$$f := \frac{1}{1-\alpha}\left(\alpha I_1 + \sqrt{3J_2} + \beta(\tilde{\varepsilon}^p)\left\langle \hat{\bar{\sigma}}_{\max} \right\rangle - \gamma\left\langle -\hat{\bar{\sigma}}_{\max} \right\rangle\right) - \bar{\sigma}_j(\tilde{\varepsilon}_j^p) = 0,\ j = c,t \tag{3.42a}$$

Here, $\alpha = \dfrac{(f_{bc}' - f_c')}{(2f_{bc}' - f_c')};\ \gamma = \dfrac{3(1-e)}{(2e+3)};\ \beta(\tilde{\varepsilon}^p) = \dfrac{\bar{\sigma}_c(\tilde{\varepsilon}_c^{pl})}{\bar{\sigma}_t(\tilde{\varepsilon}_t^{pl})}(1-\alpha) - (1+\alpha)$

$e = \rho_t/\rho_c$ (Typical value = 2/3)

with hardening variables (or, equivalent plastic strain) defined as

$$\tilde{\varepsilon}_c^p, \tilde{\varepsilon}_t^p = \int_o^t \dot{\tilde{\varepsilon}}_t^p dt, \int_o^t \dot{\tilde{\varepsilon}}_c^p dt;\ \dot{\tilde{\varepsilon}}_t^p = r(\hat{\bar{\sigma}})\dot{\hat{\varepsilon}}_{\max}^p;\ \dot{\tilde{\varepsilon}}_c^p = -(1 - r(\hat{\bar{\sigma}}))\dot{\tilde{\varepsilon}}_{\min}^p$$

$\tilde{\varepsilon}_{\max}^p, \tilde{\varepsilon}_{\min}^p$ – maximum and minimum characteristic (or, eigen) of plastic strain tensor, so that

$$\dot{\tilde{\varepsilon}}^p = \begin{Bmatrix} \dot{\tilde{\varepsilon}}_t^p \\ \dot{\tilde{\varepsilon}}_c^p \end{Bmatrix} = \begin{bmatrix} r(\tilde{\bar{\sigma}}) & 0 & 0 \\ 0 & 0 & -(1-r(\tilde{\bar{\sigma}})) \end{bmatrix} \left\{ \dot{\tilde{\varepsilon}}_1^p, \dot{\tilde{\varepsilon}}_2^p, \dot{\tilde{\varepsilon}}_3^p \right\}; \; r(\tilde{\bar{\sigma}}) = \frac{\sum_{i=1}^{3} \langle \tilde{\bar{\sigma}}_i \rangle}{\sum_{i=1}^{3} |\tilde{\bar{\sigma}}_i|}, \; 0 \le r(\tilde{\bar{\sigma}}) \le 1$$

when, $\bar{\sigma}_c(\tilde{\varepsilon}_c^p), \bar{\sigma}_t(\tilde{\varepsilon}_t^p) =$ effective compressive and tensile cohesion stresses

$\langle \bar{\sigma}_{\max} \rangle = 0$ if $\bar{\sigma}$ is compressive and 1 if $\bar{\sigma}$ is tensile (cracking)

$\langle -\bar{\sigma}_{\max} \rangle = 1$ if $\bar{\sigma}$ is compressive and 0 if $\bar{\sigma}$ is tensile (crushing)

$r(\tilde{\bar{\sigma}}) =$ stress weight factor is =0 if all principal stresses are negative and 1 if all are positive.

(ii) Flow rule

The non-associated flow rule for plastic strain rate calculation in quasi-brittle materials like concrete is proportional to the rate of change of the scalar plastic potential function, g, with respect to stress.

$$\dot{\varepsilon}_p = \dot{\lambda} \frac{\partial g}{\partial \bar{\sigma}} \tag{3.42b}$$

Here, $\dot{\lambda}$ represents the rate of change of hardening parameter. According to Kuhn–Tucker conditions, $\dot{\lambda} f = 0; \; \dot{\lambda} \ge 0; \; f \le 0.$

(iii) Plastic potential function (PPF)

$$g := \sqrt{(m f_t^{'} \bullet \tan\psi)^2 + 3J_2^2} + \frac{I_1}{3}\tan\psi - p \tag{3.42c}$$

where m = eccentricity of PPF

ψ = dilatancy angle

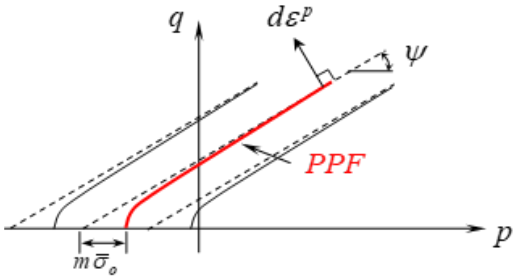

Figure 3.28. Definition of m and ψ.

As shown in Fig. 3.28, the dilatancy angle, ψ, and eccentricity parameter, m, is measured in the $p-q$ plane based on hyperbolic Drucker–Prager flow rule. At high confining pressures, m defines the rate at which the function approaches the asymptotic value.

(iv) Effect of damage

Damage accumulation causes progressive softening of concrete. The resulting elasticity matrix is expressed as

$$\boldsymbol{C} = (1 - d_j)\boldsymbol{C}^o,\ j = c,t \tag{3.42d}$$

where $\boldsymbol{C}^o$ = elasticity matrix of damaged material

$d_t = d_t(\tilde{\varepsilon}_t^p),\ 0 \le d_t \le 1-$ tensile damage factor

$d_c = d_c(\tilde{\varepsilon}_c^p),\ 0 \le d_c \le 1-$ compressive damage factor

So, the expression for nominal stress tensor becomes

$$\boldsymbol{\sigma} = \boldsymbol{C} : (\boldsymbol{\varepsilon} - \boldsymbol{\varepsilon}^p) = (1-d)\bar{\boldsymbol{\sigma}}$$

$$d = d(\bar{\boldsymbol{\sigma}}, \kappa)$$

$$\kappa = \left\{ \tilde{\varepsilon}_t^p, \tilde{\varepsilon}_c^p \right\}$$

$\bar{\boldsymbol{\sigma}}$ = the effective stress vector.

Holmquist–Johnson–Cook (HJC) Model

The HJC model [82] allows for large deformations, high pressures, high strain rates, damage, fragmentation and spalling of concrete under high-speed impact. As shown in Fig. 3.29, the HJC model also has relationships between four major components: (i) yield function; (ii) strain-rate effect; (iii) damage effect; and (iv) equation of state.

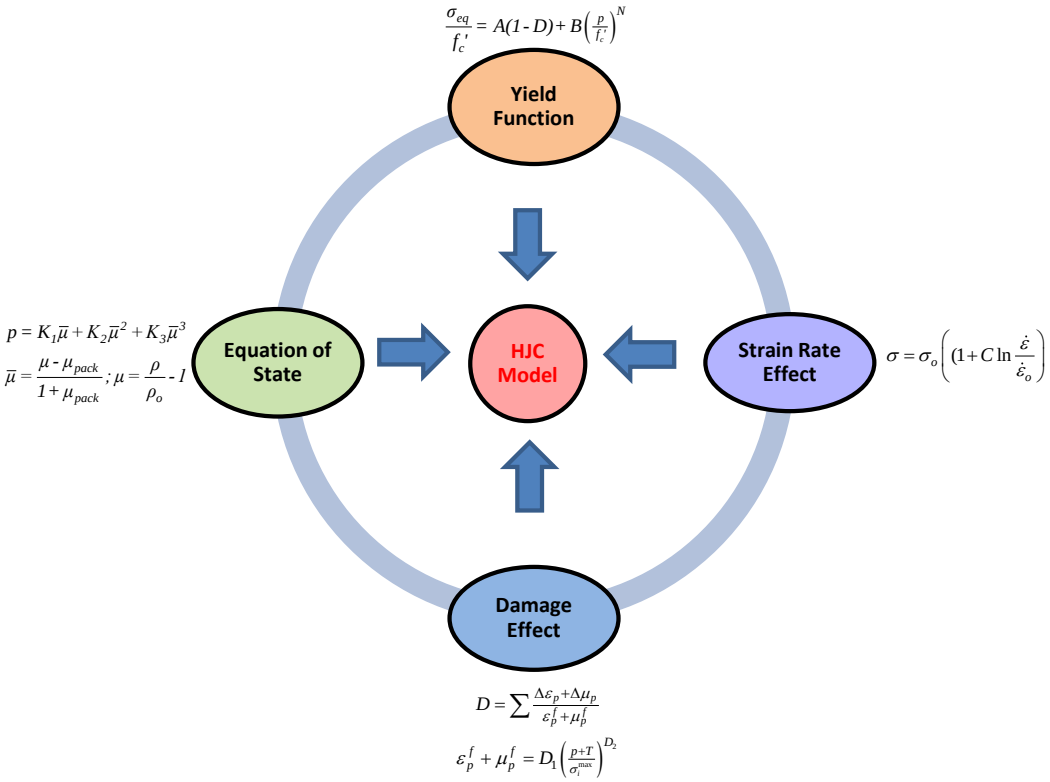

Figure 3.29. HJC model.

(i) Yield function

Here, the yield function is given by Eq. (3.43a). It determines the effects of hydrostatic pressure and damage parameter on material strength. *A*, *B*, *C* and *N* are material parameters determined by fitting the model to test data. This equation follows von Mises yield surface and assumes plastic flow to be isochoric. $0 \le D \le 1$ is scalar damage parameter. One of the two more terms which are not shown here accounts for the strain rate effect and other term allows for the temperature dependence of strength which is not part of the present study. As will be shown, for strain-rate dependence the equation is multiplied by *DIF*.

$$\sigma_{eq}^{*} = \frac{\sigma_{eq}}{f_c'} = \frac{\sqrt{3J_2}}{f_c'} = \left[A(1-D) + B\left(\frac{p}{f_c'}\right)^N\right] DIF \le s_{\max} \tag{3.43a}$$

In this equation, $A =$ cohesive coefficient; $B =$ normalized pressure hardening coefficient; $DIF =$ dynamic increase factor due to strain-rate effect; $N =$ pressure hardening exponent; $D =$

accumulated damage; $\frac{p}{f_c'} = p^* = \text{normalized pressure} \geq 0$; $\frac{\sigma_{eq}}{f_c'} = \sigma_{eq}^* = \text{normalized equivalent}$ stress; and $s_{\max} = \text{normalized deviatoric strength}$. The effect of D on σ_{eq}^* vs p^* plot is shown in Fig. 3.30.

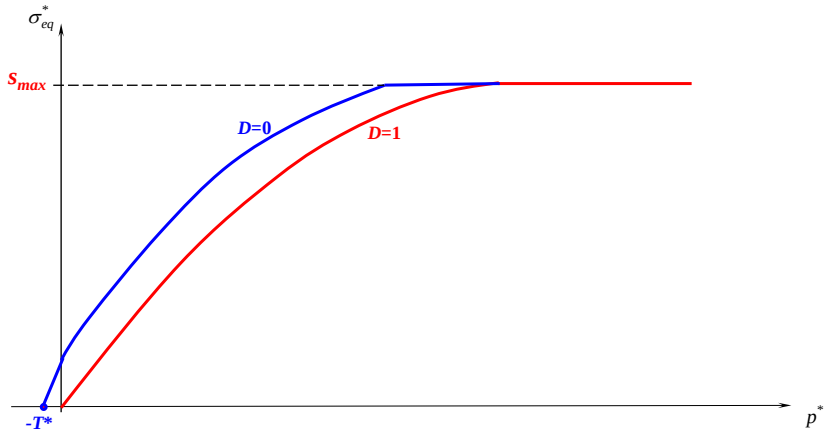

Figure 3.30. Plots of Eq. (3.43a) for $D = 0$ and 1.

The intercept of the D=0 line with p^* axis represents the normalized tensile strength of concrete ($T^* = \frac{T}{f_c'}$). For $p^* \leq 0$, the yield function is assumed to be linear defined by the following equation, signifying that the damage behavior of concrete is damage dependent.

$$\sigma_{eq}^* = A(1-D)\left(1+\frac{p}{T}\right) \tag{3.43b}$$

(ii) Strain-rate effect

In the original HJC model [82], the expression for DIF is given as

$$DIF = \frac{\sigma}{\sigma_o} = \left[1 + C\ln\left(\frac{\dot{\varepsilon}}{\dot{\varepsilon}_o}\right)\right] \tag{3.43c}$$

where, $C = 0.007$ is a coefficient based on experimental data, and $\dot{\varepsilon}_o$ =1.0/s is the reference strain

rate. It was found during this study that this value for C grossly underestimates the value of DIF.

Based on the actual loading rate of 35 psi/sec (or, 0.241 MPa/sec.) used during laboratory strength tests of concrete, the actual reference strain-rate was found to be close to 10^{-5}/s and a higher value for C = 0.033 seems to be more appropriate. Not surprisingly, the DIF vs $\dot{\varepsilon}$ plot based on C = 0.033 follows the other predictions more closely for $\dot{\varepsilon} < 100.0 s^{-1}$. In a 2018 paper, Johnson et al. [83] stated the need to improve the formula for higher strain rates by introducing additional terms. Shortcoming of the original HJC formula was also pointed out by Liu et al. [85] and need for modification was emphasized. Alternatively, the proposed more accurate formulas for DIF, applicable to full range of $\dot{\varepsilon}_o$ values, given by Eq. (3.25), or Eq. (3.28) can be used.

(iii) Damage effect

In Eq. (3.43a), the damage parameter is associated with the cohesive strength term which is directly related to shear strength. Two sources of strain are identified as the cause of damage, namely, plastic strain (ε_p) due to deformation and fracture, and plastic volumetric strain (μ_p) due to crushing and void collapse under hydrostatic pressure. In terms of incremental values of these strains normalized with respect to the failure values (ε_p^f and μ_p^f), the damage parameter is expressed as

$$D = \sum \frac{\Delta\varepsilon_p + \Delta\mu_p}{\varepsilon_p^f + \mu_p^f} \tag{3.43d}$$

The effective plastic strain to fracture under constant pressure is larger of the minimum plastic strain value ($\varepsilon_{f\min}$) which will cause the material to fracture. Its value is given by Eq. (3.43e). In the absence of test data, the default value of $\varepsilon_{f\min}$ is taken as 0.01. Damage constants D_1 can be based on unconfined compressive strength data. The damage constant D_2 is set equal to 1.0.

$$\varepsilon_p^f + \mu_p^f = D_1(p^* + T^*)^{D_2} \geq \varepsilon_{f\min} \tag{3.43e}$$

(iv) Equation of state

In Section 3.1.2 the hydrostatic pressure vs. volumetric strain relationship was defined with the help of Fig. 3.10. The equations for the three stages are summarized here.

- In the elastic stage, $\mu_{crush} = p_{crush}/K$, where $K = E_c / 3(1-2\nu_c)$ and $p_{crush} = f_c^{'}/3$.
- In the compaction stage: $p = p_{crush} + K_{lock}(\mu - \mu_{crush})$ with

  $K_{lock} = (p - p_{crush})/(\mu_{lock} - \mu_{crush})$
- In the packing stage: $p = f(\bar{\mu}) = K_1\bar{\mu} + K_2\bar{\mu}^2 + K_3\bar{\mu}^3,\ \bar{\mu} = (\mu - \mu_{lock})/(1+\mu_{lock})$

3.3.2 Role of Stress Invariants

In the three-dimensional principal stress space $(\sigma_1, \sigma_2, \sigma_3)$, every stress can be defined in terms of three stress invariants. But in the material models considered so far only two invariants I_1 and J_2, scaled to p and σ_{eq}, respectively were used. It is well known that in the Drucker-Prager model, the yield surface comprises of the spatial diagonal line $(\sigma_1=\sigma_2=\sigma_3)$ or the hydrostatic stress line which is equally inclined to the principal stress axes. The distance of the surface from a point on the surface defines the corresponding deviatoric stress. If one considers the variation of deviatoric stress around a point on the hydrostatic stress line, as defined by Eq. (3.37) and shown in Fig. 3.29, another coordinate comes into play which happens to be the Lode angle θ which was defined by

$$\theta = \frac{1}{3}\cos^{-1}\left[\frac{3\sqrt{3}J_3}{2J_2^{3/2}}\right]$$

In this definition, in addition to J_2, the Lode angle is a function of another stress invariant J_3 which is the third deviatoric stress invariant. This establishes the need for using the third stress invariant if the yield surface is not axisymmetric with respect to the hydrostatic stress line. Accordingly, several models like RHT [88], JHB [89], and AFC [90] models have been put forward. For this purpose, the application of Eq. (3.27) for deviatoric surface profile is popular. This function can be used as a multiplier to the yield function.

3.3.3 Calibration of Model Parameters for Concrete

The quality of predictions based on a material model depends on the accuracy of associated material parameters. The parameters associated with the two constitutive models for concrete used in this study are as follows.

- CDP Model: Experimental material data are $E_c, \nu, f_c^{'}, f_t^{'}, f_{bc}^{'}$. The optimized material parameters requiring calibration are $\alpha, \gamma, m, \psi, e, \dot{\varepsilon}$.
- HJC Model: Experimental material data are $E_c, \nu, f_c^{'}, T(= f_t), p_{cr}, \mu_{cr}, p_{lock}, \mu_{lock}, K_1, K_2$ and K_3. The material parameters requiring calibration are $A, B, D_1, D_2,$ and $s_{\max}$.

Based on the available experimental data, calibration can be undertaken painstakingly by trial and error. Alternatively, a more efficient approach is to use Simulia's optimization software Isight [86] which can be accessed from Abaqus. For quick turnaround, the gradient-free optimization algorithm based on heuristics like Neadler and Mead downhill simplex can be used, provided suitable starting points are defined. For this purpose, the test values of Hanchak et al. [87] for normal strength concrete with f_c'=48 MPa was used. Experimentally, the strength parameters can be obtained by testing cylindrical specimen without and with confining pressures. Such information can be used to determine the parameter values.

3.3.4 Smooth Particle Hydrodynamics Model for Concrete

The Lagrangian formulation discussed in Chapter 2 has been found to be most convenient for modeling the impact problem. However, its numerical implementation in the context of an explicit finite element code runs into acute convergence problems due to excessive element distortion in critical regions prone to local damage, say, at the projectile impact region. This situation is often tackled by using the element erosion option which is activated whenever the effective strain measure in an element reaches the limiting value. A more rational alternative is to switch to a meshless scheme based on the concept of smooth particle hydrodynamics or SPH [99 – 102]. In addition, the response tends to reproduce the actual fragmentation process when the projectile perforates the target. The Lagrangian formulation of SPH can be seamlessly coupled with Lagrangian FE and can be triggered adaptively. Some essential elements of this method are discussed in the following.

In this method, material mass is lumped into motion of a collection of spherical particles motions that satisfy Newton's Second Law of Motion. Computationally this method is more efficient than meshed methods when large strains or distortions are involved. In addition to defining the particle locations, a smoothening function approximation to obtain the kernel estimates of a field variable like, say, acceleration, at a particle location using the values at the end of previous time-step for the *i*-th particle as well as those of neighboring particles within a zone of influence of, say, radius h_i is used. Such a kernel (or, smoothening) function can be based on the following smooth Gaussian function to reflect the influence of all the particles within the zone of influence on the field parameters of *i*-th particle [102].

$$W(|x-x'|,h)=\frac{1}{(\pi h^2)^{n/2}}\exp\left(-\frac{|x-x'|^2}{h^2}\right) \text{ so that } \int_{\Omega_i} W(|x-x'|,h)dx'=1 \tag{3.44}$$

where $|x-x'|$ is the position vector (radial distance) of any particle within the zone of influence from the reference particle.

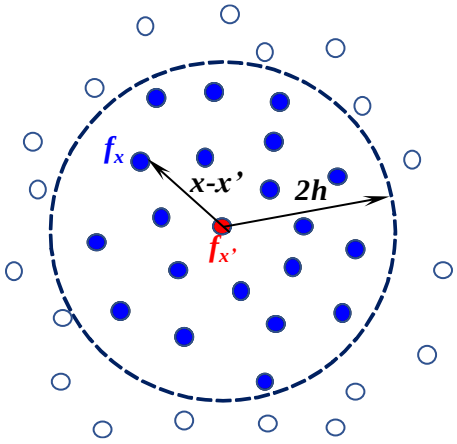

Figure 3.31. The kernel approximation of a function *f*.

The kernel approximation of a function *f* can now be expressed as the following integral, where ***r*** and *r'* are the position vectors of a pair of points, as shown in Fig. 3.31.

$$\langle f(\boldsymbol{x})\rangle = \int f(\boldsymbol{x}')W\left(|\boldsymbol{x}-\boldsymbol{x}'|,h\right)d\boldsymbol{x}' \tag{3.35a}$$

On the other hand, the gradient of a function can be expressed as

$$\langle \nabla \cdot f(\boldsymbol{x})\rangle = \int \nabla . \int_{\partial\Omega} f(\boldsymbol{x}')W(|\boldsymbol{x}-\boldsymbol{x}'|,h)d\boldsymbol{x}' \tag{3.35b}$$

This approximation does not require connectivity of the particles and is capable of handling arbitrary deformations. Based on these integral equation approximations of the function value at a particle location, the equations of conservation of mass, momentum and energy are setup.

3.3.5 Model for Steel Reinforcement

Mechanical characteristics of steel used in this study was considered in Section 3.1.2. Steel rod reinforcement in concrete can either be modeled discretely or, a smeared approach may be used in which the steel reinforcement is assumed to be distributed (smeared) over an entire subdomain with a given volume fraction. In this study, the steel reinforcements are modeled discretely. The reinforcement can be assumed to follow an elastoplastic or elastoplastic strain-hardening material model as well as strain-rate dependent. The models available in Abaqus are adequate for this purpose. In any case, the strain levels in steel are expected to be on the lower side for the speed of the projectiles used in the test.

3.3.6 Model for Glass

Mechanical characteristics of glass used in this study was considered in Section 3.1.3. Depending upon the load level, the following two models are applicable to the plate glass considered in this study.

- Low Load Level: Linear elastic model requiring young's modulus and Poisson's ratio values for glass.
- Higher Load Levels: Brittle fracture model with no plasticity. It may be possible to identify damage initiation, progression, and failure pattern if concrete damage model is adapted to

the characteristics of the material but that means the use of a smeared crack model.

Although Holmquist et al. [103] put forward a constitutive model for glass allowing for large strains, high strain rates and high pressures as improvement upon the JHB Model [104] for brittle materials. Due to its non-availability in Abaqus, no new model is presented for glass under this heading and during numerical simulations attempts so that available models for brittle materials in Abaqus was used.

3.3.7 Model for Polyethylene Film

Based on the tensile stress vs strain curve in Section 3.1.4, this material is treated as elastic-perfectly plastic. Creep effect is not considered in this study, because the impact loading is of very short duration. Models available in Abaqus is adequate to take care of this material.

CHAPTER 4

EXPERIMENTAL WORK

4.1 Introduction

In this chapter all the experimental work undertaken as part this research effort is presented in four major segments. First, details and fabrication of test panels are elucidated. In the next segment, the experimental work related to the determination of strength characteristics of materials, namely, concrete, steel, glass, and polyethylene, used in the fabrication of the test panels is undertaken. Thereafter, impact tests on plain concrete panels without and with glazed opening are covered. Finally, impact testing of the panels hardened with polyethylene film is explained. Necessary details of the tests are presented in Appendix A.

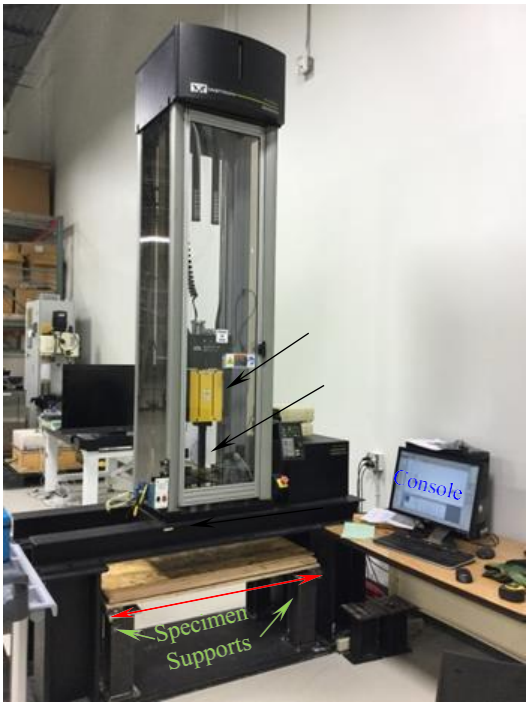

Figure 4.1. Instron/Dynatup 9250 HV.

In Table 2.1, velocities below 820 ft/sec (120m/s) are identified as of low velocity category. High velocity impact tests of structural panels typically involve the use of ballistic projectiles. In his Ph.D. research Heard [47] undertook high velocity impact tests at the modern ERDC facility of USACE in Vicksburg, MS. Such a setup is beyond the reach of the present investigator.

Fortunately, however, the Laboratory for System Integrity and Reliability (LASIR) at Vanderbilt University houses an Instron Drop Weight Impact Tester (Model: Instron/Dynatup 9250 HV) shown in Fig. 4.1 with variable mass, drop height and velocity configurations and was selected for use in this study. This pneumatically assisted drop weight system has a pneumatic rebound brake allowing the maximum impact speed of 14m/s (44ft/sec), squarely putting it in the low velocity range. The upper limit of impact energy is 1603J (1180ft-lb). Free falling height of drop weight is 1.5m (4.92ft) and simulated (spring prestressed) height is 20.4m (67ft). It uses GRC-9301 data acquisition system to acquire load-deflection and energy information captured by sensors.

4.2 Detailing and Fabrication of Test Panels

In Chapter 1, the use of standardized precast reinforced concrete claddings in building construction was discussed. The details of such panels with respect to geometry, materials of construction (namely, concrete and steel reinforcement), anchorage to supporting frame, and nature of window openings were carefully examined. Based on such information, typical single-story candidate panels were identified. Thereafter, keeping in view of available impact test equipment, the required test panels, both in terms of type and number were identified.

4.2.1 Details of Scaled Test Panel

The maximum size of test panel that can be accommodated in the Instron Impact Tester was based on the dimensions of its test bed. The maximum usable length of the test bed, as marked by red arrowed line in Fig. 4.1, was found to be 1219.2 mm (48"). In view of this limitations imposed by the equipment on the size of test specimen, dimensions of typical prototype panels were scaled down by applying the principles of similitude [105, 106]. A test specimen is said to have similitude with the prototype if the two share geometric similarity, kinematic similarity, and dynamic similarity. This can be done by applying the concepts of dimensional homogeneity to ensure that the response formula for the problem will have same dimensions on both sides of the equation. For instance, if the primary parameters of interest in the problem of projectile impact on a concrete plate are identified as mass of rigid projectile (m), diameter of projectile (d), impact velocity (V_o), plate thickness (t), compressive strength of concrete (f'), elastic modulus of

concrete (E_c), etc., then the function for some measurable response quantity (say, x) with the unit of length can be expressed as

$$x = f(m, d, V_o, f_c^{'}, E_c, ...) \tag{4.1}$$

By applying the concept of dimensional homogeneity, the non-dimensional form of Eq. (4.1) will be

$$f\left[\frac{x}{d}, \frac{mV_o^2}{d^3 f_c^{'}}, \frac{E_c}{f_c^{'}}, ...\right] = 0 \tag{4.2}$$

Eq. (4.2) signifies that any dimensionally homogeneous equation can be reduced to an equivalent equation involving a complete set of dimensionless products. One can conclude from this statement that for a truly representative model, the value of each non-dimensional term (also, called as π-number) in Eq. (4.2) for the model and the prototype should be same. This enables identification of the values of scaled model parameters with respect to those of the prototype. Likewise, the response of the prototype can also be predicted in terms of π-numbers comprising of the response parameters measured with the model. For instance, the value of response parameter x for the prototype can be obtained from $x_p = (d_p/d_m)x_m$. Note that here d_p/d_m is the geometric scale factor for the problem. In some situations, it may be very difficult to satisfy equality of all the π-numbers of a problem. In this research, the geometric dimensions of the panel were scaled by a factor of 3 and use was made of a concrete mix to reach the upper strength limits of normal strength concrete, namely M40 concrete with $f_c' \approx 41$ MPs or, 6 ksi, to ensure better resistance against extreme events.

Dimensional details of 1/3rd scale model for two types of panels – two solid (Type-I) and the other with glazed cutout (Type-II) are given in Table 4.1. Also, the gross dimensions of the panels are given in Table 4.1. Note that the overall thickness of all the test panels is 50.8 mm (2"). The reinforcement details of a typical solid panel with volumetric ratio of steel in the test panel close to that of the prototype is shown in Fig. 4.2. The top and bottom steel mesh comprises of 10 mm rods at 22.5 mm centers, giving a steel ratio of 0.216% <1.5% EWFE which is close to

the value of 0.025 used in the prototype. It is worth recalling that according to [107, 108], if the steel ratio is less than 1.5% the steel wire mesh has very little influence on impact resistance.

4.2.2 Construction of Test Panels

The panels were fabricated in the CEE Lab of Vanderbilt University. A total number of six panels were made, two of Type I and four of Type II. Following the practical norms, in Type II panels the cutouts were filled with glazing glass securely placed in a rectangular steel frame made from 1" ×1"×1/8" C shaped channel section. The frame was anchored to concrete with ½" dia.×$1^1/_2$" long studs welded to this steel frame.

Table 4.1. Dimensions of typical test panels.

Panel Type	Panel Overall			Concentric Cutout		Anchor Hole Location
	Length	Width	Thickness	Height	Width	Distance from Corner
I	1143 mm	571.5 mm	50.8 mm	–	–	50.8 mm × 50.8 mm
II	1143 mm	571.5 mm	50.8 mm	584.2 mm	266.7 mm	50.8 mm × 50.8 mm

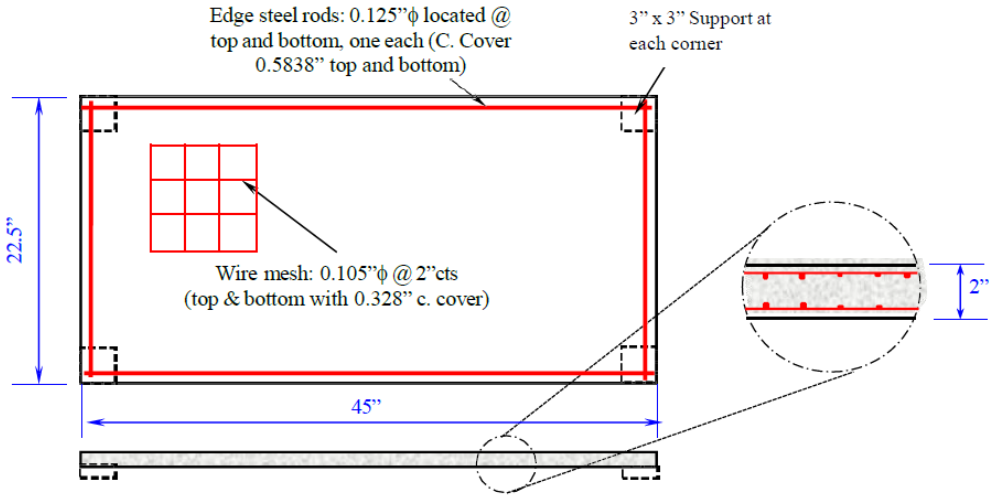

Figure 4.2. Reinforcement details of Panel Type I.

In Fig. 4.3, the pinewood formwork with reinforcement cage in place for both Type I and II panels ready for pouring of concrete is shown. To achieve, at least, M40 grade concrete, ready-mix concrete (Quikrete5000) with maximum aggregate size of 5/16" (8mm) was appropriately reconditioned.

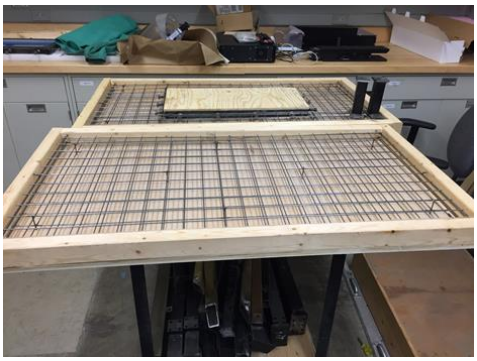

Figure 4.3. Type I and II panels ready for pouring of concrete.

The final mix used in the test panels was arrived at through four trial mixes by varying the water to cement ratio and by adding water reducing superplasticizer (Rheobuild1100) as per ASTM C-494 recommendations. Three standard (4"x8") cylinders were cast for each trial mix and were tested in compression to failure as per ASTM C39/39M [30], after curing for 14 days. The typical variation of compressive strength of concrete with age is shown in Fig. 4.4. According to [109, 110], concrete strength at 28-days can be predicted in terms of 14-day strength based on the following general correlation equation $f'_{c,28} = \kappa(f'_{c,\delta})^{\varsigma}$. The coefficients κ and ς depend on the strength of concrete at *n* days, $f'_{c,n}$ being in MPa. In this formula for *n* = 14 days, coefficient κ = 2.5 and exponent ς = 0.8 [109].

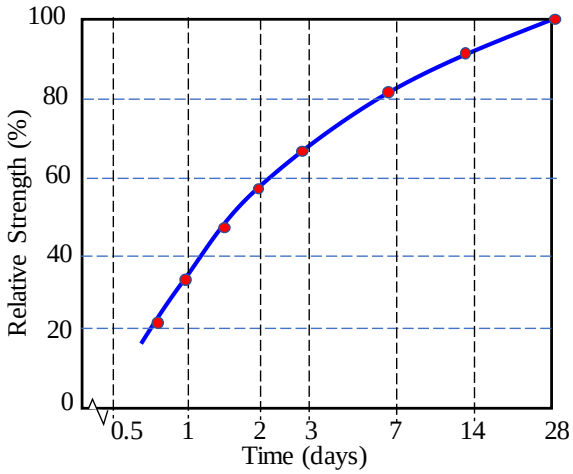

Figure 4.4. Variation of compressive strength with days after casting.

Results of the compression test for four trial mixes are shown Table 4.2. The values in the last two columns of Table 4.2 represent predictions; whereas the rest are values measured by the researcher. The 28-day strength value of 49.03 MPa qualifies the concrete to be classified as high strength concrete as was used in this study.

Table 4.2. Crushing strength values with trial mixes.

Mix	w/c ratio	Load	Stress	14-day Mean Strength		28-day Prediction	
		lb	psi	psi	MPa	psi	MPa
1*i* – 1	0.35	95,980.00	7,637.85	5,986.088	41.273	7,111.327	49.031
1*i* – 2		66,740.00	5,311.00				
1*i* – 3		62,950.00	5,009.41				
1 – 1	0.3	94,960.00	7,556.68	7,412.648	51.108	8,437.521	58.175
1 – 2		99,840.00	7,945.02				
1 – 3		84,650.00	6,736.24				
2 – 1	0.25	93,950.00	7,476.31	7,374.981	50.849	8,403.204	57.938
2 – 2		91,590.00	7,288.51				
2 – 3		92,490.00	7,360.13				
3 – 1	0.2	90,150.00	7,173.92	7,073.913	48.773	8,127.630	56.038
3 – 2		88,920.00	7,076.03				
3 – 3		87,610.00	6,971.79				

The mix designated by '1*i*' in Table 4.2 was used to cast the panels. Within 24 hours of pouring of concrete in the molds, the cast panels were thoroughly cured by covering the molds with wet burlap fabric for 28-days and by spraying with water twice per day during the first week and once per day during the remaining three weeks. Due to the use of plasticizer, the concrete turned out to be self-consolidating and no vibration was necessary. Demolding of the panels was undertaken at the end of 28 days.

4.3 Determination of Mechanical Properties

All materials used in this study were tested as per ASTM standards. The materials of interest were concrete, steel, glass, and polyethylene protective film. Table 4.3 summarizes the material type, test type, shape, size, and type of test specimen, as well as relevant ASTM standards used. The last column refers to relevant section designations in Appendix A where further details are given.

Table 4.3. Material test specimens and reference ASTM spec.

Material	Test Type	Specimen	ASTM Spec.	Details in
Concrete	Unconfined Compressive	4" dia.×8" cylinder	C39/C39M-16b	Secs. A1 & A2
	Split-cylinder Tensile		C496/C496M-17	Section A3
Steel	Tensile	Rod	A370-17a	Section A4
Glass	4-point Flexure	39.4 mm strip	C158-02	Section A5
Polyethylene	Tensile	1" wide strip	D882-12	Section A6

As stated in Table 4.4, the self-adhesive protective polyethylene film was placed on the back face of selected dry panels. In the case of window glass, the film was applied before being placed in the steel window frame. The application of protective film was preceded by the attachment of electrical resistance strain gages at selected locations with appropriate lead wires, as shown in Fig. 4.5. The details of application of strain gages are given in Appendix A (Section A7). In Table 4.4, Panels #1 and #3 are not hardened and hence act as reference panels. Hardening of Panels #5 and #6 are done to allow comparison between the effect of back face only, and both face hardening of glass.

Figure 4.5. Type-I panel after polyethylene film placement.

Table 4.4. Protective film placement scheme.

Panel No.	Panel Type	Hardened	Film Placement		Remarks
			Concrete	Glass	
1	I	No	No	N/A	Reference
2	I	Yes	Yes	N/A	Back Face
3	II	No	No	No	Reference
4	II	No	No	Yes	Back Face
5	II	Yes	Yes	Yes	Back Face
6	II	Yes	Yes	Yes	Both Faces

4.4 Impact Testing of Panels

In Section 4.1, the reasons behind the choice of Instron/Dynatup 9250 HV for impact testing was discussed. Added advantage was the ready assistance from competent LASIR personnel, with experience in using the impact tester. Specifications of the tester are summarized in Appendix A (Table A2). The tests were undertaken keeping in view the following objectives of the experimental study.

a) Determining temporal deflection response of the panels under impact load.
b) Identifying local and global damage types.
c) Identifying local damage patterns for both concrete and glass.
d) Examining strain history at selected locations.
e) Determining the effectiveness of hardening measure in the form attached protective films.
f) Finally validating the prediction of numerical simulations.

4.4.1 Test Setup and Instrumentation

The corner supports used in this study consisted of four vertical steel I-sections topped with 3"×3" welded bearing plate, as shown in Fig. 4.6. C-clamps were used to prevent the slippage of test panels from the supports. In this figure, a Type II panel is resting on the four corner supports, ready for testing.

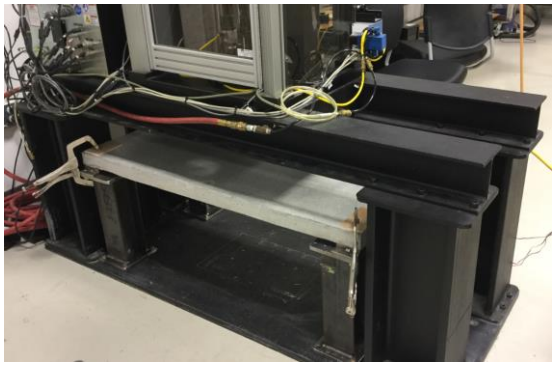

Figure 4.6. Four corner supports.

The procedure for testing all the six panels was same, except that magnitude of impact energy was adjusted according to expected capacity of panel to impact load applied at its center. Details of strain gages is given in Appendix A (Table A1). For high-speed strain data acquisition

National Instruments COMPACTDAQ (cDAQ-9171) was used. Time history of deflection during the impact process was recorded with GRC data acquisition software. In addition, high speed camera was used for visual recording of the motion of the test panel during impact.

4.4.2 Impact Testing

At the start of test, mass (m=16 kg) and the flat-topped projectile size (d= 50.8 mm) were in place, as shown in Fig. 4.1. The specimens were placed on the corner supports. First, the bare and hardened solid panels were considered. These were followed by those with glazed cutout bare and with different degrees of hardening.

Testing of Panel #1

According to Table 4.4, Panel #1 is a Type-I bare solid panel, meaning without being subjected to any hardening measures. This panel served as the reference panel for Type-I series. Table 4.5 shows the drop weight status just before the moment of impact. The corresponding deflection vs. time plot at the point of impact is shown in Fig. 4.7. It may be emphasized that the deflection values correspond to the downward movement of the impactor after first plate contact. The resulting damages can be seen in Fig. 4.8. The impact energy consumed in the test was 12.21 N.mm.

Table 4.5. Impact status just before the moment of impact for Panel #1 and Panel #2.

Panel	**Time**	**Load**	**Energy**	**Velocity**	**Max. Impactor Deflection**
#	s	N	Nm (J)	mm/s	mm
1	0.0244	466.8381	873.39	6,060.9661	55.5232
2	0.02441	996.0205	1766.85	7,617.8978	59.1538

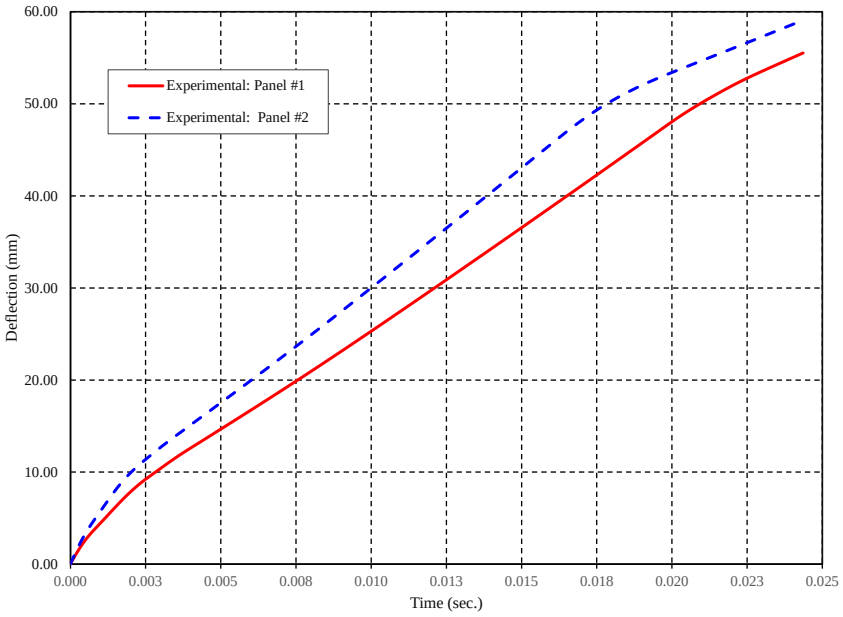

Figure 4.7. Experimental deflection vs. time curves for Panel #1 and Panel #2.

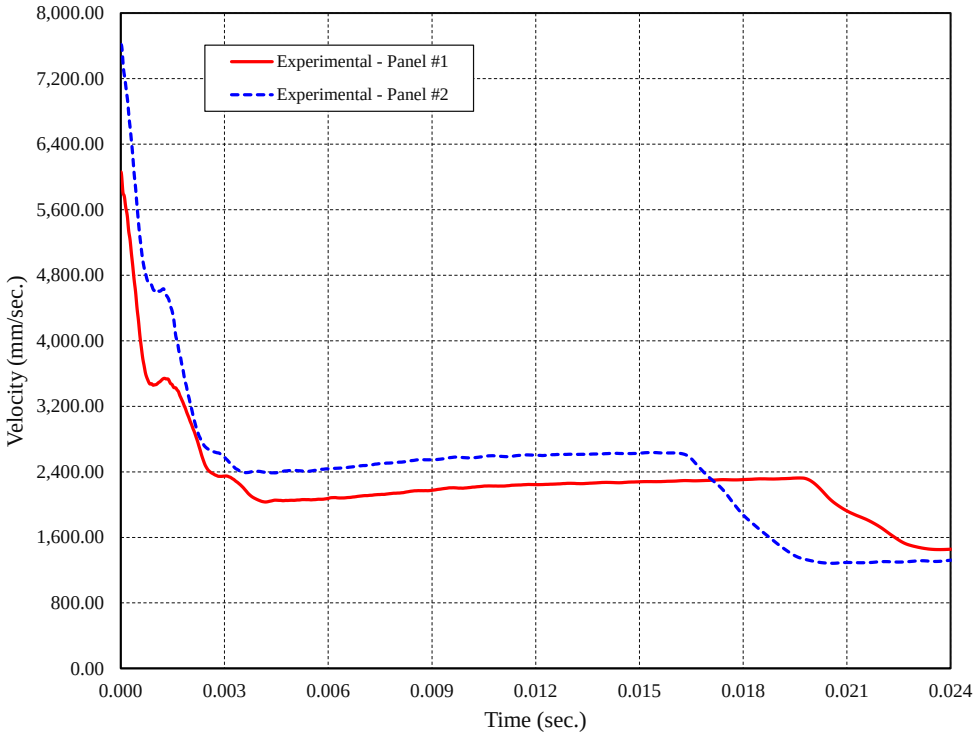

Figure 4.8. Experimental projectile velocity vs. time curves for Panel #1 and Panel #2.

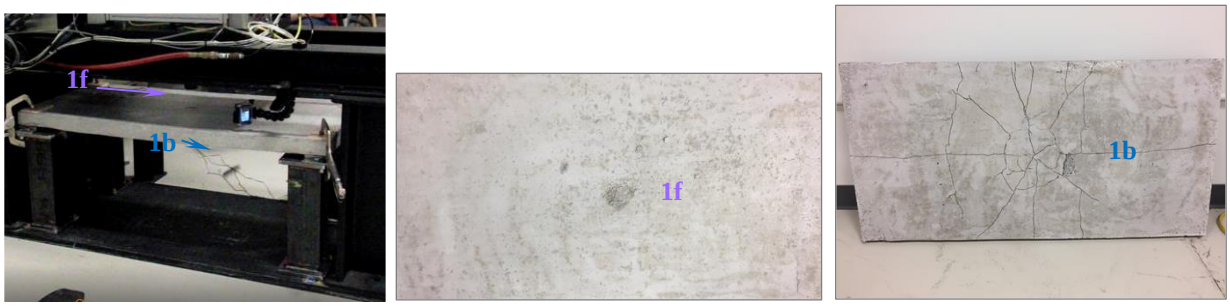

(a) View after test (video frame) (b) Local damage (front face) (c) Local/global damage (back face)

Figure 4.9. Damage during impact (Panel #1).

(1f – Top surface cratering; 1b – dislodged spall material).

In Fig. 4.8, the initial slope of the velocity plot plunges at around 0.0025 sec. due to penetration damage. Before hitting the maximum deflection point, a slight drop in the slope (or, velocity) is noticed, possibly due to further damage caused by spalling from the back face. The maximum deflection recorded at 0.0245 sec was 56 mm. The local and global damage patterns shown in Fig. 4.9 seem to be consistent with those reported in much of the published literature.

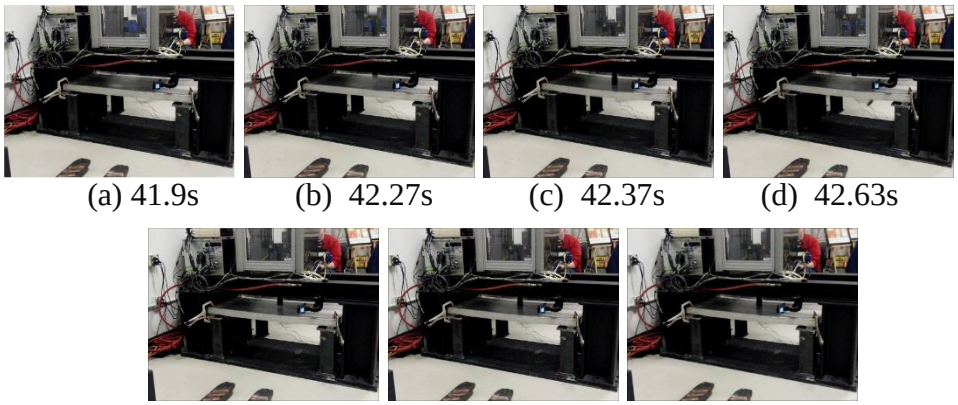

(a) 41.9s (b) 42.27s (c) 42.37s (d) 42.63s

(e) 43.33s (f) 43.42 (g)

Figure 4.10. Critical stages of impact test of Panel #1.

Video frames of the test at critical junctures are shown in Figure 4.10 (a) to (g) and the views successively correspond in (a) plunger release; (b) moments before impact; (c) maximum deflected position after impact; (d) detachment of spalling just after first rebound; (e) plunger approaching for second impact; (f) plunger fails to contact the permanently deformed panel; and

(g) view at the end of test. The times shown are recording time. The time instants shown are the expired time after the camera was turned on. The actual impact process lasted for less than 2 sec.

Testing of Panel #2

As per Table 4.4, Panel #2 is a Type-I solid panel with hardening film bonded to its back face. The nature of response of this panel allowed assessment of the effectiveness of the hardening process in comparison with the bare Panel #1. Table 4.5 gives the status just before the moment of impact. The energy of impact in this case is 27.65 N.mm, which is more than twice the impact energy used for Panel #1, with the hope of ensuring more damage in the panel. Deflection vs. time plot for the point of impact is shown in Fig. 4.7. The resulting damage can be seen in Fig. 4.11.

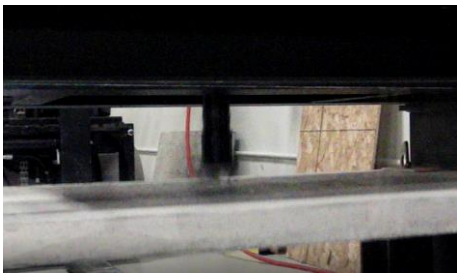

(a) Cratering damage (video frame)

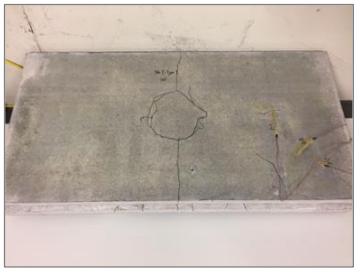

(b) Local/global damage patterns in back face

Figure 4.11. Impact damage in Panel #2.

Video frames of the test at critical junctures are shown in Fig. 4.12 (a) to (j) and the views successively correspond to (a) setup before impact test; (b) approaching plunger before impact; (c) instant of first contact; (d) maximum deflection during first impact; (e) rebounded plunger after first impact; (f) visible crater damage after first rebound; (g) approaching for second impact; (h) more damage after second impact; (i) approaching for possible third impact; and (j) due to permanent panel deformation failed to impinge the panel for third impact. The actual impact process lasted for less than 2.5 sec.

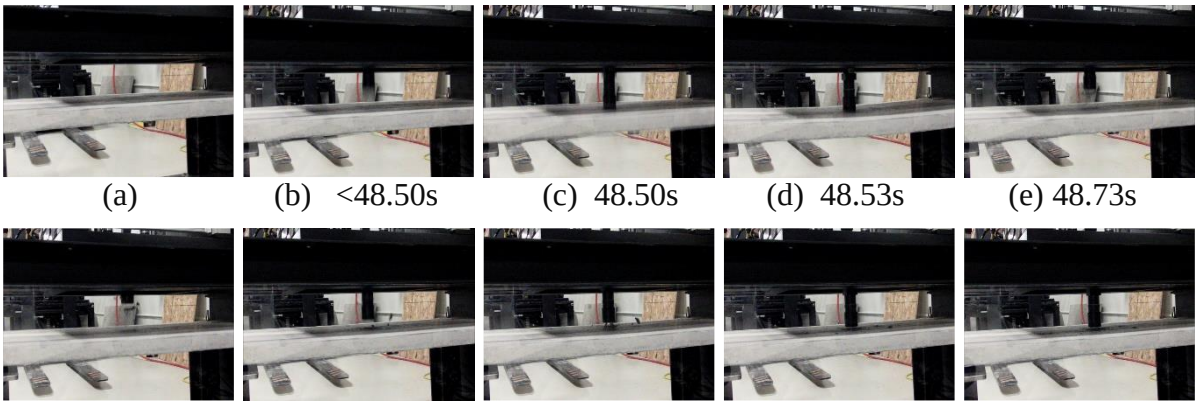

Figure 4.12. Critical stages of impact test of Panel #2.

The velocity vs. deflection curves for the two panels are shown in Fig. 4.8. It is evident from Figs. 4.7, 4.8 and 4.11 that the panel withstood the effect of doubled impact energy quite well showing minimal damage, as elaborated below.

The hardening film enabled the following changes of response in comparison to Panel #1.

a) Maximum deflection at the end of the test, occurring at around same time as for Panel #1, is 59 mm representing an increase of 6.5%. This signifies slight increase in ductility.
b) Unlike Panel #1, the initial part of the response curve is distinctly nonlinear, signifying effect of the attached film.
c) In the time segment 0.0025 sec and 0.0175 sec, the response curve shows nearly constant velocity meaning little loss of energy. At 0.0175 sec. the drop in velocity signifies further energy loss due to damage accumulation.
d) Significantly more energy is absorbed in Panel #2.
e) Unlike Panel #1, there are hardly any cracks showing up in the back face. After a close examination, barely visible hair line cracks were noticed and to highlight their presence black marker was used, as can be seen in Fig. 4.11b. Radial cracking is non-existent. Trace of single cone cracking around the load point was barely visible. Same is true for single flexural crack over the width of the panel.

f) Aspect ratio of the panel is 2. So, larger load transfer is expected to take place along the length explaining the appearance of hair line crack extending over the width of the panel.

g) In Fig. 4.8, as expected, due to higher stiffness of Panel #2, the impactor velocity is consistently higher than that for Panel #1 till 0.18 sec after it crosses down below the curve for Panel #1. This can be attributed to energy loss in the poly-film due to plastic flow.

h) In Fig. 4.8, for both cases the early steep drop in velocities signifies sharing of impact energy with the panel and also due to cratering. The steep drops near the tail ends of the curves also signify energy dissipation, most likely due to global damage.

i) During the test, damage in Panel #1 is caused by single impact. In the case of Panel #2, however, the damage is inflicted twice, first, by the original impact and then by the rebounded plunger.

In the following sections, experimental results for four Type-II panels are presented. The impact loading status for the four panels at the onset of test are shown in Table 4.6. The projectile displacement vs. time plots of the four cases are shown in Fig. 4.15. Also, the corresponding projectile velocity vs time plots are shown in Fig. 4.16.

Table 4.6. Impact machine status at time of impact for Panels #3 to #6 and recorded deflection.

Panel	**Time**	**Load**	**Energy**	**Velocity**	**Max. Impactor Deflection**
#	s	N	Nm (J)	mm/s	mm
3	0.0243	663.4089	126.5	6,117.5600	155.0744
4	0.0244	808.2068	239.8	7,631.5333	185.8035
5	0.0245	605.0535	304.3	9,936.8022	253.0160
6	0.0246	1,008.4226	501.7	9,882.4844	229.0113

Testing of Panel #3

As per Table 4.4, Panel #3 is a Type-II bare panel with no hardening. This panel served as the reference panel for the Type-II series of panels. As the impactor would directly hit the bare glass, the applied impact energy was deliberately reduced to 15.993 N.mm. Table 4.6 shows the status just before the moment of impact. The damage process and resulting damage can be seen in

Figs. 4.13 (a) and 4.13 (b). As the impactor broke through the glass, the recorded displacement value for the impactor was very high.

(a) View of test in progress (b) Glass pane blown away, no damage to concrete

Figure 4.13. Complete shattering of glass pane during impact testing of Panel #3.

Video frames of the test at critical junctures are shown in Fig. 4.14 (a) to (e) and the views successively correspond in (a) first contact of plunger; (b) soon after first impact; (c) plunger rebound; (d) later stages of rebound; and (e) plunger return for second impact but the glass was gone after first impact.

(a) 50.73s (b) 50.77s (c) 50.83s (d) 51.71s (e) 51.93s

Figure 4.14. Critical stages of impact test of Panel #3.

It is evident from Fig. 4.15 that the failure was of elastic brittle type with maximum recorded plunger movement of 155 mm. Furthermore, as per Fig. 4.16, this case uses smallest of the four impact velocities. In this case, as expected, the glass had very low resistance against impact resulting in fully shattered glass with splinters flying, as evident from Fig. 4.14(b). It appeared from the video that the failure was almost instantaneous, and the impactor experienced zero resistance at 0.007 sec. As expected, there was no damage to concrete.

Testing of Panel #4

According to Table 4.4, Panel #4 is a Type-II panel with protective poly-film bonded to the back face of glazed area only. This test checked the effectiveness of the film in improving impact resistance of glass as compared to the bare unhardened glass in Panel #3. Table 4.6 shows the status just before the moment of impact. In this case, the impact energy is 23.32 N.mm, which is 46% higher than that for Panel #3. Plunger deflection vs. time plot is shown in Fig. 4.15. The damage process and the resulting damage can be seen in Figs. 4.17 and 4.18.

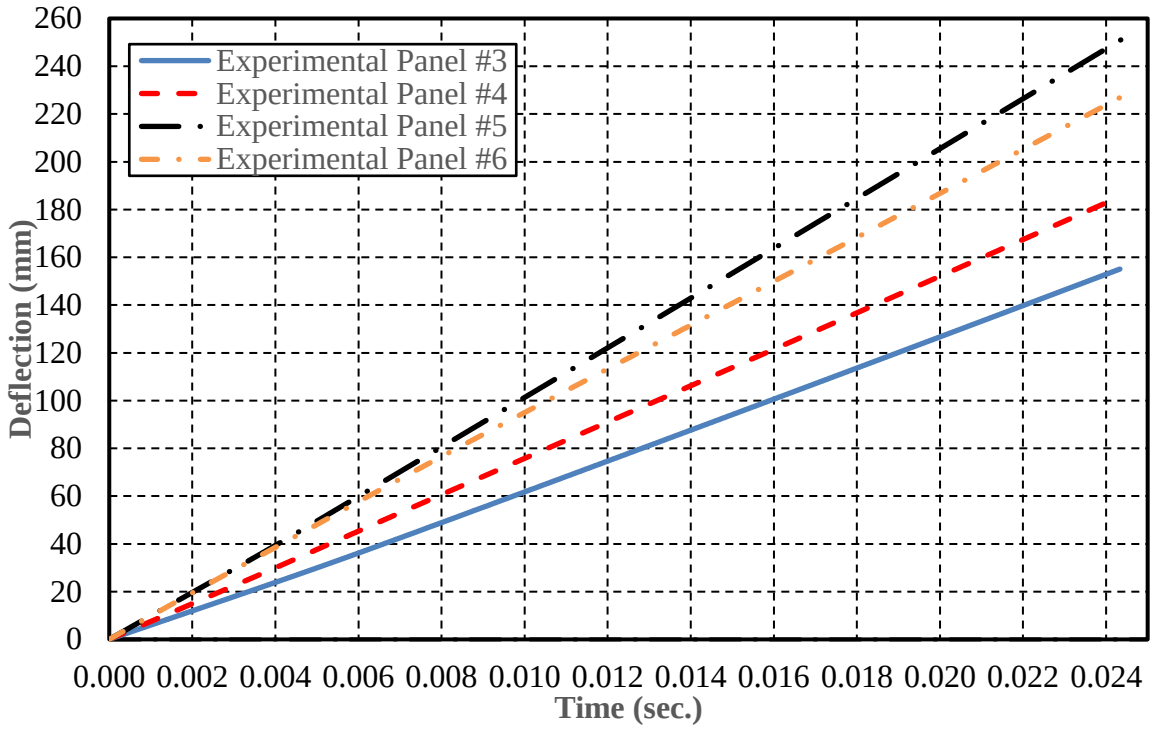

Figure 4.15. Experimental deflection vs. time curve for Type II panels.

It is evident from Fig. 4.15 that the performance of this panel was strikingly better than Panel #3. Although extensive cracking of glass pane did occur but without flying splinters, because the splinters remained bonded to the poly-film. In this case also the response was brittle. Early dip in the velocity response curve signifies energy transfer from plunger to glass pane and the subsequent plateau signifies little resistance offered by the panel after shattering of glass. However, the poly-film marginally increased the impact resistance and ductility. In this case, possible injury due to flying glass splinters was prevented, even with higher impact energy (Fig. 4.17a). Unlike

Panel #3, in Panel #4 the concrete experienced one bottom flexural crack in concrete, extending over the full width of the panel (Fig. 4.17b).

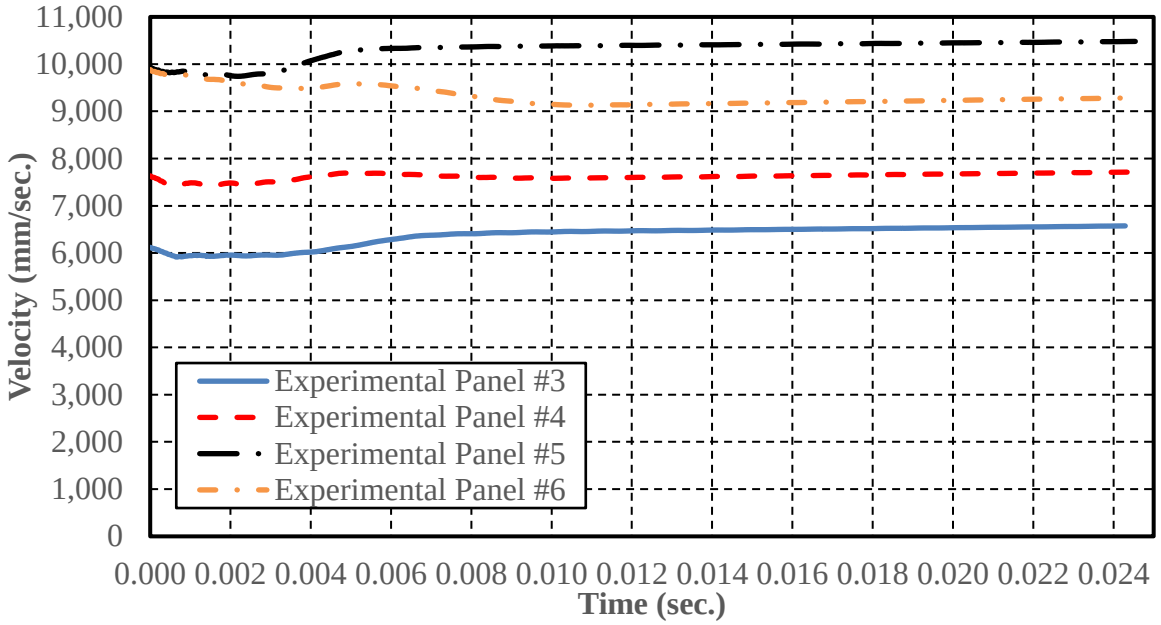

Figure 4.16. Experimental velocity vs. time curve for Type II panels.

(a) Shattered glass pieces captured by poly-film

(b) Back face primary crack across the width

Figure 4.17. Impact test of Panel #4.

Video frames of the test at critical junctures are shown in Fig. 4.18 (a) to (d) and the views successively correspond in (a) first contact of plunger; (b) momentarily after first impact tiny flying glass splinters appear on the impact side; (c) momentarily after plunger rebound, the poly-film with sticking glass splinters falls off; and (d) after first rebound the downward movement of plunger occurs but no resistance is offered by the panel.

(a) 00.17s (b) 00.20s (c) 00.33s (d) 00.37s

Figure 4.18. Critical stages of impact test of Panel #4.

Testing of Panel #5

Panel #5 is a Type-II panel with back face of the glass as well as concrete hardened by adhesive film. This panel allowed finding out the effectiveness of the hardening process of Panel #4 with hardening poly-film applied to the glass pane only. Table 4.6 shows the status of impact test right at the instant the impactor comes in contact with the panel. In this case the applied impact energy is 24.21 N.mm, which is only 4% higher than that applied on Panel #4. Deflection vs. time plot curve at the point of impact test is shown in Fig. 4.15. Further reduction of the slope of the curve compared to Panels #3 and #4, signifies higher stiffness and continued improvement in performance. The slope of the curve is 10 m/s. The state of final damage is shown in Figs. 4.19.

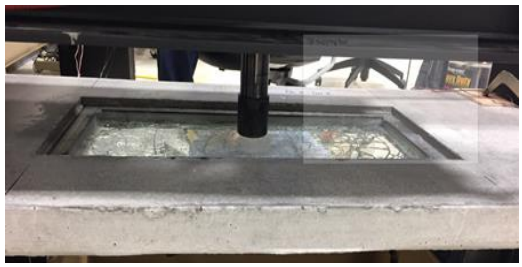

Figure 4.19. Damaged Panel #5.

Video frames of the test at critical junctures are shown in Fig. 4.20 (a) to (c) at time instances of 46.10s, 46.13s, and 48.43s. The frames refer successively to (a) first impact event; (b) plunger rebound; and (c) approach for second impact which does not occur due to permanent deformation in the panel.

(a) 46.10s (b) 46.13s (c) 48.43s

Figure 4.20. Critical stages in impact test of Panel #5.

In this case also the glass pane shattered but stayed in place. As before, no damage was noticed in the back of the panel.

Testing of Panel #6

Panel #6 is a Type-II panel with hardening done to both back and front face of glass and only to back face of rest of the panel. This panel allowed finding out if additional hardening of impact side of the glass pane in Panel #5 can noticeably improve the impact resistance. Table 4.6 shows the status of impact test right at the time the impactor touches the panel. In this case, the applied impact energy was 36.24 N.mm, which is 50% higher than what was used for Panel #5. Deflection vs. time plot for the point of impact test is shown in Fig. 4.15. The damage process and the state of final damage can be seen in Figs. 4.21(a) and 4.21(b). It is evident from Fig. 4.15 that stiffness of Panel #6 is higher than that of Panel #5. It also shows increase in stiffness as compared to Panel #5. Video frames of the test at critical junctures are shown in Fig. 4.22(a) to (e) and the views successively correspond in (a) plunge in position just at the point of impact; (b) rebounding of plunger; (c) second impact to be followed by rebound; and (d) third impact to be followed by rebound; and (e) final stationary position of plunger after failing to impact the panel fourth time.

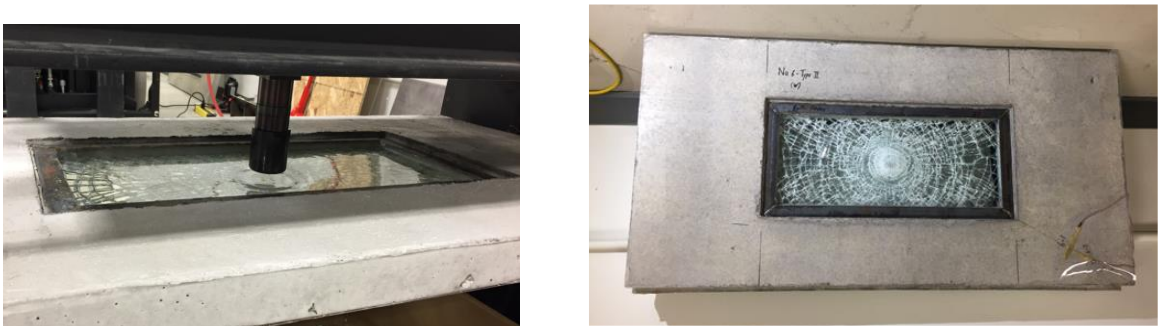

(a) View of test after damage (b) View of back face damage

Figure 4.21. Impact test of Panel #6.

(a) 17.47s (b) 17.53s (c) 18.77s (d) 19.50s (e) 20.07s

Figure 4.22. Critical stages of impact test of Panel #6.

As expected, the performance of this panel was best of the four Type-II panels considered, except that cracking of glass could not be avoided because of the local effect of the impactor directly hitting an amorphous material like glass. The slope of the curve is 9.32 m/s.

4.4.3 Strain History of Impact Loading

The acquisition of strain data was undertaken for Panels #1 and #2 only. Unfortunately, however, in the case of Panel #1, the data acquisition system malfunctioned, and strain recording were found to be useless. So, the following discussion pertains to Panel #2 only. The strain-gage locations are shown in Appendix A (Fig. A7 of Section A9). The details of strain data acquisition are given in Appendix A. The acquired raw strain data required calibration to remove static offset followed by filtering to remove all background noise. The resulting strain data for gages SG1, SG2, and SG3 are shown in Figs. A11, A12, and A13 (Appendix A). These plots indicate that the panel continued to undergo oscillations after the local impact event was over. According to the plots, the recorded local impact effect lasted for less than 0.025 sec. (or, $1/40^{th}$ sec); whereas, global oscillations continued well beyond 1 sec, as evidenced by the strain data records for 10 seconds. As expected, due to its closer proximity, the initial strain amplitudes for SG1 at any instant of time are larger than those for SG2 and SG3. Also, the attenuation of amplitude with time indicates energy dissipation, mostly, in damping and wave propagation.

Magnified view of strain plot for SG1, SG2, and SG3 in Fig. A11 to A13 (Appendix A) for the first 0.025 sec are shown in Figs. 4.23 to 4.25 It appears from the plot that the first peak represents the arrival of shock wave at the strain gage location, which occurs at less than 0.01 second. The slight oscillations in the plots, most likely, are leftover high frequency artifacts from the data acquisition system. The plot also indicates that the primary frequency of oscillation of the

panel is close to 57 Hz. The strain amplitudes show difference depending upon gage location and orientation.

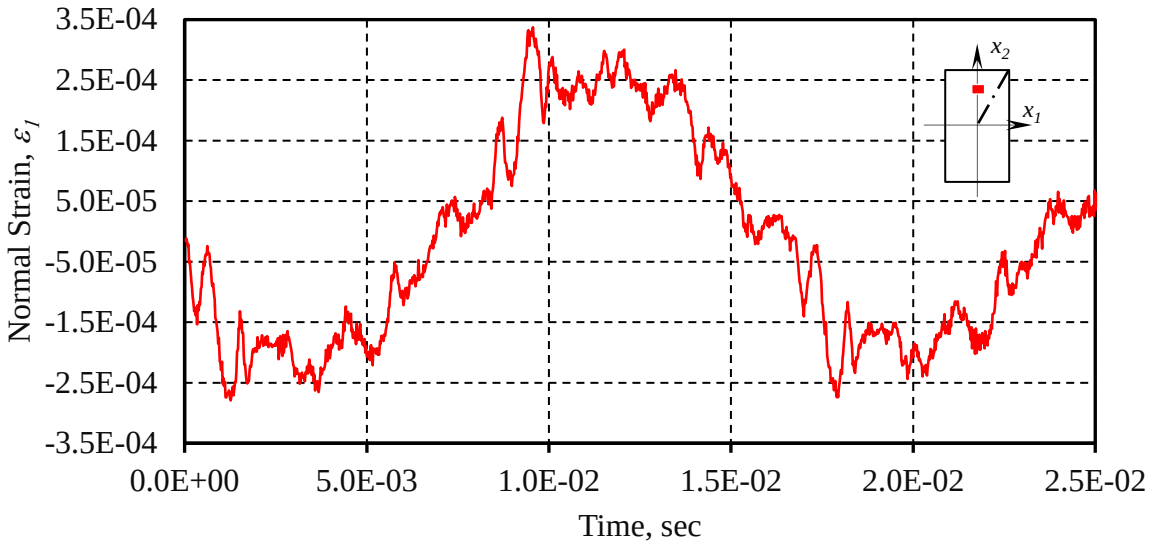

Figure 4.23. Strain vs. time history of gage SG1 in Panel #2 for the first 0.025 s.

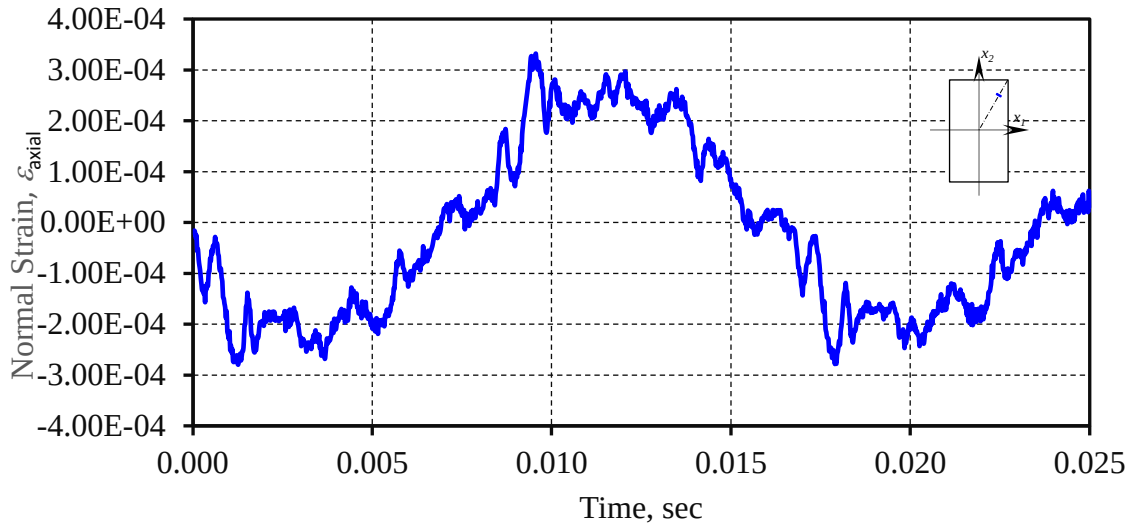

Figure 4.24. Strain vs. time history of gage SG2 in Panel #2 for the first 0.025 s.

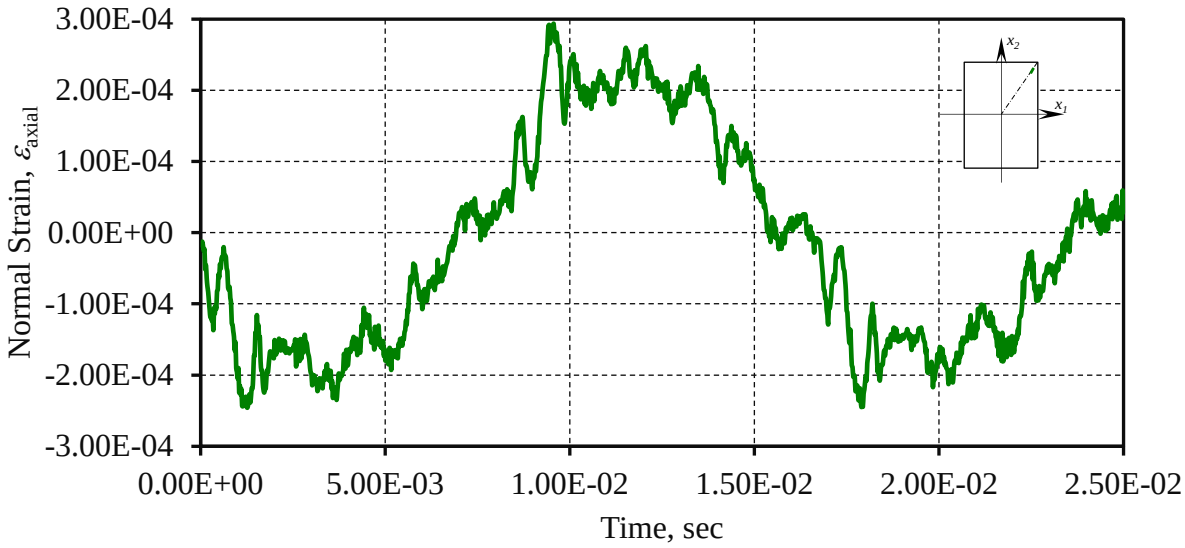

Figure 4.25. Strain vs. time history of gage SG3 in Panel #2 for the first 0.025 s.

4.5 General Observations and Summary

This chapter discusses the machine specification, detailing and fabrication of Test Panels, and test procedures in detail. Keeping in mind the objectives of experimental work mentioned in section 4.4, the tests were undertaken carefully to meet those objectives. The impact testing machine was solely operated by LASIR personnel. So, the investigator had to rely upon their expertise and experience with the machine. The investigator made sure that the machine was properly calibrated before the tests were undertaken. The panels were tested by applying different magnitudes of impact energy, primarily yielding the deformation vs. time data. Due to instrumental error, the measured strain values were not found to be reliable.

The experimental test data from the impact tests on corner supported panels with and without bonded protective film confirmed the effectiveness of protective films in significantly enhancing the impact resistance of the panels, particularly in the case of solid panels. This is especially significant because no test results have been reported in the published literature for the worst possible support condition used in this study.

Based on the results of Panels #4 to #6, it may be stated that the protective film applied to the glass pane did not prove to be very effective, at least, for the level of impact energy used. In all these cases, the damage was mostly localized in the glass area and the strength of the concrete part of such panels was mobilized minimally. To prevent such failure significantly more expensive

specially reinforced (or bulletproof) glass needs to be used. Also, for superior performance, the film needs to be more securely adhered to glass as well as frame supporting the glass pane. The use of thicker boundary anchored adhesive film may enhance the impact resistance of glazed panels.

CHAPTER 5

NUMERICAL SIMULATIONS

5.1 Introduction

Numerical simulations were undertaken using the commercial software Abaqus CAE 2019 with three objectives.

a) First, the numerical models are validated with the experimental data for solid Panels #1 and #2 presented in Chapter 4. In doing so, the simulation results with two concrete models, namely, CDP and HJC, discussed earlier are evaluated to identify the best model suited for undertaking the studies under (c).
b) Secondly, the relative suitability of CDP and HJC models in simulating the response of remaining four panels (#3 to #6) with glazed cutouts is determined.
c) Finally, the performance of bare and hardened solid panels under the influence of increasing magnitude of impact energy, as shown in Table 5.1, is evaluated. The three cases considered for this purpose are
    i) Panel #1: Bare solid panel.
    ii) Panel #2: Solid panel with poly-film hardening in the back face only
    iii) Panel #2b: Solid panel with poly-film hardening in both front (or impact) and back faces.

Here, Panels #1 and #2 are same as the ones originally considered for validation purposes.

Table 5.1. Summary of different impact energies used in the simulations.

Panel #	Hardened	Impact Energy (J)				Drop Weight	Velocity (m/s)			
		Case 1	Case 2	Case 3	Case 4		Case 1	Case 2	Case 3	Case 4
1	No	873.7	1310.5	1747.3	1766.85	466.84N	6.06096	7.42313	8.5715	8.61924
2	Back Face	1766.85	1747.3	2650.27	3533.7	597.61N	7.6180	7.57582	9.3301	10.7735
2b	Both Faces	-	2650.3	3533.7	4417.1	597.61N	-	9.33013	10.774	12.0452

In the above table, Case 1 of Panels #1 and #2 represent the original test panels. Corresponding impact energies used during testing were 873.7 (say, I_1) and 1767.8 (say, I_2),

respectively. A close examination of Table 5.1 reveals that Panel #1 was simulated with impact energies of I_1, $1.5I_1$, $2I_1$ and I_2. Panel #2 was simulated with impact energies of I_2, $2I_1$, $1.5I_2$ and $2I_2$. Finally, Panel #2b was simulated with impact energies of $1.5I_2$, $2I_2$, and $2.5I_2$. The objective is to investigate the performance with increasing impact velocity. In the end, the results for regular and hardened panel are compared to critically assess the extent of effectiveness of the proposed simple hardening scheme.

5.2 Calibration of Material Parameters

In Chapter 3, the two phenomenological models of concrete, namely, CDP and HJC, were discussed in detail. Careful calibration of material parameters driving these models with respect to the actual materials used in the present study is a necessity based on the material used in this study. The methods used for the purpose were discussed in Section 3.2.3.

5.2.1 CDP Model

The mechanical properties of 2,400 kg/m^3 concrete used in the low impact velocity tests were:

$$f_c^{'} = 41.93\text{MPa};\ f_t = 3.34\text{MPa};\ f_{bc}^{'} = 1.21 f_c^{'} = 50.3\text{MPa [33]};\ E_c = 29,405\text{MPa};\ \nu = 0.15$$

The corresponding values for CDP model parameters used in this study are

$\alpha = 0.143,\ \gamma = 0.2857,\ m = 0.1,\ \psi = 36^o,$ and viscosity parameter, $\mu = 0$.

5.2.2 HJC Model

Holmquist et al. used test data by Hanchak et al. [87] for 48 MPa concrete to determine the parameter value manually, as reported in [82]. In the present study, the same values were used as the starting point values for calibration using Isight, for the 41.93 MPa concrete used in the present research. The resulting modified parameter values are shown in Table 5.2. The value of the density parameter is ρ_o = 2400kg/m^3.

Table 5.2. HJC (modified) parameter values for concrete.

Strength Parameters	f_c'	T	G	S_{max}	A	B	N
	41.93 MPa	3.34 MPa	12.785 GPa	7.00	1.00	1.72	0.61
Pressure Parameters	p_{cr}	μ_{cr}	p_{lock}	μ_{lock}	K_1	K_2	K_3
	16 MPa	0.001	800 MPa	0.100	85 GPa	-171 GPa	208 GPa
Damage Parameters	D_1	D_2	$\varepsilon_{f\,min}$	Strain-rate Parameter	C	-	-
	0.50	1.0	0.01		0.033	-	-

5.3 Numerical Simulation of Test Panels #1 and *#2*

The simulations were undertaken with CDP model without strain-rate effect and the HJC model by including the strain-rate effect, in line with the considerations discussed in Chapter 3. The finite element model comprised of

- 14090 tetrahedral (C3D4) elements for concrete panels.
- 12396 wire (B31) elements for steel reinforcement.
- 4911 tetrahedral (C3D4) elements for polyethylene film.

The Model of Panel #2 is shown in Figs. 5.1 and 5.2. The execution time of typical runs based on a i7-4500U 4 core CPU with 8 GB RAM is given in Table 5.3.

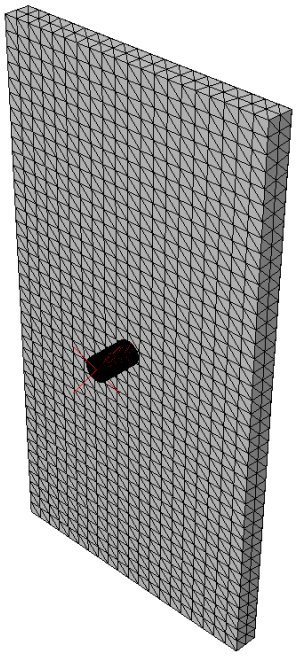

Figure 5.1. Panel #2, impact face.

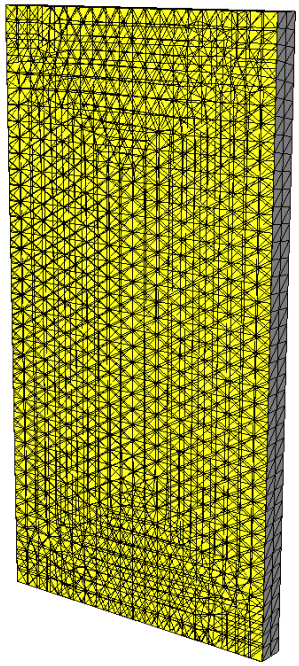

Figure 5.2. Panel #2 back face—protective film.

Table 5.3. Typical wall clock execution time for Panels #1 and #2.

Panel #	CDP Model	HJC Model
1	6507 sec	5166 sec
2	17764 sec	19699 sec

5.2.1 Displacement vs. Time Results

The simulation results and experimental values for Panels #1 and #2 are compared in Figs. 5.3 and 5.4. The experimental displacement values are for the impacting mass; whereas, the simulation values correspond to the center of panel.

Prediction of displacement near the beginning and end of the test seems to agree. The higher displacement predictions in the intermediate time range may be attributed to the fact that test data is for projectile displacement and the simulated data is deflection at the center of panels. During simulation, the full contact force impact acts at zero time; whereas, during testing small time lapse occurs before the full impact force is realized. Moreover, unrecognized artifacts in the test data may be responsible for the noticeable discrepancy in the intervening time. As the test

velocity was in the low range, both CDP and HJC model results tend to agree, most likely, due to negligible strain-rate effects..

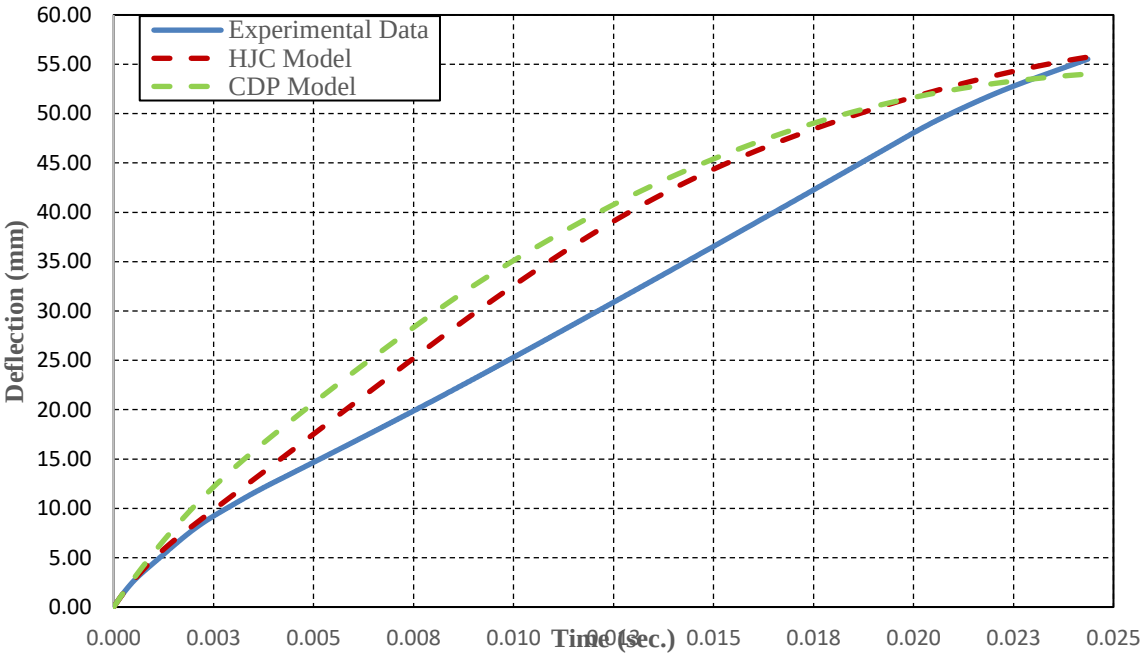

Figure 5.3. Displacement vs. time curves for Panel #1.

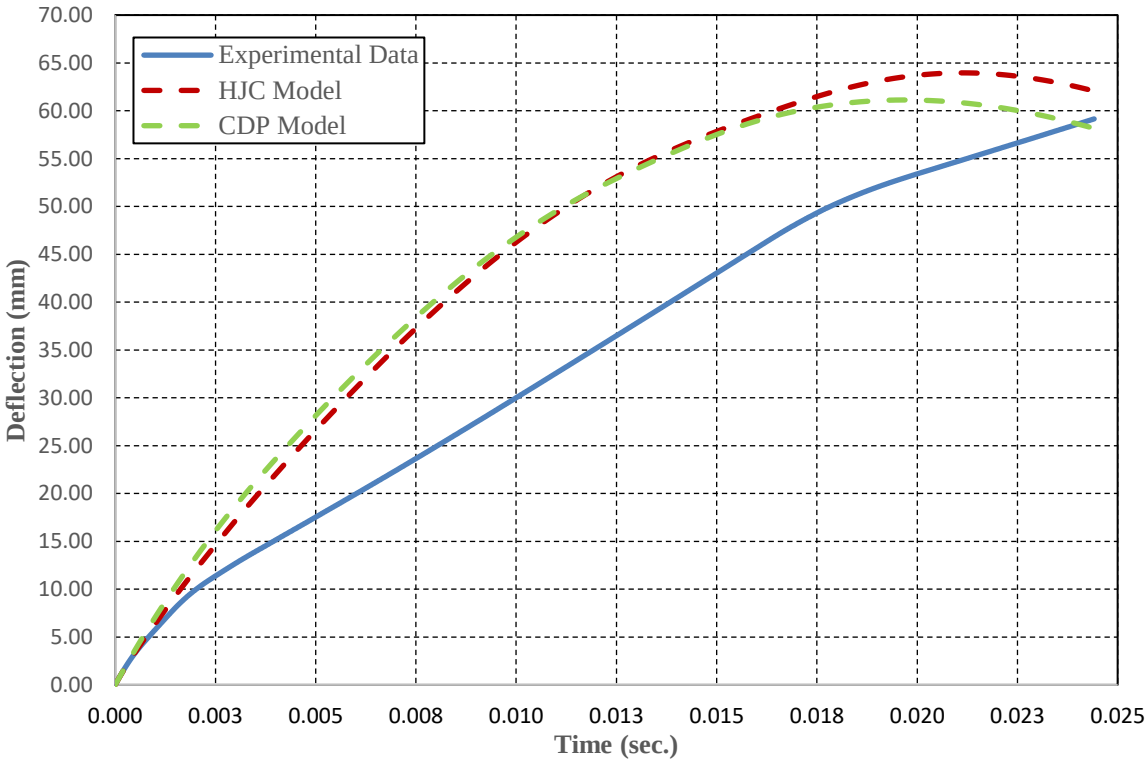

Figure 5.4. Displacement vs. time curves for Panel #2.

The instantaneous deflected shapes for Panels #1 and #2 at time instant 0.0244 sec are shown in Figs. 5.5 (a to d). Panel #2 shows more flexibility in the transverse direction. The center point deflections for the four cases are shown in Table 5.4.

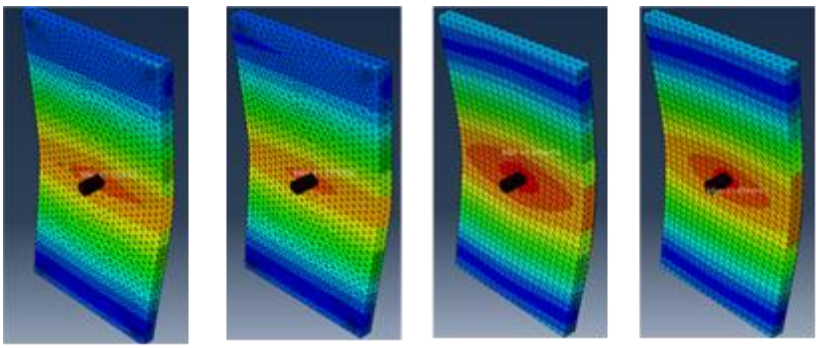

(a) Panel 1: HJC; (b) Panel 1: CDP; (c) Panel 2: HJC; (d) Panel 2: CDP

Figure 5.5. The deflected shapes for Panels #1 and #2 at time instant 0.0244 sec.

Table 5.4. The center point deflections for Panels #1 and #2.

Description	**Panel 1**	**Panel 2**
Projectile Velocity	6.06 m/s	7.618 m/s
HJC Model	57.59 mm	62.68 mm
CDP Model	52.37 mm	**5.39** mm

5.3.2 Velocity vs. Time Results

The simulation results and experimental velocities for Panels #1 and #2 are compared in Figs. 5.6 and 5.7 The discrepancy between test and simulation can be attributed to the differences in response characteristics between the impactor and the panel.

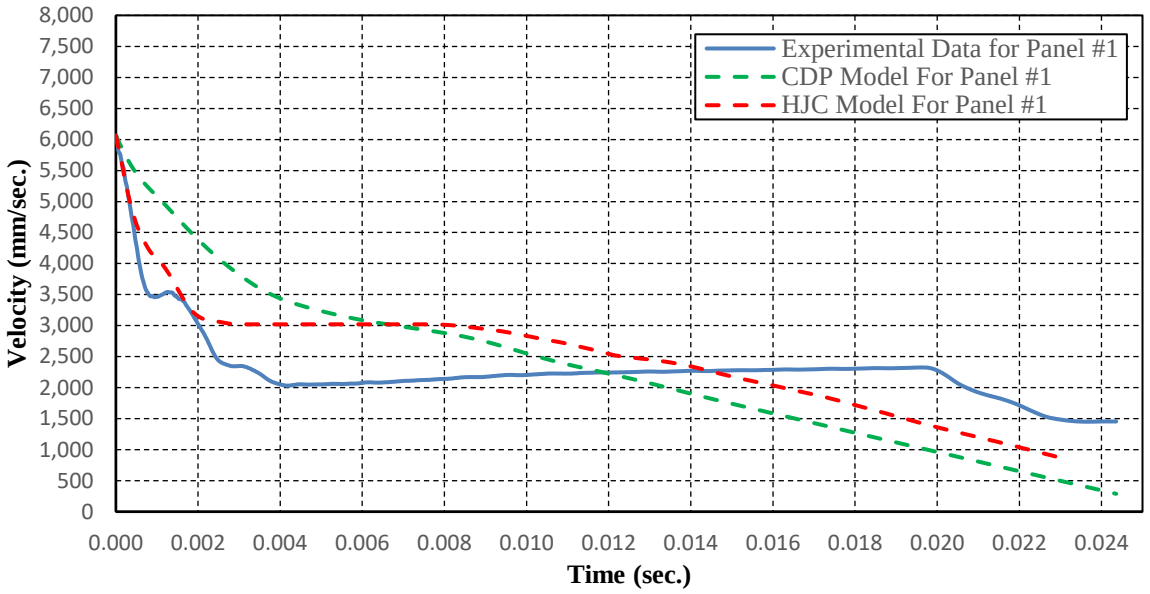

Figure 5.6. Velocity vs. time curve for Panel #1.

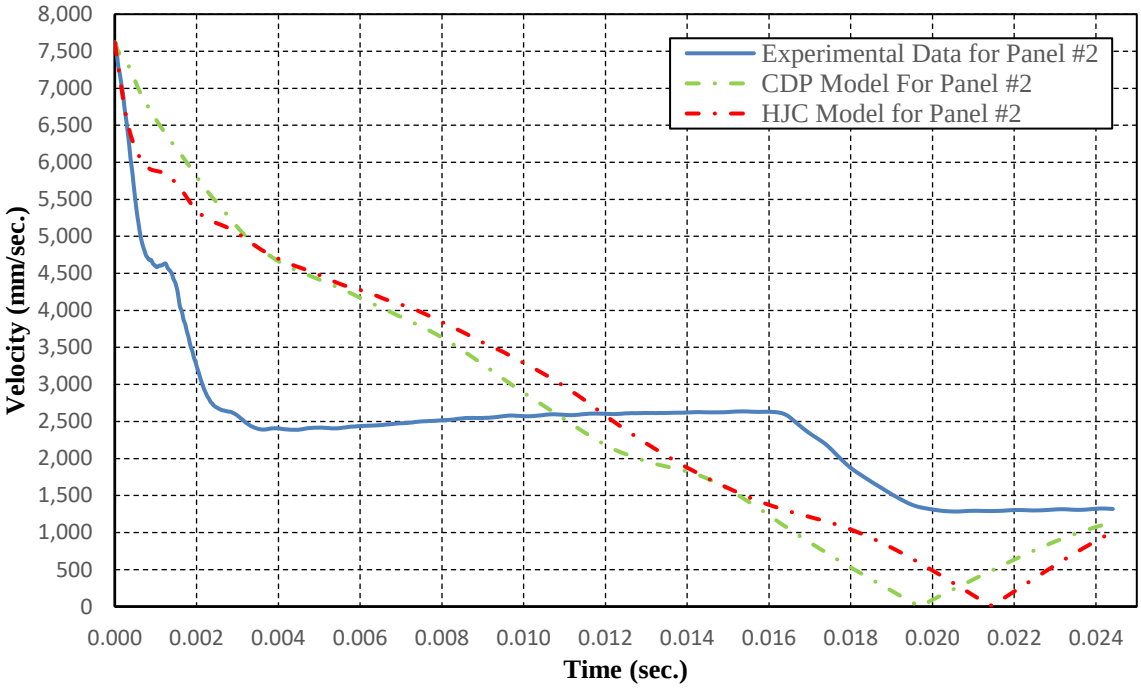

Figure 5.7. Velocity vs. time curve for Panel #2.

5.3.3 Damage Prediction in Panels #1 and #2

For both panels, concrete damage was examined in the back face of concrete in terms of the value of the damage parameter. In addition, for Panel #2, the damage measure in the bonded

film is expressed in terms of the Mises equivalent stress value defined as: $\sigma_{eq} = \sqrt{\frac{3}{2}\tilde{\sigma} : \tilde{\sigma}}$, where $\tilde{\sigma}$ is the deviatoric stress tensor.

Damage in Panel #1

As mentioned in Chapter 2, Section 2.1.1, the degree target damage is related to the magnitude of impact energy being dissipated. The low-velocity projectile tends to cause global damage but under high-velocity local damage is more pronounced. In this context, a comparison of the numerical simulation based damage pattern and crack patterns from experimental observation shown in Chapter 4 is needed. Figs. 5.8 and 5.9 show the predicted damage patterns based on HJC and CDP models.

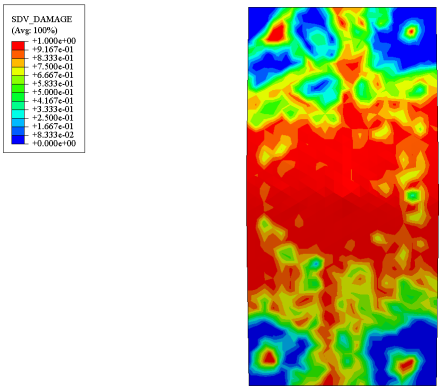

Figure 5.8. HJC model damage patterns of the back face of Panel #1.

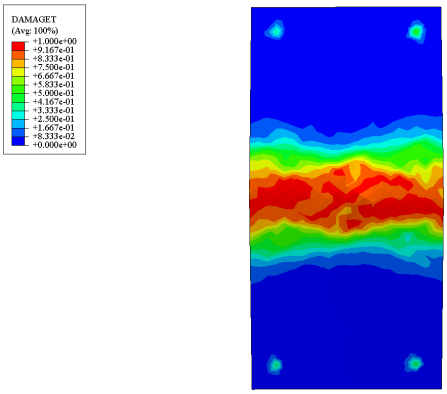

Figure 5.9. CDP model damage patterns of the back face of Panel #1.

HJC prediction of significant global damage is consistent with test results. In this regard, the performance of CDP model deemed to be relatively poor.

Damage of Panel #2

Panel #2 consisted of polyethylene film bonded to the back face of the concrete panel. In this case, the damage patterns in the back face of concrete obtained by HJC and CDP models are shown in Figs. 5.10 and 5.11. A comparison of these damage patterns with the experimental data of Chapter 4 shows consistently better agreement between HJC predictions and test results. Also, HJC model predictions showing significant global damage is consistent with test results.

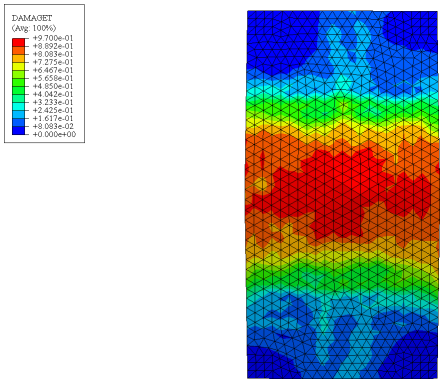

Figure 5.10. CDP prediction of damage patterns in the back face of Panel #2.

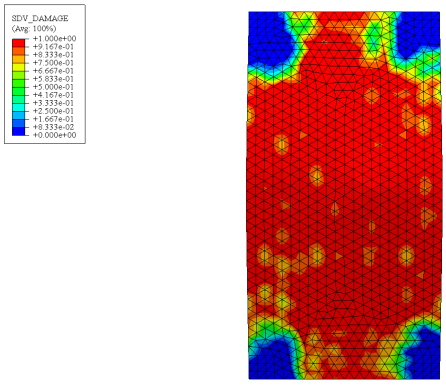

Figure 5.11. HJC prediction of damage patterns in the back face of Panel #2.

Damage in Polyethylene Film

The damage patterns in the polyethylene film bonded to back of Panel #2 predicted by CDP and HJC models show close resemblance. The degree of damage in the polyethylene film involved comparison of the maximum equivalent stress obtained by HJC and CDP models with the experimental base strength test shown in Appendix A (Table A2 and Fig. A8). The equivalent stress obtained by CDP and HJC models are shown in Figs. 5.12 and 5.13 respectively. The maximum equivalent stress for both models is equal to 66.88 MPa and the test yield strength of the polyethylene film is equal to 90 MPa. In other words, as the stress level experienced by the film stays within the elastic zone, the polyethylene film itself does not undergo any damage. The damage is primarily local and/or global bond failure.

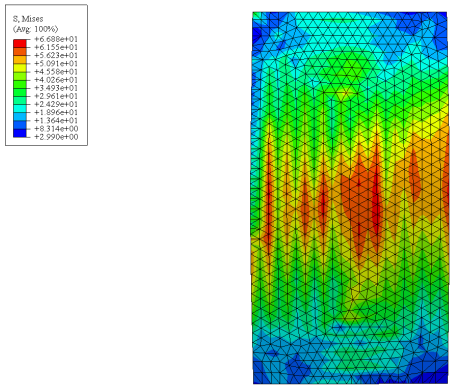

Figure 5.12. Equivalent stress in polyethylene film by CDP model.

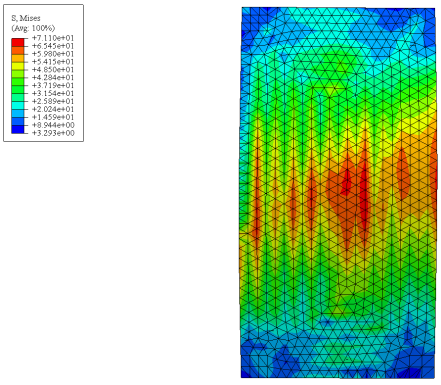

Figure 5.13. Equivalent stress in polyethylene film by HJC model.

In Figs. 5.8 to 5.11, deep red areas signify that concrete in the back face of the panels has cracked or about the crack. The deep blue areas represent no cracking. In the case of poly-film, the

gray banded areas represent largest effective stress locations. The maximum poly-film stress predicted by CDP was less than that with HJC.

5.4 Numerical Simulation of Test Panels #3 to #6

In this section, the CDP and HJC model based simulation results for Panels #3 to #6 characterized by glazed window openings are presented. Apart from deflection and velocity values, damage experienced by the panels are considered. The results are compared with those observed from experimental studies presented in Chapter 4.

5.4.1 Deflection vs. Time

The time history of deflection for Panels #3 to #6 are presented for a time interval close to 0.025 sec.

Simulation Results for Panel #3

As stated in Table 4.4, this Type II panel did not undergo any hardening measure. As can be seen in Fig. 5.15, the deflection history predicted by numerical simulation based on CDP and HJC models agreed closely. The maximum displacement with both models was 145 mm; whereas, the experimental value was 155 mm. In other words, simulation predictions underestimated the experimental value by a small margin of 6.45%. The glass pane modeled with 2 layers of C3D4 element type and with 30786 number of elements as shown in Fig. 5.14.

Simulation Results for Panel #4

According to Table 4.4, this Type II panel has poly-film bonded to the back face of glass pane only. As in the case of Panel #3, the time history of simulation based on CDP and HJC models, as shown in Fig. 5.15, also agreed closely. The experimental displacement was 185 mm, and the maximum displacement of the two models was 174 mm. which is 11 mm lower than the experimental result. However, this discrepancy of 5.4% is limited to the maxima value. Otherwise, the simulation and experimental plots of deflection-history showed excellent agreement.

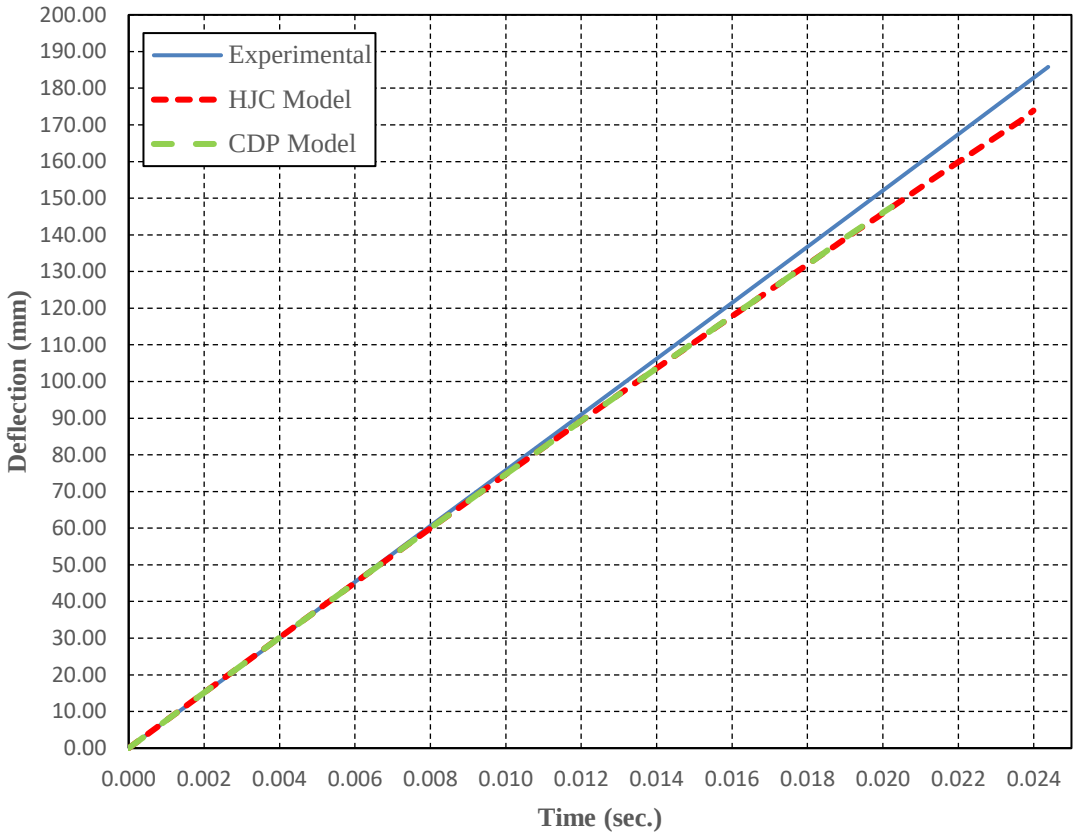

Figure 5.14. Displacement vs. time plots for Panel #3.

Figure 5.15. Displacement vs. time plots for Panel #4.

Simulation Results for Panel #5

According to Table 4.4, this Type II panel has polyfilm bonded to the back face of the panel, including the glass pane. In this case, apart from good agreement between CDP and HJC model results, the maximum predicted CDP and HJC deflection value are 230 mm. This is smaller than maximum experimental value by 20.52 mm (or, 8.19%). The time history of simulation based on CDP and HJC models, are shown in Fig. 5.16.

Simulation Results for Panel #6

According to Table 4.4, this Type II panel has polyfilm bonded to the back whole back face of panel and front faces of glass pane. In this case, apart from good agreement between CDP

and HJC model results, the maximum predicted CDP and HJC deflection value are 221 mm. This is smaller than maximum experimental value by 7.98 mm (or, 3.35%). The time history of simulation based on CDP and HJC models, as shown in Fig. 5.17.

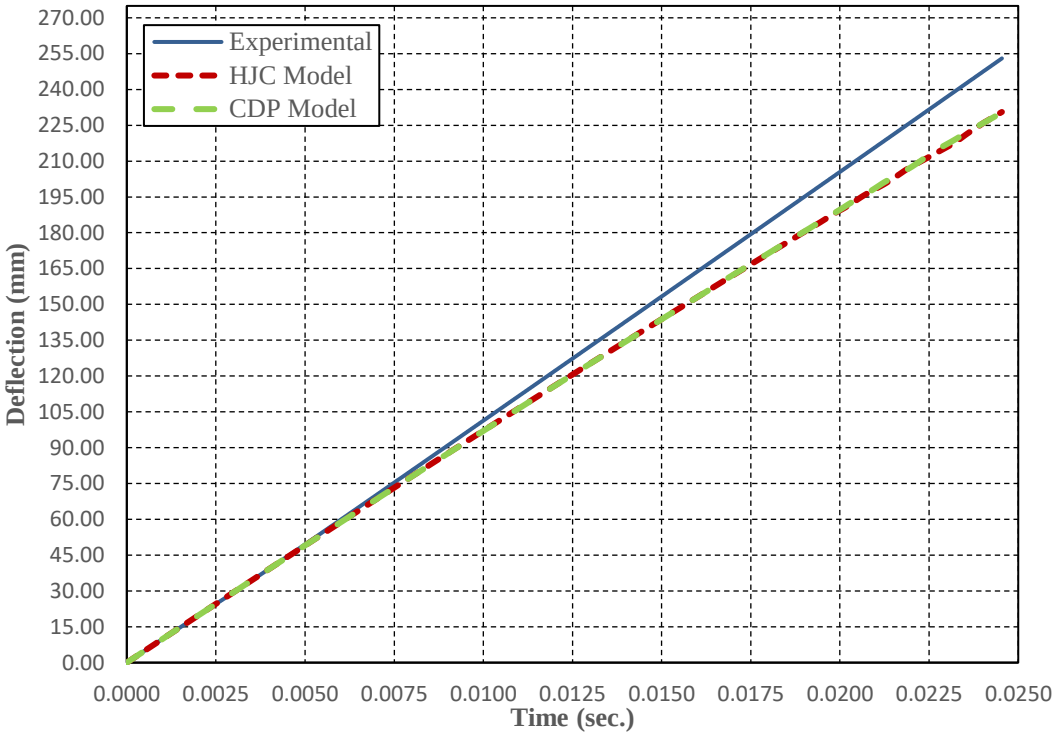

Figure 5.16. Displacement vs. time plots for Panel #5.

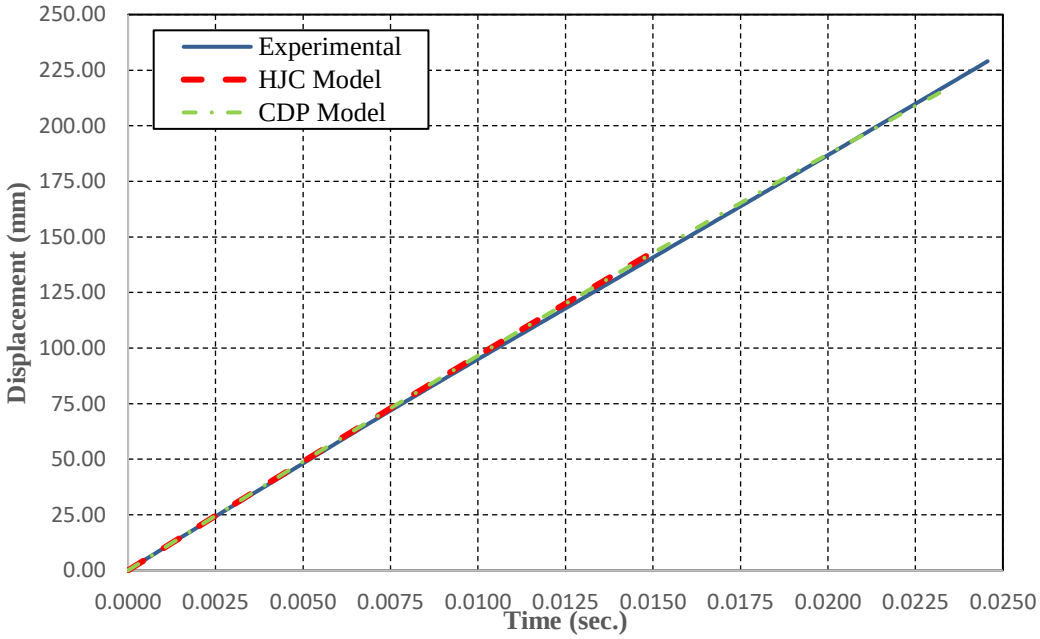

Figure 5.17. Displacement vs. time plots for Panel #6.

5.4.2 Damage Simulation Results of Panels #3 to #6

In all these four panels, the damage was found to be confined to the glass pane. For Panel #3 the shattered glass pane pieces were blown away, with no noticeable damage to concrete. As confirmed in Fig. 5.18, the glass pane was completely shattered with very little visible distress in the surrounding concrete.

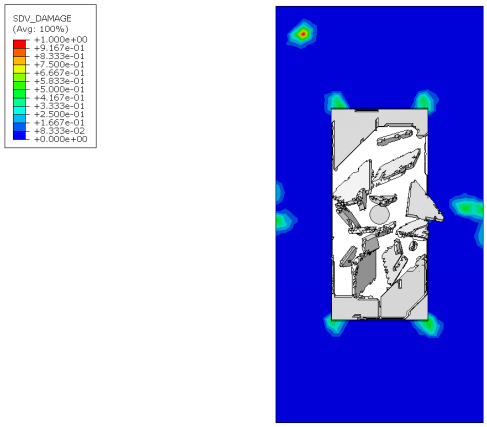

Figure 5.18. Damage of Panel #3.

In the case of Panels #4 to #6, the bonded polyethylene film served the purpose of holding the fractured glass pane in place, preventing flying of glass fragments. In the case of Panels #5 and #6, the polyethylene film seemed to improve global performance by superior transfer of load to the concrete part, as evidenced in Fig. 5.19.

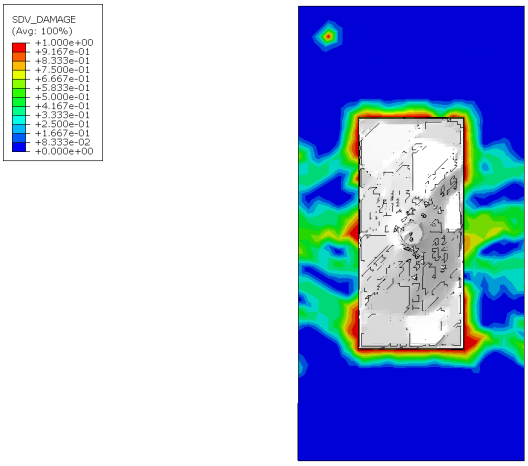

Figure 5.19. Damage of the back face of Panel #4.

5.5 Exploratory Simulation of Panels #1, #2 and #2b with Higher Impact Energy

In accordance with the impact energy details of cases shown in Table 5.1, four simulations were undertaken for each of the Panels #1 & #2, and three simulations for Panel #2b which has bonded poly-film in both the faces. Here, the objective is to investigate the relative performance of the three panels when subjected to higher impact energy by using increasing values of impact velocity, as detailed in Table 5.1. In the end, the results for regular and the two hardened panels are compared to critically assess the extent of effectiveness of the proposed simple hardening scheme. It was noted earlier that the performance of HJC model is superior to the CDP model. Furthermore, with HJC model the strain-rate effect can be allowed for, unlike with the CDP model. To further explore the performance of HJC, the deflection history of Panel #1 based on HJC model for top and bottom faces as well as that of impactor are shown in Fig. 5.20. Slightly larger deflection in the top face can be attributed to more acute compression effect near the top surface than near the bottom surface. It is also interesting to note that, as expected, the top face and impactor deflections are almost the same beyond 0.007 second. As noted in recorded time frames in the experimental data, the small disagreement of deflection value in the earlier segment can be attributed to small duration impactor rebound.

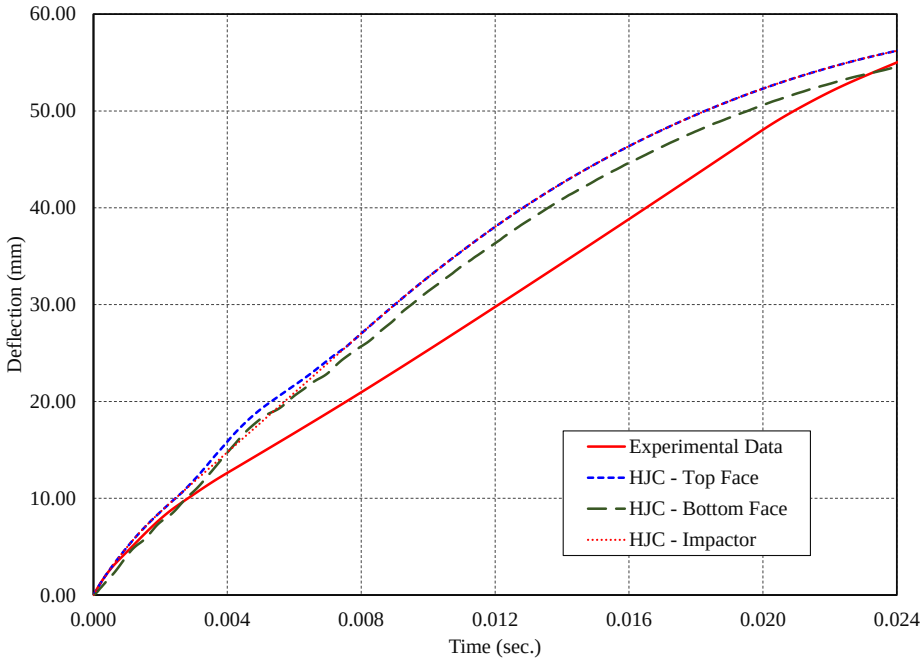

Figure 5.20. Displacement vs. time plots for Panel #1.

5.5.1 Deflection vs. Time Response of Panels #1, #2 and #2b

Panel #1: The predicted deflection vs. time responses of the bare panel using different impact energies is shown in Fig. 5.21. Panel #1 was simulated with impact energies of I_1, $1.5I_1$, $2I_1$ and I_2, which corresponded to impact velocities of 6060.96, 7423.13, 8571.49 and 1766.85 mm/sec, respectively. It is evident from this figure that as the impact energy is increased by 50% (i.e., to $1.5I_1$), the deflection increased by 38%. With 100% increase in impact energy ($2\ I_1$), the deflection increases by 64%. So, with higher impact energy, the relative increase in deflection is not proportional.

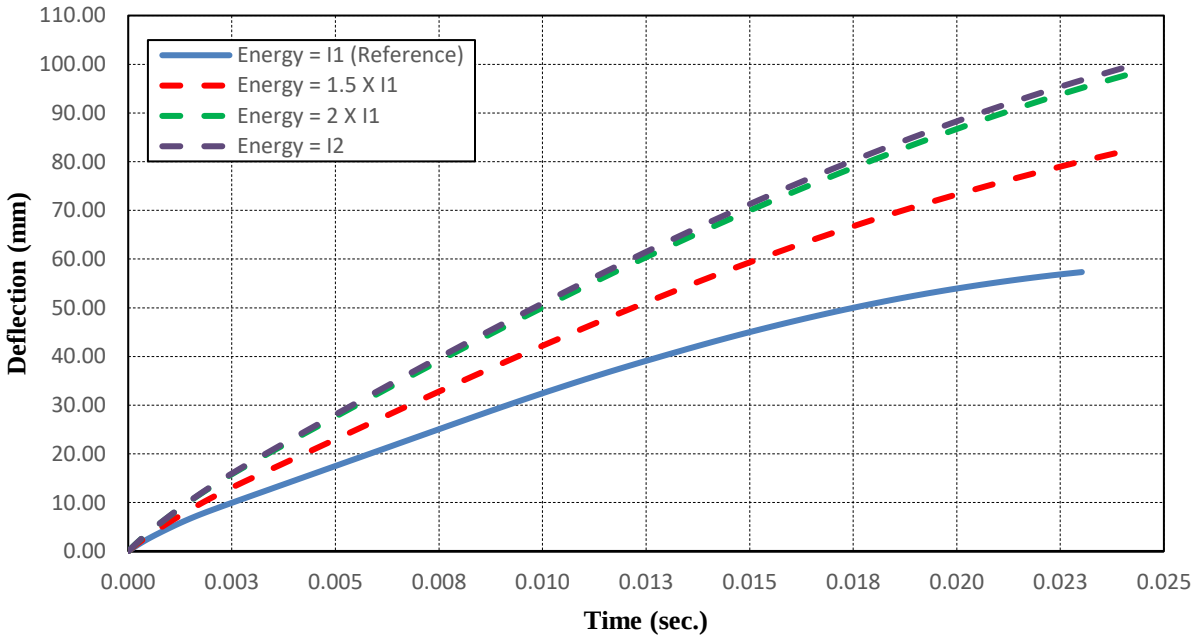

Figure 5.21. Central deflection vs. time curves for Panel #1 with different energies.

Panel #2: The deflection vs. time responses of this panel, having hardening in the back face only, are shown in Fig. 5.22 for impact energies of I_2, $1.5I_2$ and $2I_2$. The corresponding impact velocities are 7618, 9330 and 10774 mm/sec, respectively. With impact energy I_2 = 1766.9 J, which is almost equal to $2I_1$ = 1747.3 J, the deflection of the back face hardened Panel #2 relative to bare Panel #1 drops by about 37%. On the other hand, the deflection due to $2I_2$ shows an increase by 36% over that due to impact energy of I_2.

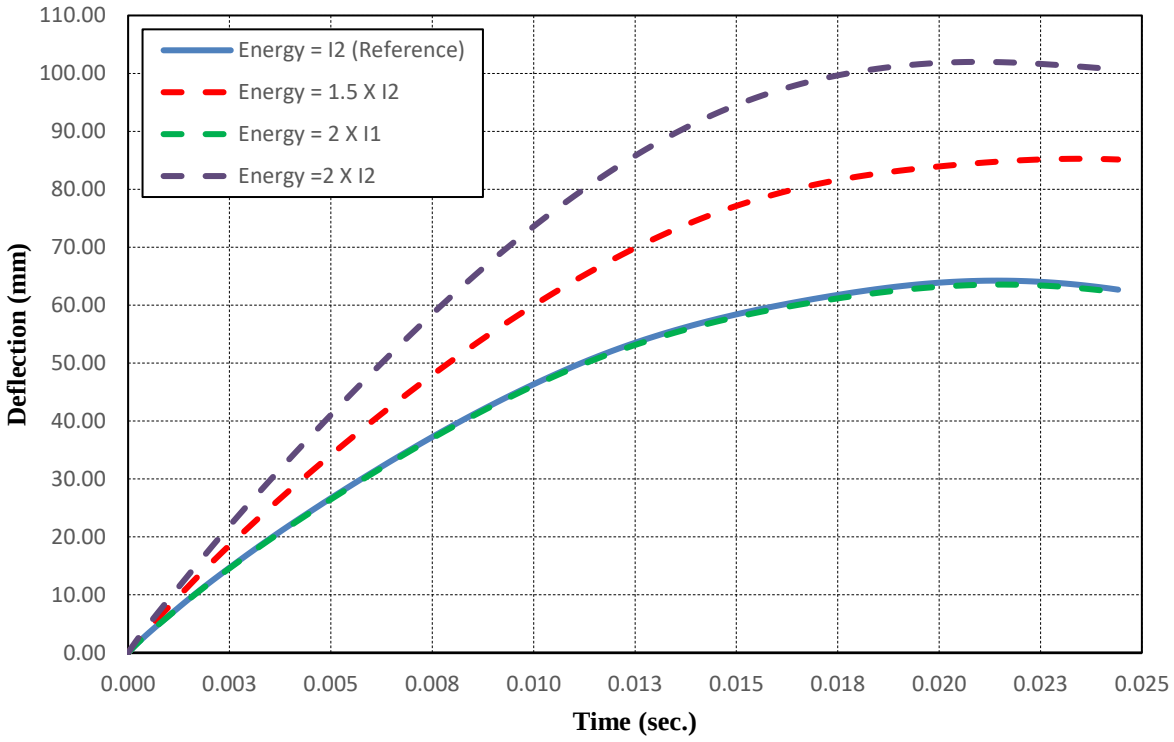

Figure 5.22. Deflection vs. time curves for Panel #2 with different energies.

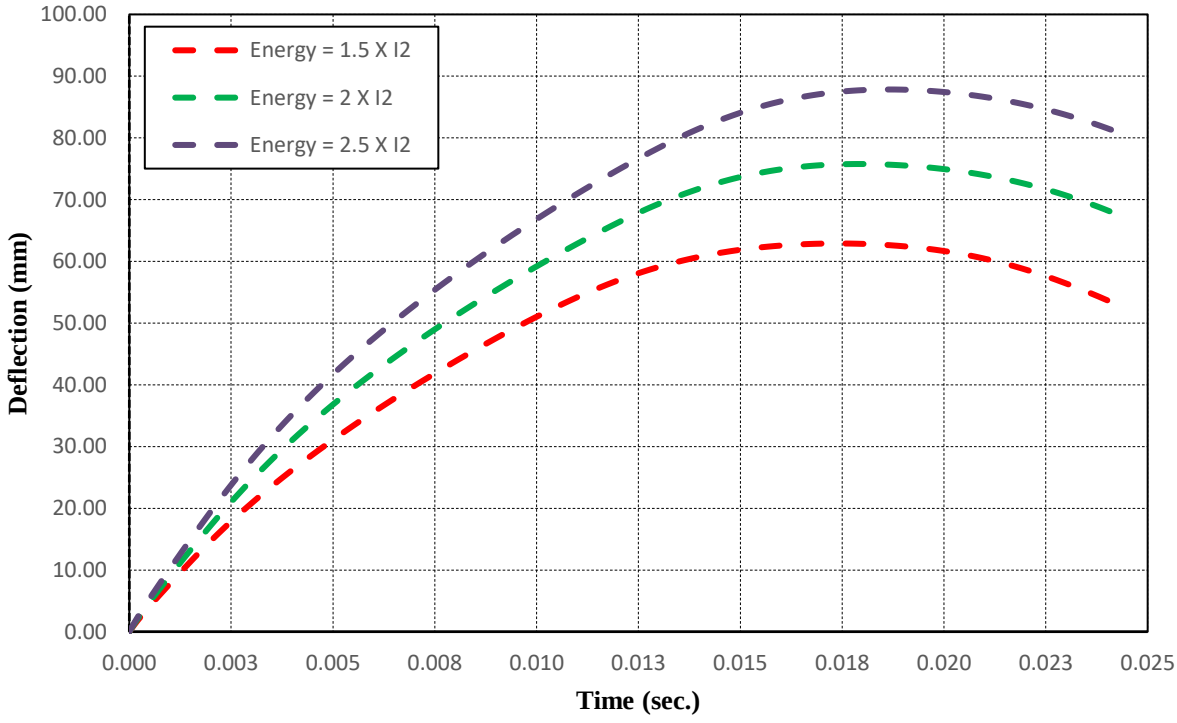

Figure 5.23. Deflection vs. time curves for Panel #2b for different energies.

Panel #2b: The deflection vs. time responses for this panel, with poly-film hardening in both back and front faces, are shown in Fig. 5.23 for impact energies of I_2, $1.5I_2$ and $2I_2$. The corresponding impact velocities were 9330.13, 10773.51, and 12045.15 mm/sec, respectively. In comparison with deflection in Panel #2 for impact energy $2I_2$, the maximum deflection value reduced from 101.987 mm to 75.768 mm which is a 26% drop.

5.5.2 Local vs. Global Response

The overall response values in terms of equivalent plastic strain given by $\varepsilon_{eq}^{p} = \sqrt{\frac{2}{3}\sum_{i=1}^{3}\sum_{j=1}^{3} d\varepsilon_{ij}^{p} \cdot d\varepsilon_{ij}^{p}}$, where $d\varepsilon_{ij}^{p}$ is plastic strain increment, and corresponding equivalent stress values were examined at time instants 0.000342s, and 0.003017s, 0.020020s for impact energy of I_2 = 1767.8 J for Panels #1 and #2, $2I_2$ = 3575.2 J for Panels #2 and #2b, and $2.5I_2$ =4419.5 J for Panels #2 and #2b. For this purpose, the sectional views through the center of equivalent strain and stress fringes along the length and width of Plates 1 to 2b are shown in Figs. 5.24 to 5.28.

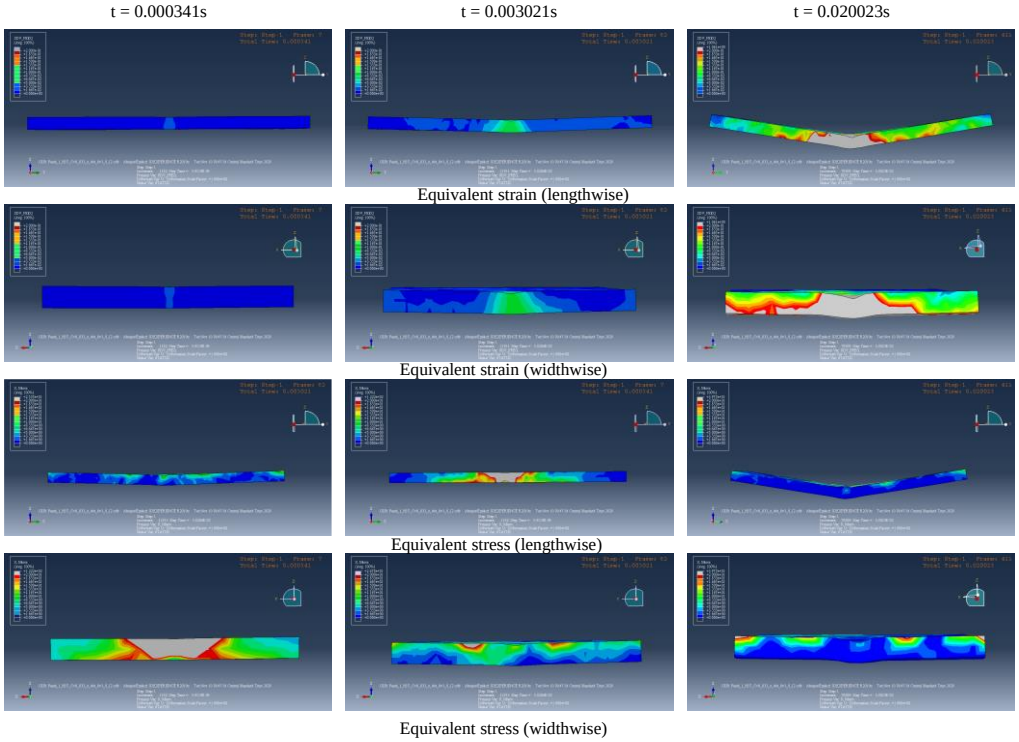

Figure 5.24. Panel #1 with impact energy I_2 = 1767.8 J.

In the case of Panel #1 (Fig. 5.24) at time instant 0.000341 s, the damage pattern is concentrated around the impact location and points away from it are almost strain free. At later times, the strain spreads globally till the time instant 0.02002 s, when most of the global damage has already occurred. The temporal transition from local to global damage is quite evident. Large residual strains in the stress free state are also evident. The damages are consistent with actual observations during tests, as the shock front radiated away from the impact area with interference from wave diffusions specially in the shorter direction from the boundaries in the longer direction. The existence of travelling shock front is clearly discernible from Fig. 5.24.

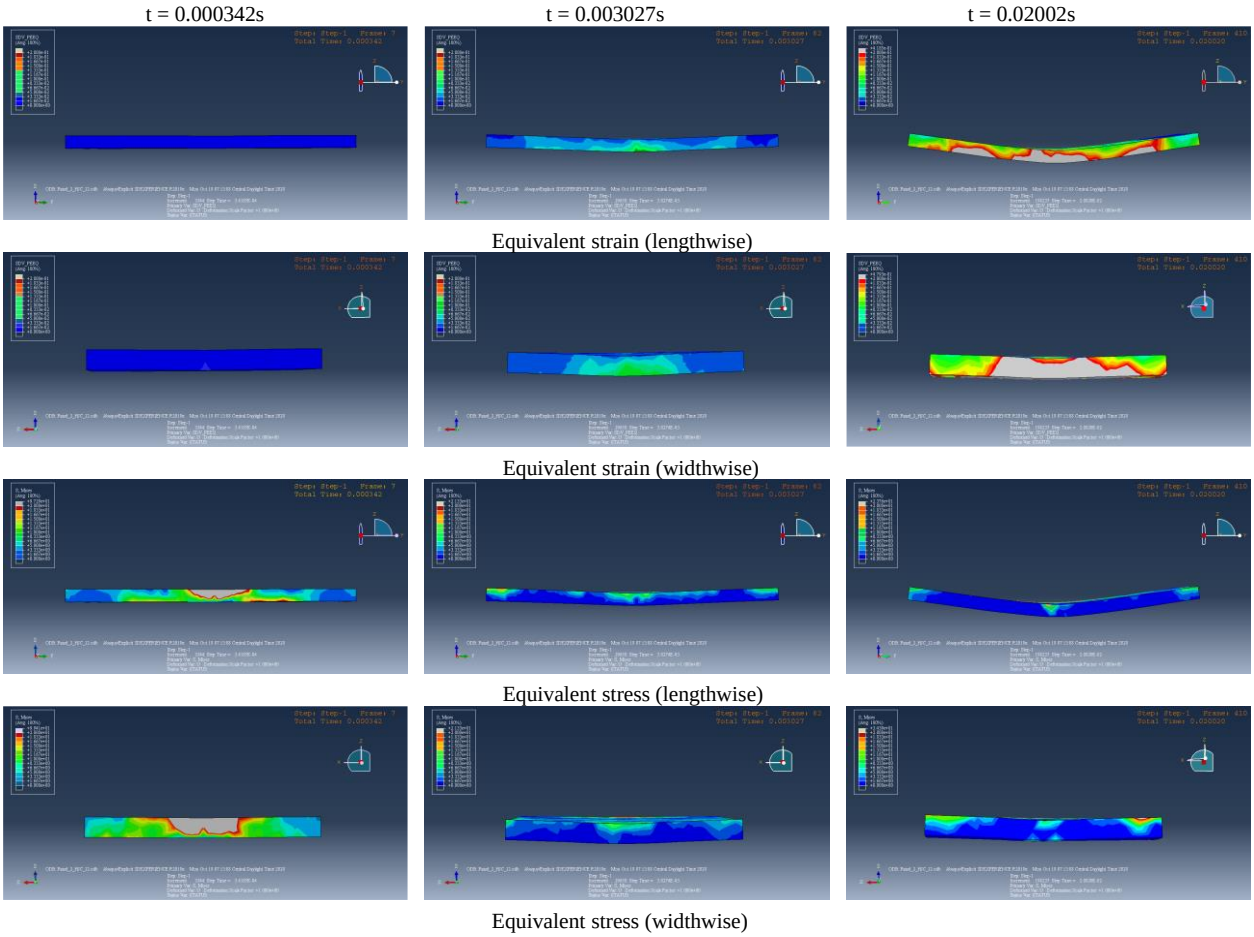

Figure 5.25. Panel #2 with impact energy of I_2 = 1767.8 J.

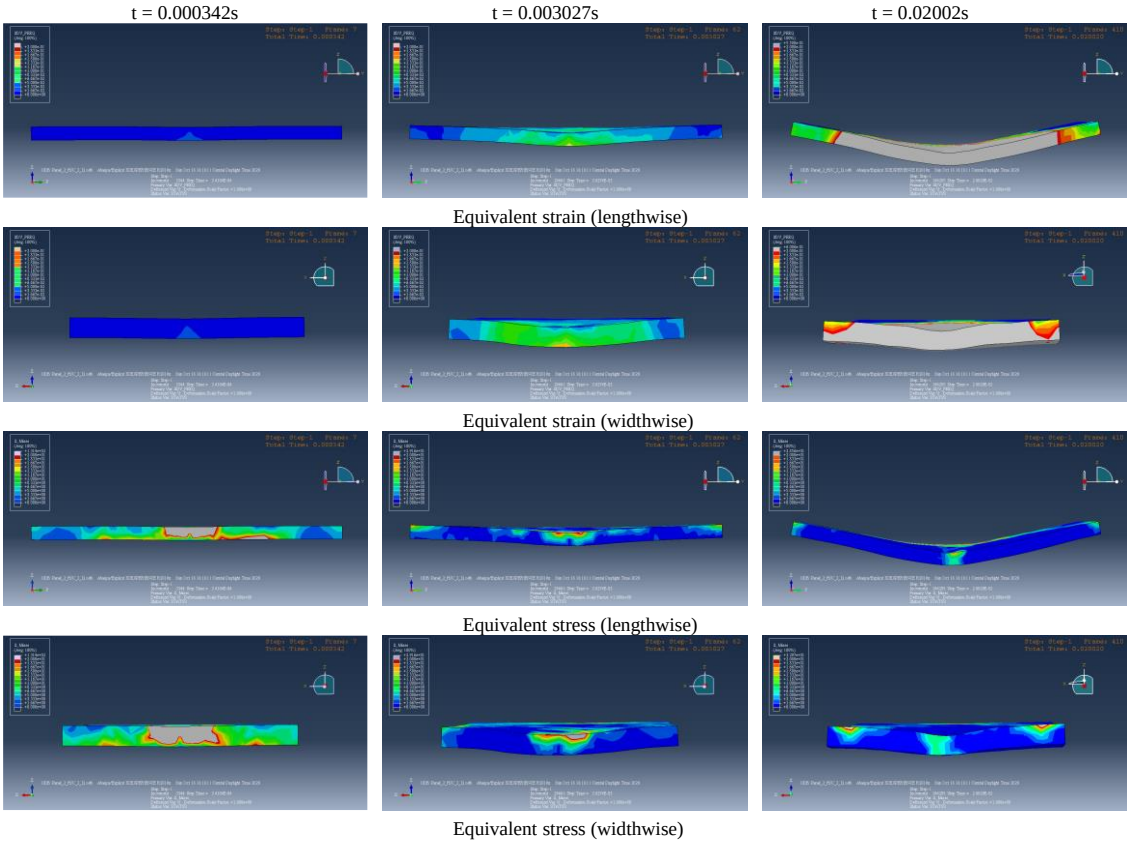

Figure 5.26. Panel #2 with impact energy of $2I_2$ = 3535.6 J.

In the case of Panel #2 (Fig. 5.25) the equivalent strain and stress fringes follow the expected pattern. A comparison of contour fringes of Panels #1 and #2 subjected to the same impact energy clearly shows superior performance of hardened Panel #2 over Panel #1 both in terms of reduced deformation and strain as well as stress levels. The difference in response when the bonded poly-film becomes effective after cracking of concrete is striking.

The advantages of applying poly-film in both the faces of the panel in the case of Panel #2b is evident from the fringe patterns shown in Figs. 26 to 28. As expected, under doubled impact energy, both Panels #2 and #2b show satisfactory performance. The overall superiority of the presence of poly-film in both the faces of panel is quite evident.

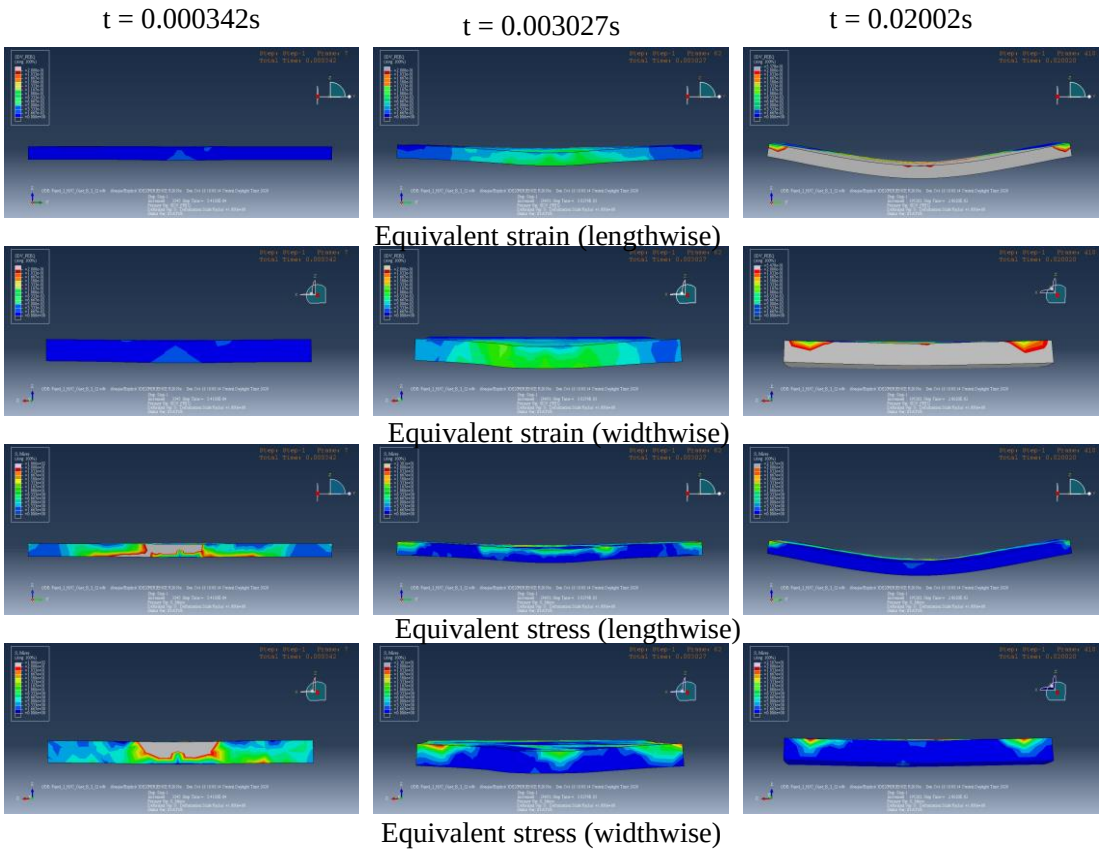

Figure 5.27. Panel #2b with impact energy of $2I_2$ = 3535.6 J.

In the case of Panel #2b (Fig. 5.28), the effect additional top layer of poly-film confirms the positive effect of such hardening even under the influence of higher impact energy. In short, the damage patterns in all cases were consistent with the level of hardening. Overall, the use of bonded polyethylene film showed significant improvement in performance with levels of impact load considered in the study.

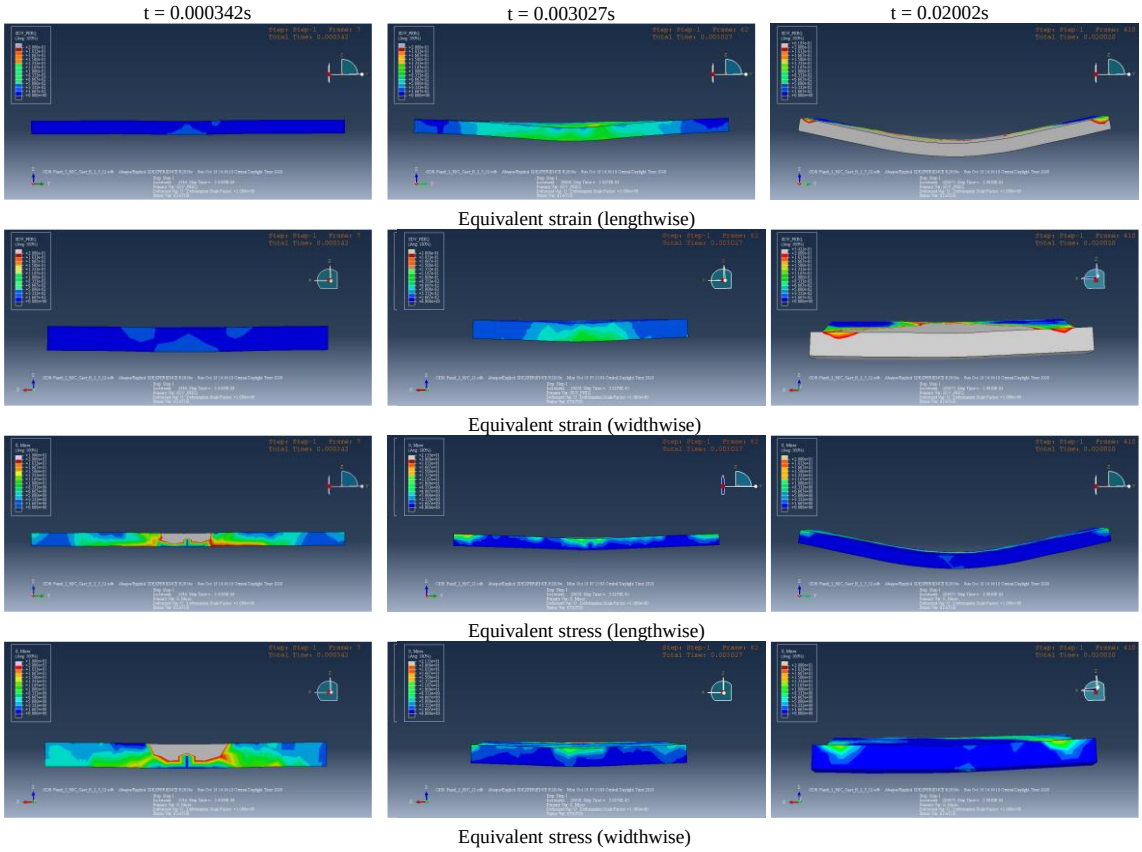

Figure 5.28. Panel #2b with impact energy of $2.5I_2$ = 4419.5 J.

5.5.3 Maximum Response Values

To deeply understand the behavior and performance of the panels subjected to different levels of impact energy, three critical reference points were selected as shown in Fig. 5.29. Point #1 is at the center of the panel (C.P.). Point #2 is on the long edge (L.E.P.) and point #3 is on the short edge of the panel (S.E.P.). Tables 5.5, 5.6 and 5.7 give the summary of the maximum values for each reference point located in the back side of concrete panels. The trend of change seems to be consisted with respect to both impact energy levels and degree of hardening.

Table 5.5. Summary of the maximum values of the center point (C.P.) of panels in all cases.

Panel #	Maximum Deflection (mm)				Max. Logarithmic Principal Strain				Equivalent stress (MPa)			
	Case 1	Case 2	Case 3	Case 4	Case 1	Case 2	Case 3	Case 4	Case 1	Case 2	Case 3	Case 4
1	54.800	76.003	94.322	95.542	0.1341	0.2310	0.2670	0.2907	3.634	5.315	4.332	3.988
2	62.006	61.771	80.592	99.236	0.1195	0.1226	0.1330	0.1878	9.036	8.996	10.958	6.825
2b	-	62.126	75.090	86.931	-	0.0536	0.0454	0.0399	-	8.869	29.737	30.655

Table 5.6. Summary of maximum values of the long edge point (L.E.P.) of panels in all cases.

Panel #	Maximum Deflection (mm)				Max. Logarithmic Principal Strain				Equivalent stress (MPa)			
	Case 1	Case 2	Case 3	Case 4	Case 1	Case 2	Case 3	Case 4	Case 1	Case 2	Case 3	Case 4
1	47.064	63.293	77.367	79.830	0.0258	0.1287	0.0754	0.0646	7.639	8.567	6.915	6.957
2	52.534	53.896	73.398	85.702	0.0229	0.0430	0.0660	0.0432	9.805	9.333	12.246	11.242
2b	-	57.407	68.443	79.392	-	0.0304	0.0448	0.0395	-	9.664	7.983	6.825

Table 5.7. Summary of maximum values of the short edge point (S.E.P.) of panels in all cases[†]

Panel #	Maximum Deflection (mm)				Max. Logarithmic Principal Strain				Equivalent stress (MPa)			
	Case 1	Case 2	Case 3	Case 4	Case 1	Case 2	Case 3	Case 4	Case 1	Case 2	Case 3	Case 4
1	8.205	10.605	13.450	13.612	0.0027	0.0019	0.0046	0.00398	5.886	6.836	6.104	4.960
2	11.348	11.449	16.233	19.314	0.0053	0.0081	0.0169	0.0129	10.385	7.970	11.081	14.526
2b	-	13.469	16.361	19.906	-	0.0207	0.0322	0.0423	-	10.471	12.167	12.939

†: Note that all deflection values in Table 5.6 with a negative sign signify that the short edge of the panel moves up.

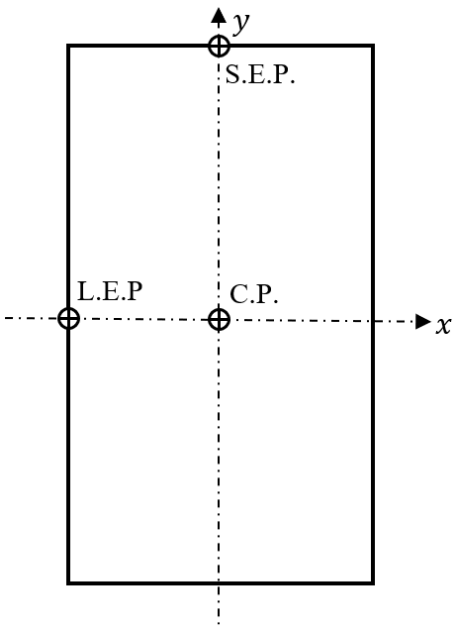

Figure 5.29. The selected critical points of the panels.

5.6 Summary

Results of numerical simulation reasonably followed the experimental data. As the experimental results refer to the impactor and the predictions refer to center of panel itself, at least partly, explains the noticeable discrepancy between the experimental data and simulation results. Also, HJC predictions show better agreement with test data than CDP predictions with the added advantage that HJC model is designed to allow for strain-rate effects. This prompted the use of HJC model in further studies, namely, the effect of higher impact energy than those used in laboratory tests. The temporal transition from local to global damage due to time lag between shock wave application and the appearance of strain at a point away from the point of impact is clearly demonstrated by the results presented in Section 5.5.2.

The simulation results of all the panels indicate that the polyethylene film is not damaged, which is corroborated by experimental findings as well. The maximum equivalent stress value predictions in the polyethylene film did not exceed the yield value of the film material, as determined by tensile testing of the material. The observed advantages of hardening with polyethylene film are as follows:

- Reduced the deflection of solid panel and those with glazed opening.

- In panels with glazed opening, bonding of poly-film to the impact face of glazing reduced the deflection by 8.60%.
- Effective in preventing back face concrete fragmentation associated with scabbing.
- Prevented flying and scattering of shattered glass fragments.
- Using poly-film with superior adhesive is expected to improve overall performance of the hardening measure.

CHAPTER 6

SUMMARY, CONCLUSIONS AND RECOMMENDATIONS

6.1 Summary

The primary objective of this research effort was to develop a modelling and simulation scheme for reinforced concrete cladding panels of a building, with glazed window opening and with no openings (i.e., solid), when exposed primarily to projectile impact. The developed method can also be applied to a blast loading scenario, with slight modification, utilizing the blast wave pressure profile given in Chapter 2. After a detailed review of the nature of impact and blast loadings as presented in Chapter 2, the scaled physical details of candidate panels were arrived at based on current practice as well as the limitations imposed by the available test facilities. Two types of panels were considered, namely, solid panels and the ones with glazed window openings. As per the typical practice in Saudi Arabia, panels anchored with corner supports only were opted for in this research. This choice enabled the consideration of structurally most critical support case. For post construction hardening of both types of panels, bonded polyethylene film was used. For validation purposes, apart from computer simulation of the projectile impact response, actual impact tests were undertaken on both types of panels, under both pre- and post-hardened conditions.

Before embarking upon the modeling and simulation process, mechanical properties of the used inventory of materials comprising of concrete, steel reinforcement, glass and polyethylene film were determined through extensive material testing, in conjunction with fabrication and testing of the fabricated panels in the Instron Drop Weight Impact Tester, as presented in Chapters 3, 4 and Appendix A.

Due to the non-accessibility of some material test equipment of required type and/or capacity, the author had to fill the gaps in the test data by making use of the empirical formulas and relevant test data available in the published literature. The pertinent details related to these were presented in Chapter 3, which covers considerations related to uniaxial and tri-axial compression behavior of concrete, damage processes in concrete, tensile behavior of concrete, and strain-rate effects in concrete for which a new Dynamic Increase Factor formula (Eq. 3.28) was proposed. In the same chapter, for given values of E_c and f_c', the proposed stress vs strain prediction

curve is given by Eq. (3.13) for the strain-hardening part, and Eq. (3.14) for the strain-softening part. The influence of confining effect on the compressive strength of concrete was investigated in detail and a set of response curves were produced for concrete used in this research, as shown Fig. 3.8, based on which the Equation of State for confined concrete was defined. Detailed considerations behind the definition of yield surface and flow rule of concrete were presented. The damage parameter *d* was based on the loss of strength of concrete in the softening segment of the uniaxial stress vs. strain curve of concrete. The influence of all the stated concrete behavior on the two models of concrete: Concrete Damage Plasticity (CDP) and Holmquist-Johnson-Cook (HJC), was presented as shown in Figs. 3.27 and 3.29. Calibration of model parameter based on material test data was undertaken using Dassault Systems software Isight. To allow for possible dislodging of broken pieces from a solid concrete panel during projectile impact reflecting cratering and scabbing processes, the need for Spherical Particle Hydrodynamics (SPH) was explained.

Furthermore, Chapter 3 dealt with material modeling considerations for steel rods, plate glass, and poly-film including strain-rate effects. The stated chapter also covers the necessary basics of failure models for all the materials considered in this research. This chapter also expounded on the evolution of various failure models for concrete and gives the basic details of two concrete damage models, namely, Concrete Damage Plasticity (CDP) and Holmquist-Johnson Cook-(HJC), used in this research. The differences between the two models were elaborated in detail.

According to Chapter 4, six test panels were fabricated, as per the details given in Fig. 4.2 and Tables 4.1 to 4.4. The scheme for using polyethylene film for hardening against impact loading is shown in Table 4.4. To control the nature of failure of the six test panels, applied impact energy was scaled appropriately to induce noticeable damage in concrete, avoiding any possibility of catastrophic failure. This was especially true in the case of two solid panels designated as Type 1, one with hardening and the other without, the latter acting as the reference panel. The response of the two panels were evaluated critically based on displacement response (Fig. 4.7), velocity response (Fig. 4.8), and damage patterns in the front and back faces of the panels, as shown in Figs. 4.9 and 4.11. Furthermore, a frame by frame examination of the high speed videos of the tests (Figs. 4.10 and 4.12) gave clear insight into the damage processes, as explained in the chapter. As expected, the hardened panel demonstrated a noticeable increase in impact resistance.

In the case of remaining four panels, one was tested without any hardening. As expected, this panel offered little resistance as the impactor mass hit the glazing at the center of the panel and shattered glass splinters flew all over. The failure process is evident from Figs. 4.13 and 4.14. In the case of the second panel of this series (namely, Panel #4 with hardening film applied to the back of glass panel) and tested with 46% higher impact energy than the unhardened case, a significant improvement in resistance was noticed. Although the glass pane showed cracks in it, but there were no flying glass splinters. The attached poly-film demonstrated some improvement in ductility and a noticeable increase in impact resistance. The progression and nature of damage in the panel are shown in Figs. 4.17 and 4.18. In the case of the third panel in the series (namely, Panel #5 with hardening film applied to the whole back face of the panel) the impact energy was almost the same as used for Panel #4 but exhibited further improvement in performance, showing higher stiffness. But in this case too, as expected, the glass pane shattered, again, but without flying splinters. In the case of the last panel in this series (namely, Panel #6 with hardening material applied to the whole back face as in Panel #5) and additional hardening material was applied in the front (or impact) face over the glazing area only. Although, in this case the impact energy was 50% higher than that used with Panel #5, the performance improved dramatically both with respect to stiffness and the extent of damage caused by impact. The impactor experienced multiple rebounds before coming to rest. The nature of response of this panel is evident from Figs. 4.21 and 4.22.

Response prediction based on finite element modeling and simulation of the six test panels was done using Abaqus, as described in Chapter 5. The CDP model is an option built into Abaqus. But in the case of HJC model, such option is not included and the complete model was defined through the input file. Additional simulations were undertaken to study the response characteristics with increasing impact energy for three solid panels, namely Panels 1, 2 and 2b. In the case of Panel #2b, the hardening film was applied to both the faces. A summary of the impact energies used in the second series of simulation are given in Table 5.1. Based on the processing and interpretation of material test results in Chapter 3, the input material parameters for the two models were defined. For instance, the parameter values for HJC model are shown in Table 5.2. In the finite element mesh, concrete was modeled mostly with 2 layers of C3D4 elements, poly-film with single layer of C3D4 elements, steels reinforcement with B31 wire elements, and glass pane with 2 layers of C3D4 elements. During the nonlinear finite element dynamic analyses, appropriate

choice of the time step was found to be of great significance to ensure faster convergence. This requires appropriate satisfaction of the Courant condition. According to this condition, the time step should be less than the ratio of the characteristic length of the smallest element used in the model and the velocity of wave propagation in the modeled material (namely, concrete).

The simulations were undertaken using calibrated material parameters, as described in Chapter 3. In the case of Panels #1 and #2, the predicted time-history of CDP and HJC displacements along with the experimental values are shown in Figs. 5.3 and 5.4. The correlation between HJC and CDP predictions was very good, even though strain-rate effect is not accounted for in Abaquse's CDP model; such effect at relatively low loading rates is negligible. The noticeable difference with the experimental values, except at the beginning and end of test was attributed to the use of different reference points in test (projectile) and simulation (center of panel). This also demonstrates definite separation between panel and projectile after impact. Another interesting observation with respect to the deflected shapes of panels as predicted by HJC and CDP (Figure 5.5), the panels underwent flexure, primarily, in the longer direction. In the case of time-history of velocity plots (Fig. 5.6), HJC predictions showed better correlation with the experimental data in the case of Panel #1. Panel #2 results show larger discrepancy during early stages and more experimentally relatable velocity values in the latter half of the simulation. The degree of damage in the panels was measured in terms of von Mises equivalent stress, as defined in Section 5.3.3 in terms of deviatoric stress tensor. The predicted damage patterns in the bottom face of the two panels are shown in Figs. 5.8 and 5.9 for Panel #1. A comparison with the back face damages of the panel, shows that the HJC predictions are closer to test values. The same was, also, found to be true in the case of Panel #2. In the case of polyethylene film, assumed to be ideally bonded, the maximum equivalent stress was 75% of its yield strength. But the observed response of Panel #2 during test showed delamination of film leading to the conclusion that the bonding agent used by the manufacturer of the film lacked enough adhesive strength.

In the case of Series 2 panels, the first panel (#3) underwent sudden brittle failure with displacement history plots by simulation and experiment showing (Fig. 5.15) reasonably good agreement. In the case of Panel #4 the predictions also agree well with the experiment. Similar results were noted in the case Panels #5 and #6 too. The predicted damage patterns in these four

cases were as expected. The main shortcoming was the delamination of bonded film in the case of Panels #4 and #5.

The results discussed so far, especially in the case of Panels #1 and #2, confirmed the superiority of the HJC model, possibly due to the inclusion of strain-rate effect. So, during the follow up parametric studies were undertaken with series 1 panels, HJC model was chosen for all three panel types, described in Chapter 4. The results of four simulations (as time-history of displacement) in each case are presented in Figs. 5.22 to 5.24. In all the cases panel performance after hardening (Panel #2) significantly improved the impact resistance in comparison with the unhardened panel.

For a clear understanding of local vs global response of Series 1 panels, the time history response of the three panels subjected to increasing impact energy were critically examined step by step in the time domain. In the case of Panel #1, the fringe plots for equivalent strain and stress over midspan sections along the length and width of the panel at different instants of time were considered, as shown in Fig. 5.26 for impact energy of 1767.8 J. The process of local initiation of damage at the impact point as well as its global spread over time due to the propagation of shock wave was clearly demonstrated. Similar fringe plots in the case of the other two panels (hardened in one and both sides) subjected to two different levels of impact energy in each case are shown in Figs. 5.26 to 5.29.

6.2 Conclusions

1. Hardening of concrete cladding panels for buildings against impact loads using surface bonded polyethylene films has proven to be effective but for better performance, the use of films with stronger adhesive agent than what is available commercially is expected to improve the performance.

2. Predictions based on finite element simulation were found to have reasonable correlation with test results. The differences can be attributed to the different choice of reference points. In the case of panel, it was the geometric center of the panel, and in the case of testing machine, it was bottom of the impacting mass.

3. Although the impact tests were undertaken at relatively low impact velocities resulting from limitation imposed by the impact test equipment, predictions of computer simulation with significantly higher velocities confirmed the effectiveness of the hardening measure.

4. In the case of glazed panels with no hardening measures, the failure was catastrophic, but the performance improved as hardening measures were undertaken. However, the resistance of the concrete part of the panel hardly came into play. The use of ordinary plate glass cannot be relied upon for full-proof impact resistance even after hardening measures are taken. The use of special impact resistant glass is advised for panels with glazed openings.

5. Of the two concrete models used in the simulation, HJC was found to be superior to CDP, partly because the Abaqus implementation of the latter model could not account for strain- rate effects as well as the confining effect of concrete (normally incorporated as the equation of state).

6. The stress vs strain information used in the material model can be appropriately defined using Equations (3.13) and (3.14) arrived at in this research effort.

7. In the case of HJC, the recommended parameter used in the strain-rate effect equation for concrete was found to be erroneous and proposed more accurate equations for same was developed as part of this research effort led to new Dynamic Increase Factor due to strain-rate defined by Equation 3.28.

8. The effect of rate of strain propagation appears as local damage phenomenon just after impact and the resulting Love waves spread out towards the supports causing damages of lesser degree except near the corner supports, as evidenced by the parametric response of panels shown in Figs. 5.25 to 5.30 as well as by the maximum response quantities at three critical locations, as presented in Tables 5.5 to 5.7.

9. Dassault Systems optimization software ‘Isight’ accessible from Abaqus was found to be an effective tool for calibrating concrete model parameters.

10. Element deletion capability of Abaqus worked smoothly both in the case of concrete and glass.

11. For quicker convergence of predictions, appropriate choice of time-step consistent with the limitation posed by the Courant Condition was found to be useful.

12. Each Abaqus simulation required a significant amount of CPU time, sometimes, involving many hours. Measures to reduce it are necessary by optimum choice of the finite element model is a desirable goal.

13. The application of principles of similitude to define the test model was found to be very useful in creating a test model which is an accurate representative of the prototype.

6.3 Recommendations

- As the Instron drop Weight Impact Tester used was found to be inadequate for the present research, a higher powered tester which allowed significantly higher impact energy as well as more detailed data acquisition is recommended for use in future work. Alternatively, the size of the test panels could be scaled down further. But it will cause fabrication problems.
    - Use of hardening films with higher adhesive resistance is recommended.
- Studying the effect of non-central and multiple projectile impact is important. In addition, the effect of different projectile geometry may be investigated.
- Prediction of the blast response of the panels based on CONWEP formulas as well as dynamic fluid simulation accounting for the source of blast is desirable.
- Studying the effect of self-powered projectiles delivered, say, by drones (UAV) is gaining importance and hence the need for developing mitigation measures may assume importance soon.
- Studying the performance high-performance concrete panels is desirable to further improve impact and/or blast resistance.
- Optimization of the finite element model using suitably graded mesh with refined mesh in the impact zone and progressively larger elements away from it, unlike what was done in the present research using a uniform mesh of small elements.

APPENDIX A: DETAILS OF MATERIAL TESTING

A1. Modulus of Elasticity and Poisson's Ratio of Concrete: For this purpose, dry test cylinders were mounted with Vishay longitudinal and transverse strain-gages meant for concrete, as shown in Fig. A1, following standard procedures. The unconfined compression test was undertaken on a 60k Tinius Olsen Universal Testing machine in conformity with ASTM Standards. The typical stress vs. strain of concrete obtained by the test is shown in Fig. A2. The average value of elastic modulus (E_c) obtained was 30,000 MPa. Also, the average value of Poisson's ratio was found to be 0.15.

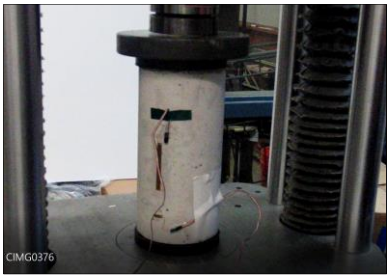

Figure A1. Measurement of stress vs. strain response concrete.

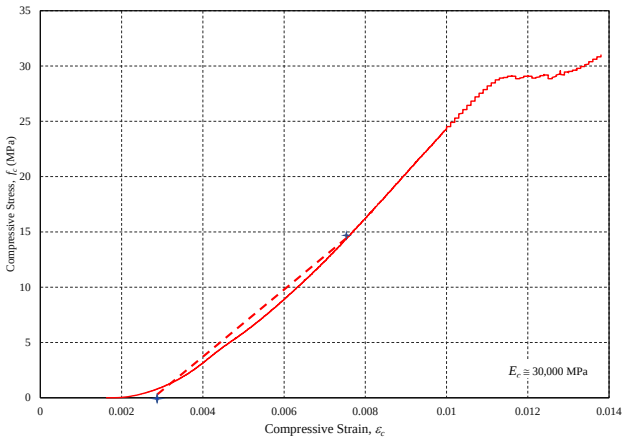

Figure A2. Initial part of uniaxial stress vs strain curve of concrete used in this study.

A2. Unconfined Compressive Strength of Concrete: 4" × 8" concrete cylinders were tested in axial compression as per ASTM C496/C496M-17 in a 400k capacity Forney compression testing machine till crushing failure, Fig. A3. 14-day Test results are shown in Table 4.2.

Figure A3. Unconfined compressive strength testing of concrete.

A3. Tensile Strength of Concrete: To determine the tensile strength of concrete Brazilian split-cylinder test was used as per ASTM C496/C496M-17. The 60k Tinius Olsen UT machine used. View of the 4" ×8" cylindrical concrete specimen at the beginning of test is shown in Fig. A4(a). The view of the same test after the specimen split into two halves is shown in Fig. A4(b). The minimum failure stress, $f_{split} = 2P_{split} / [\pi \times \textit{failure-surface-area}]$, was found to be equal to 3.71MPa. The direct tensile strength of concrete ($f_t^{'}$) has been found to be close to 90% of f_{split} giving the value of 3.34MPa.

(a) (b)

Figure A4. Split-cylinder tensile strength test of concrete with 60 k Tinius Olson UT Machine.

A4. Tensile Strength of Steel Reinforcing Rods: The same UT machine was used for this purpose. The test conformed with ASTM A370-17a. The typical stress vs. strain curve obtained

from the test is shown in Fig. 3.11. Figs. A5(a) and A5(b) show the test specimen before and after failure.

(a) (b)

Figure A5. Tensile test of reinforcing steel using UT Machine.

A5. Flexural Strength Test of Plate Glass: The mechanical properties of 13.54 mm thick using 39.4 mm wide single-layer normal glaze glass strips over 203.2 mm effective span was obtained by undertaking four-point bending quasi-static load test on the Tinius-Olsen UT machine. A view of the test is shown in Fig. A6. The average values of associated mechanical properties are shown in Table A1. The typical extreme load vs. deflection curve is shown in Fig. A7. The fracture strain for glass was found to be 1.526E-4.

Figure A6. Four-point flexure testing of glass strip using Tinius-Olson UTM.

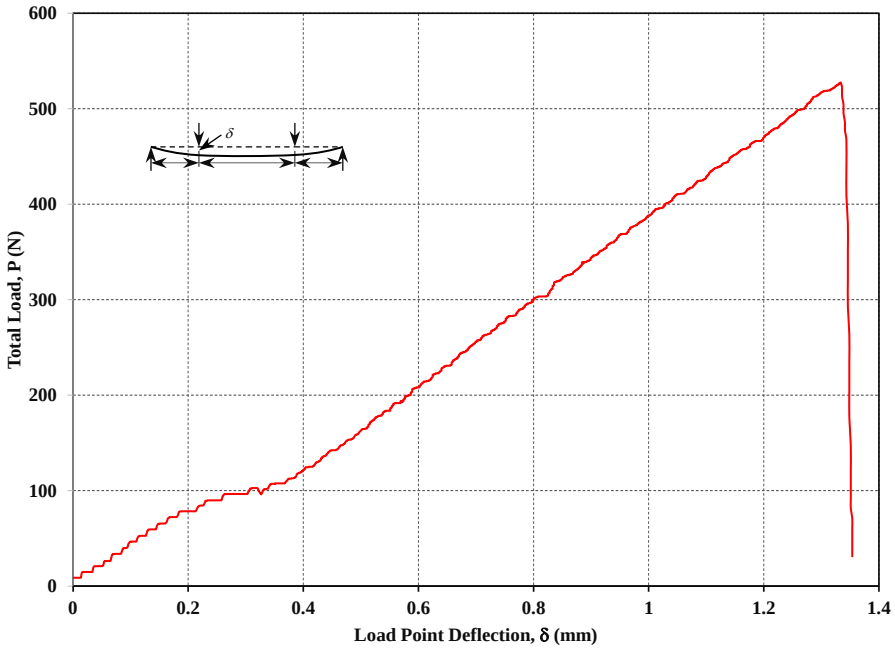

Figure A7. Experimental load vs. deflection curve for plate glass.

Table A1. Properties of glass used in numerical simulation.

Thickness (mm)	Density (kg/m^3)	Elastic Modulus (GPa)	Breaking Strength (MPa)	Poisson's Ratio	Shear Modulus (GPa)	Fracture Strain (mm/mm)
13.54	2.2	72.90	22.244	0.165	31.3	0.0525

A6. Tensile Strength of Polyethylene Film: The quasi-static tensile strength using a Instron 5944 testing machine belonging to the Mechanical Engineering Department. Two views of the test before and after fracture are shown in Fig. A7. The resulting typical stress vs strain curve is shown in Fig. A8. The initial part of the curve shows elastic behavior. At around 91MPa, it shows linear strain-hardening behavior till fracture occurs at a stress 114.7MPa at a large strain 0f 2.875.

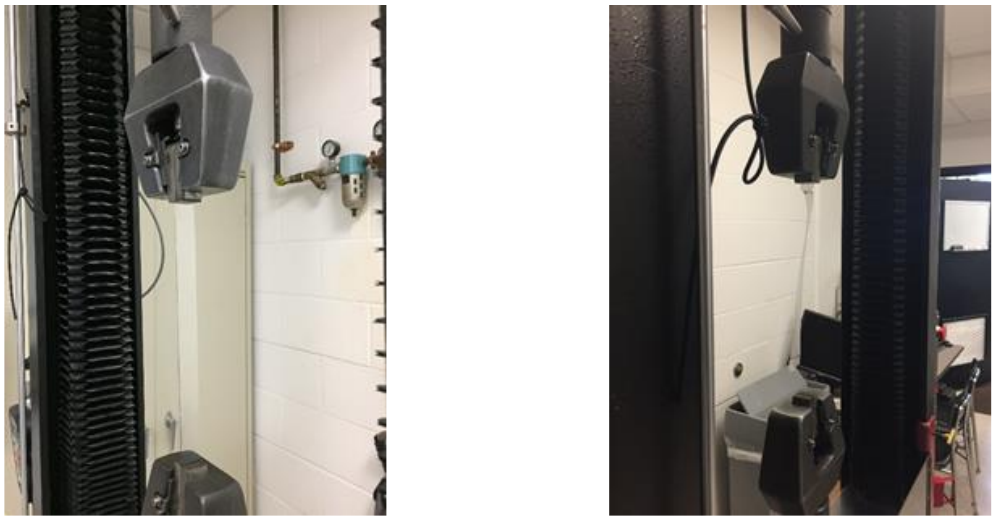

(a) Before failure (b) After failure

Figure A8. Tensile strength testing of polyethylene film.

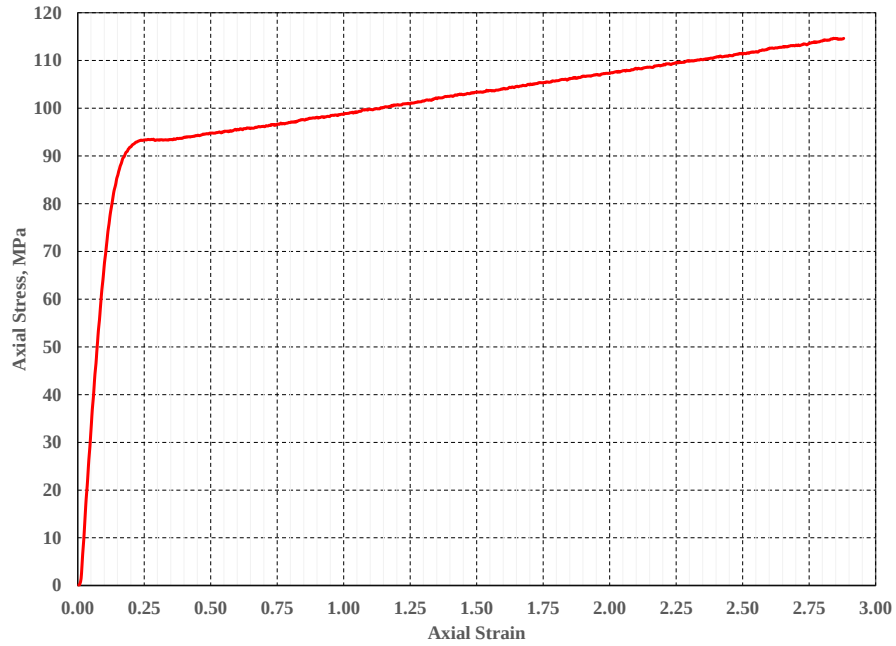

Figure A9. Experimental stress vs. strain curve for 12 mil thick polyethylene film.

Table A2. Properties of high-density polyethylene used in numerical simulations.

Density (kg/m^3)	Thickness (mm)	Peak Stress (MPa)	Break Stress (MPa)	Shear Strength (MPa)	Elastic Modulus (MPa)	Poisson's Ratio	Break strain (mm/mm)
1.5255	0.3048	114.7	109.007	1.542	853.184	0.3	2.955

A7. Strain Gage Installation: Strain gages were affixed to the test panels at locations shown in Figs. For measuring strains, Micro-Measurements self-temperature compensated strain gage locations for Panel #2 are shown in Fig. A9(a) and those for Panels #3 to #6 are shown in Fig. A9(b). Strain gage locations and relevant details of same are given in Table A.1. The strain gages were installed following standard procedures. Three Wheatstone quarter bridge circuits were fabricated to measure the strains.

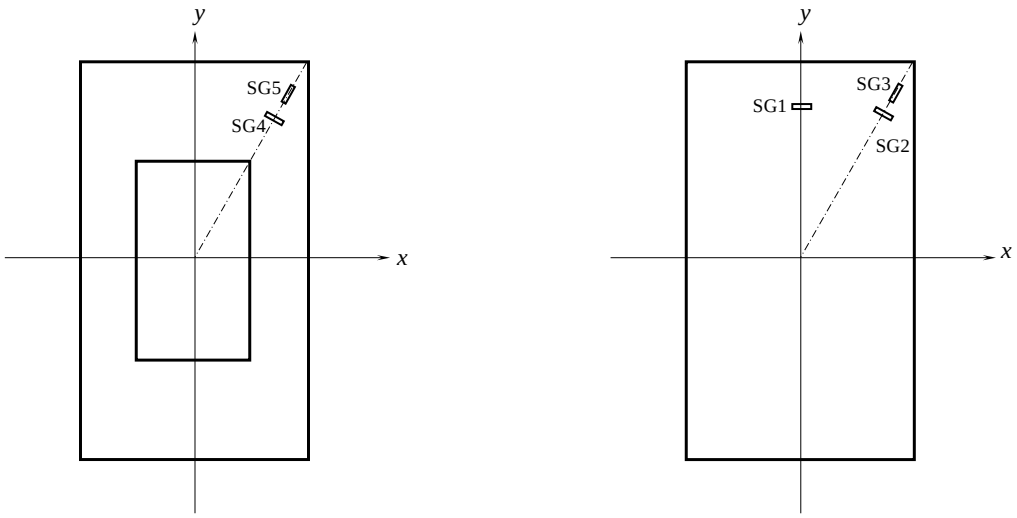

(a) Panel #2 (b) Panels #3 to #6

Figure A10. Strain gage locations.

Table A3. Details of strain gages (in Fig. A9).

Designation	Coordinates		Type	Resistance	Gage Factor
	x	*y*			
SG1	0.00	16.75"	C2A-06-20CLW-120	120Ω	2.14
SG2	9.18"	18.80"	C2A-06-20CLW-120	120Ω	2.14
SG3	10.10"	20.30"	C2A-13-50LW-120	120Ω	2.1
SG4	9.18"	18.80"	C2A-06-20CLW-120	120Ω	2.14
SG5	10.10"	20.30"	C2A-13-50LW-120	120Ω	2.1

A8. Specifications of Instron Drop Weight Impact Tester: Pertinent specifications of the impact tester are shown in Table A4.

Table A4. Drop weight impact testing machine specifications [111].

Item	Specification	Unit
Range of Impact Energy	0.59 - 1800	Joule
	0.44 - 1330	ft-lb
Range of Impact Velocity	0.77 - 24	m/s
	2.53 - 78.70	ft/s
Equivalent Free Drop Height	0.03 - 29.40	m
	1.18 - 11.60	in
Mass Range	2.00 - 70.00	kg
	4.41 - 154	lb
Mass Increment	0.5	kg
	1.1	lb
Dimensions of Test Area (w×d×h)	700×720×550	mm
	27.5×28.3×21.6	in

REFERENCES

[1] Canadian Precast/Prestressed Concrete Institute, “Architectural Precast Concrete Walls, Best Practice Guide,” 2017.

[2] PCI Design Handbook, “Blast-resistant design of precast, prestressed concrete components,” Appendix A, Edition 8, 2014.

[3] Interagency Security Committee, “Physical Security Criteria for Federal Facilities,” (for official use only). Washington, DC: Department of Homeland Security, 2010.

[4] U.S. Department of Defense, “Design and Analysis of Hardened Structures to Conventional Weapons Effects,” UFC 3-340-01. Washington, DC: U.S. Department of Defense, 2002.

[5] U.S. Department of Defense, 2012, “Structures to Resist the Effects of Accidental Explosions,” UFC 3-340-02. Washington, DC: U.S. Department of Defense.

[6] U.S. Department of Defense, “DoD Minimum Antiterrorism Standards for Buildings,” UFC 4-010-01. Washington, DC: U.S. Department of Defense, 2012.

[7] USACE (U.S. Army Corps of Engineers), “Single Degree of Freedom Structural Response Limits for Antiterrorism,” Protective design center technical report - PDC-TR 06-08, Washington, DC: USACE, 2006.

[8] ASCE (American Society of Civil Engineers), “Design of Blast Resistant Buildings in Petrochemical Facilities,” Reston, VA: ASCE, 2010.

[9] Zukas, A., *Introduction to Hydrocodes*, Studies in Applied Mechanics, Elsevier, 2004.

[10] NDRC, “Effects of Impact and Explosion,” Summary of Technical Report of the National Defense Research Committee, Washington, D.C., 1946.

[11] Rahman, M., and Barber, J.R., “Exact expressions for the roots of the specular equation for Rayleigh waves,” ASME J. Appl. Mechanics, Vol. 62, pp. 250–252, 1995.

[12] Davidson, L., *Fundamentals of Shock Wave Propagation in Solids*, Springer, 1978.

[13] Bedford, A., and Drumheller, D.S., *Introduction to Elastic Wave Propagation*, John Wiley, 1994.

[14] Basu, P.K., “Development of a Simplified Blast Design Procedure and Response Limits for Load-Bearing Precast Wall Panels Subjected to Blast Loads,” 2013.

[15] Basu, P.K., “CEE 307 Class Notes,” 2014.

[16] FEMA, “Primer for Design of Commercial Building to Mitigate Terrorist Attacks,” FEMA 427, 2003.

[17] Ngo, T., Mendis, P., Gupta, A. and Ramsey, J., “Blast Loading and Blast Effects on Structures – An Overview,” Electronic Journal of Structural Engineering, Special Issue, pp.76–91, 2007.

[18] Dewey, J.M., “The Friedlander Equations,” Blast Effects, Springer, pp. 37–55, 2017.

[19] Krauthammer, T., *Modern Protective Structures*, CRC Press, 2008.

[20] Mills, C.A., “The Design of Concrete Structure to Resist Explosions and Weapon Effects,” Proceedings of the 1st Int. Conference on Concrete for Hazard Protections, Edinburgh, UK, pp. 61–73, 1987.

[21] Tedesco, J.W., McDougall, W.G., and Ross, C.A., *Structural Dynamics – Theory and Applications*, Addison-Wesley, 1999.

[22] US Army Fundamentals of Protective Design (Non-nuclear) (1965) “US Army Fundamentals of Protective Design (Non-nuclear),” Department of Army Technical Manual TM5-855-1, Washington, 1965.

[23] Department of Defense, “Structures to Resist the Effects of Accidental Explosions, Army TN 5-1300, Navy NAVFAC P-397, Air Force AFR-88-22,” Department of Defense, 1990.

[24] U.S. Army Corps of Engineer, “Single Degree of Freedom Structural Response Limits for Antiterrorism Design,” Protective Design Center Technical Report 06-08, 2008.

[25] USACE-ERDC, “Fundamentals of Protective Design for Conventional Weapons,” TM 5-855-1.

[26] Hyde, D.W., “Users Guide for Microcomputer Program – CONWEP: Application of TM 5-885-1,” Fundamentals of Protective Design for Conventional Weapons, Instructional Report SL-88-1, 1992.

[27] Swisdak, M.M., and Ward, J.M., “The DDESB Blasts Effect Computer – Version 3.0,” PARAPI 99 Australian Safety Seminar, Nov. 1999.

[28] Department of Defense, “DoD Minimum Antiterrorism Standards for Buildings,” UFC 4-1010-02, 2012.

[29] ASCE, “Blast Protection of Building,” ASCE Standard ASCE/SEI 59-11, 2011.

[30] ASTM C39/C39M-21, “Standard Test Method for Compressive Strength of Cylindrical Concrete Specimens,” 2021.

[31] ASTM C469/C469M-14e1, “Standard Test Method for Static Modulus of Elasticity and Poisson's Ratio of Concrete in Compression,” 2014.

[32] ASTM C496/C496M-17, “Standard Test Method for Splitting Tensile Strength of Cylindrical Concrete Specimens,” 2017.

[33] *Kolsky, H., “An Investigation of the Mechanical Properties of Materials at Very High Rates of Loading,” Proc. Phys. Soc. B, Vol. 62, No. 11, p. 676, 1949.*

[34] Chen, W.F., *Plasticity in Reinforced Concrete,* McGraw-Hill, 1982.

[35] Drucker, D.C. (1949) “Relations of Experiments to Mathematical Theories of Plasticity,” J. Appl. Mech., Vol. 16, pp. 349–357.

[36] ABAQUS, “Abaqus Analysis User's Manual, Version 6.9,” Dassault Systems, 2009.

[37] Hognestad, E., Hanson, N.W., and McHenry, D., “Concrete Stress Distribution in Ultimate Strength Design,” ACI Jl. Proc., Vol. 52, No. 12, pp. 455–479, 1955.

[38] Yip, W.K., “Generic Form for Stress-Equations for Concrete,” Cement Concrete Res., Vol. 28, No. 4, pp. 499–508, 1998.

[39] Desayi, P., and Krishnan, S., “Equation for the Stress-Strain Curve of Concrete,” ACI Jl., pp. 345-350, March 1964.

[40] Tulin, L.G., and Gerstle, K.H., “Stress-Strain Relations for Concrete Under Cyclic Loading,” ACI Jl., 61, 1236 (1964).

[41] Popovics, S., “A Numerical Approach to The Complete Stress-Strain Curve of Concrete,” Cement Concrete Res., Vol. 3, pp. 583–599, 1973.

[42] Richart, F.E., Brandtzaeg, A, and Brown R.L., “A Study of the Failure of Concrete Under Combined Compressive Stresses,” Bulletin No. 185, Engineering Experimental Station, University of Illinois, Champaign, Illinois, 1928.

[43] Gardner, N., “Triaxial Behavior of Concrete”, ACI Jl., 1969.

[44] Li, Q., and Ansari, F., “High-strength concrete in triaxial compression by different sizes of specimens,” ACI Materials Jl., 97, 2000.

[45] Nordendale, N.A., “Modeling and Simulation of Brittle Armors Under Impact and Blast Effects,” Ph.D. Dissertation, Vanderbilt University, 2013.

[46] Hammons, M.L., and Neeley, B.D., “Triaxial Characterization of High-Strength Portland Cement Concrete,” Transportation Research Record 1382, pp. 73–77.

[47] Heard, W.F., “Development and Multi-Scale Characterization of a Self-Consolidating High-Strength Concrete for Quasi-Static Load and Transient Load,” Ph.D. Dissertation, Vanderbilt University, 2014.

[48] Ahmad, S.H., and Shah, S.P., “Complete Triaxial Stress–Strain Curves for Concrete,” J. Struct. Div., Vol. 108, No. 4, pp. 728–742, 1982.

[49] Sfer, D., Gettu R., and Etse G., “Study of the Behavior of Concrete Under Triaxial Compression,” J. Eng. Mech., pp. 128–156, 2002.

[50] Mills, L.L., and Zimmerman, R.M., “Compressive Strength of Plain Concrete Under Multiaxial Loading Conditions,” ACI J. Proc., Vol. 67, No. 10, pp. 802–807, 1970.

[51] Attard, M.M., and Setunge, S., “Stress–Strain Relationship of Confined and Unconfined Concrete,” ACI Mater. J., Vol. 93, No. 5, pp. 432–442, 1996.

[52] Hammons, M.L., and Neeley, B.D., “Triaxial Characterization of High-Strength Portland Cement Concrete,” Transportation Research Record 1382, pp. 73–77.

[53] Binici, B., “An Analytical Model for Stress–Strain Behavior of Confined Concrete,” Eng. Struct., Vol. 27, No. 7, pp. 1040–1051, 2005.

[54] Lim, J.C., and Ozbakkaloglu, T., “Stress–Strain Model for Normal- and Light-Weight Concretes Under Uniaxial and Triaxial Compression,” Constr. Build. Mater., Elsevier, 71, pp. 492–509, 2014.

[55] Holmquist, T.J., Johnson, G.R., and Cook, W.H., "A Computational Constitutive Model for Concrete Subjected to Large Strains, High Strain Rates, and High Pressures," Proceedings of the Fourteenth International Symposium on Ballistics, Quebec City, Canada, 1993.

[56] Roy, D.M., Brown, P.W., Shi, D., Scheetz, B.F., and May, W., "Concrete Microstructure – Porosity and Permeability," Report: SHRP-C-628, National Research Council, 1993.

[57] Wang T., and Hsu T.T.C., "Nonlinear Finite Element Analysis of Concrete Structures Using New Constitutive Models," Computers and Structures, Vol. 79, No. 32, pp. 2781–2791, 2001.

[58] Carreira, D.J., and Chu, K-H, "Stress-Strain Relationship for Reinforced Concrete in Tension," ACI J., pp. 21–28, January–February 1986.

[59] Bertero, V.V., Rea, D., Mahin, S., and Atalay, M.B., "Rate of loading effects on uncracked and repaired reinforced concrete members," Proceedings of 5th World Conference on Earthquake Engineering, Rome, pp. 1461–1470, 1973.

[60] Kulkarni, S. M. and Shah, S. P., "Response of Reinforced Concrete Beams at High Strain Rates," ACI Struct. J., Vol. 95, No. 6, pp. 705–715, 1998.

[61] Tedesco, J.W., Ross, C.A., McGill, P.B. and O'Neil, B.P., "Numerical Analysis of High Strain-Rate Concrete Direct Tension Tests," Computers and Structures, Vol. 40, No., 2, pp. 313–327, 1991.

[62] Heard, W.F., Nie, X., Basu, P., Martin, B.E., and Slawson, T., "Annular Pulse Shaping Technique for Large-Diameter Kolsky Bar Experiments on Concrete," Exp. Mech., Vol. 54, No. 8, pp. 1343–1354, October 2014.

[63] Gebbeken, N., and Greulich, S., "A New Material Model for SFRC Under High Dynamic Loadings," Proceedings of the 11th International Symposium on Interaction of the Effects of Munitions with Structures (ISIEMS), Mannheim, Germany, 2003.

[64] CEB., "CEB-FIP Model Code 1990," Trowbridge, Wilshire, UK, Committee Euro-International Du Beton, Redwood Books, 1993.

[65] Tedesco, J.W., and Ross, C.A., “Strain-Rate-Dependent Constitutive Equations for Concrete”, J. Press. Vess-T. ASME, Vol. 120, pp. 398–405, 1998.

[66] Yamaguchi, H., Fujimoto, K., and Nomura, S., “Stress Strain Relationship for Concrete Under High Tri-Axial Compression, Part 2 – Rapid Loading,” Trans Architectural Institute of Japan, 396, pp. 50–59, 1989.

[67] Malver, L.J., and Ross, C.A., “Review of Strain Rate Effects for Concrete in Tension,” ACI Mater. J., Vol. 95, No. 6, pp. 735–739, 1998.

[68] Grote, D.L., S.W. Park, and M. Zhou, “Dynamic Behavior of Concrete at High Strain-Rates and Pressures: I. Experimental Characterization,” Int. J. Impact Eng., Vol. 25, pp. 869–886, 2001.

[69] Fujikake, K., Li, B., and Soeun, S., “Impact Response of Reinforced Concrete Beam and its Analytical Evaluation”, J. Struct. Eng., ASCE, No. 28, pp. 938–950, 2009

[70] Lu, Y.B., and Li, Q.M., “About the Dynamic Uniaxial Tensile Strength of Concrete-Like Materials,” Int. J. Impact Eng., Vol. 38, pp. 171–180, 2011.

[71] Li Q.M., and Meng, H., “About the Dynamic Strength Enhancement of Concrete-Like Materials in a Split Hopkinson Pressure Bar Test,” Int. J. Solids Struct., Vol. 40, pp. 343–360, 2003.

[72] Hao, Y., Hao, H., and Li, Z.X., “Numerical Analysis of Lateral Inertial Confinement Effects on Impact Test of Concrete Compressive Material Properties,” Int. J. Protective Structures, Vol. 1, pp. 145–168, 2010.

[73] ASTM, “Standard Specification for Deformed and Plain Carbon-Steel Bars for Concrete Reinforcement,” ASTM A615/A615M, 2018.

[74] Rao, N.R.N., Lohrmann, M., and Tall, L., “Effect of Strain Rate on the Yield Stress of Structural Steels,” Fritz Laboratory Report No. 249.23, Lehigh University, September, 1964.

[75] Limbach, R., Rodrigues, B.P., and Wondraczek, L., “Strain-Rate Sensitivity of Glasses,” J. Non-Cryst. Solids, Vol. 404, pp. 124–134, 2014.

[76] Nie,X., Chen, W., Wereszczak, A.A., and Templeton, D., “Effect of Loading Rate and Surface Conditions on the Flexural Strength of Borosilicate Glass,” J. Am. Ceram. Soc., Vol. 92, No. 6, pp. 1287–1295, 2009.

[77] Holmquist, T.J., and Johnson, G.R., “A Computational Constitutive Model for Glass Subjected to Large Strains, High Strain Rates and High Pressures,” J. Appl. Mech., Vol. 8, No. 9, pp. 051003-1 to 9, 2011.

[78] Al-Maliky, N., and Parry, D.J., “Measurement of High Strain Rate Properties of Polymers Using an Expanding Ring Method,” J. Phys. IV Colloque, Vol. 04 (C8), pp. C8-71–76, 1994.

[79] Dong, W., Wu, Z., Zhou, X., and Huang, H., “Experimental Study of Biaxial-to-Uniaxial Compressive Strength Ratio of Concrete at Early Ages,” Constr. Build. Mater., Vol. 126, pp. 263–273, 2016.

[80] Lubliner, J., Oliver, J., Oller, S., and Onate, E., “A Plastic-Damage Model for Concrete,” Int. J. Solids Struct., Vol. 25, pp. 299–329, 1989.

[81] Lee, J., and Fenves, G.L., “Plastic-Damage Model for Cyclic Loading of Concrete Structures,” J. Eng. Mech., Vol. 24, No. 8, pp. 892–900, 1998.

[82] Holmquist, T. J., Johnson, G. R., and Cook, W. H., “A Computational Constitutive Model for Concrete Subjected to Large Strains, High Strain Rates, and High Pressures,” Proc. 14th International Symposium on Ballistics, Quebec, Canada, pp. 591–600, September 1993.

[83] Johnson, G.R., Holmquist, T.J., and Beissel, S.R., “Response of Aluminum Nitride (Including a Phase Change) to Large Strains, High Strain Rates and High Pressures,” J. Appl. Phys., Vol. 94, pp. 1639–1646, 2004.

[84] Majewski, S., “The Mechanics of Structural Concrete in Terms of Elasto-Plasticity,” Silesian Polytechnic Publishing House, Gliwice, 2003.

[85] Liu, F., and Li, Q.M., “Strain-Rate Effect on the Compressive Strength of Brittle Materials and its Implementation into Material Strength Model,” Int. J. Impact Eng., Vol. 130, pp. 113–123, 2019.

[86] Velden, A., and Koch, P., “Isight Design Optimization Methodologies,” Simulia - Dassault Systems, 2010.

[87] Hanchak, S.J., Forrestal, M.J., Young, E.R., and Ehrgott, J.Q., “Perforation of Concrete Slabs with 48 MPa (7 ksi) and 140 MPa (20 ksi) Uncompressive Strength,” Int. J. Impact Eng., Vol. 12, No. 1, pp. 1–7, 1992.

[88] Riedel, W., Thomas, K., Hiermaier, S., and Schimolinske, E., “Penetration of Reinforced Concrete by BETA-B-500 Numerical Analysis Using a New Macroscopic Concrete Model of Hydrocodes,” Proc. 9th Int. Symp. On the Effects of Munitions with Structures, 1999.

[89] Beissel, S.R., Holmquist, T.J., and Jhonson, G.R., “Influence of Third Invariant in the Ballistic Missile Impact of Silicon Carbide,” SwRI Report 18.12544/024, August 2010.

[90] Adley, M.D., Frank, A.O., Danielson, K.T., Akers, S.A, and O’Daniel, J.L., “The Advanced Fundamental Concrete (AFC) Model,” Technical Report ERDC/GSL TR-10-51, Vicksburg, MS: U.S. Army Engineer Research and Development Center, 25, 2010.

[91] Bresler, B., and Pister, K.S., “Strength of Concrete under Combine Stresses,” J. Am. Concrete I., Vol. 55, No. 9, pp. 321–345, 1958.

[92] Hsieh, S.S., Ting, E.C., and Chen, W.F., “A Plastic Fracture Model for Concrete,” Int. J. Solids Struct., Vol. 18, pp. 181–197, 1982.

[93] William, K.J., and Warnke, E.P., “Constitutive Models for the Traiaxial Behavior of Concrete”, Proc. Int. Assoc. Bridge and Structural Engineering, Bergamo, Italy, Vol. 19, pp. 1–30, 1975.

[94] Menterey, P.H., and William, K.J., “Triaxial Failure Criterion for Concrete and its Generalization,” ACI Struct. J., Vol. 92, pp. 311–318, May 1995.

[95] Imran, I., and Pantazopoulu, S.J., “Plasticity Model for Concrete Under Triaxial Compression,” ASCE J. Eng. Mech., Vol. 127, pp. 281–290, 2001.

[96] Grassl, P., Lundgren, K., and Gylltoft, K., “Concrete in Compression: A Plasticity Theory with a Novel Hardening Law,” Int. J. Solids Struct., Vol. 39, pp. 5205–5223, 2002.

[97] Kang, H.D., and William, K.J., “Localization Characteristics of Triaxial Concrete Model,” ASCE J. Eng. Mech., Vol. 125, pp. 941–950, 1999.

[98] Drucker, D.C., “On the Postulate of Stability of Materials in the Mechanics of Continua,” J. Mechanique, Vol. 3, pp. 235–249, 1964.

[99] Zukas, J.A., “Penetration and Perforation of Solids,” Impact Dynamics, Editors: J.A. Zukas, T. Nicholas, H.F. Swift, and D.R. Curran, John Wiley, pp. 155–214, 1982.

[100] Monaghan, J.J., and Gingold, R.A., “Shock Simulation by the Particle Method SPH,” J. Comput. Phys., Vol. 52, pp. 374–389, 1983.

[101] Monaghan, J.J., “An Introduction to SPH,” Commun. Comput. Phys., Vol. 48, pp. 89–96, 1988.

[102] Zukas, J.A., *Introduction to Hydrocodes*, Studies in Applied Mechanics 49, Elsevier, 2004.

[103] Holmquist, T.J., and Johnson, T.R., “A Computational Constitutive Model for Glass Subjected to Large Strains, High Strain Rates and High Pressures,” J. Appl. Mech., ASME, Vol. 78, pp. 0510031-9, 2011.

[104] Johnson, G.R., Holmquist, T.J., and Beissel, S.R., “Response of Aluminum Nitride (Including a Phase Change) to Large Strains, High Strain Rates and High Pressures,” J. Appl. Phys., Vol. 94, pp. 1639–1646, 2004.

[105] Langhaar, H.L., *Dimensional Analysis and Model Theory*, John Wiley, 1964.

[106] Buckingham, E., “On Physically Similar Systems; Illustrations of the Use of Dimensional Equations,” Phys. Rev., Vol. 4, pp. 345–376, 1914.

[107] Dancyngier, A.N., “Effect of reinforcement ratio on the resistance of reinforced concrete to hard projectile impact,” Nucl. Eng. and Des., Vol. 172, pp. 233–245, 1997.

[108] Abdel-Kader, M., and Fouda, A., “Effect of reinforcement on response of concrete panels to impact of hard projectile,” Int. J. Impact Eng., Vol. 63, pp. 1–17, 2014.

[109] Kabir, A., Hasan, M.M., and Miah, K., “Predicting 28-Days Compressive Strength from 7-Days Test Result,” Proc. Int. Conf. on Advances in Design and Construction, pp. 18–22, 2012.

[110] Nawy, E.G., *Fundamentals of High-Performance Concrete*, Second edition, John Wiley, 2001.

[111] CEAST 9300 Series. Drop Tower Impact Systems Catalog.

[112] Gordon Glass Co., 12 Mil Security Window Film 30" Wide x 10 ft. Roll.